UNIVERSITA' DEGLI STUDI DI PARMA

Dottorato di ricerca in Scienza e Tecnologia dei Materiali Innovativi

Ciclo XXVII (2012-2014)

Fabrication of high-efficiency $Cu(In,Ga)Se_2$ solar cells by Pulsed Electron Deposition technique

Coordinatore:
Chiar.mo Prof. Enrico Dalcanale

Tutor:
Chiar.mo Dott. Stefano Rampino

Dottorando: Matteo Bronzoni

2015

Abstract

In the past few years, a continuous rise of gas/oil prices promoted the exploitation of renewable energy especially from photovoltaic. This field is today monopolized by Silicon, either mono- or crystalline-, solar cells, although thin film technologies are gaining increasing interest for the possibility to reduce the material quantity and cost and to use light and flexible substrates. Among thin films, $CuInGaSe_2$ (CIGS) is the material with the highest conversion efficiency, close to 22%.

Despite the fact that the performances of CIGS-based solar cells are comparable to the silicon ones, their spread on the market has been limited by the high production cost; long and expensive multistage processes (thermal co-evaporation and sputtering/selenization) must be adopted to solve the problems related to the CIGS complex composition and incongruent melting.

An innovative deposition technique (PED, Pulsed Electron Deposition) has been developed at IMEM-CNR, aiming to simplify the growth of complex materials such as CIGS. PED is based on a non-thermodynamic equilibrium process, consisting in the ablation of a target with the same composition of the film to be grown, leading to a simple and “single stage” CIGS deposition.

The work is carried on in the frame of an industrial project “PED4PV” (Pulsed Electron Deposition for PhotoVoltaic), coordinated by IMEM-CNR and financed by the Italian Economic Development Ministry, with the purpose of optimizing the PED technique for depositing high efficiency (>15%) CIGS-based solar cells.

The first part of the thesis is focused to exploit the PED peculiarities (specifically, the optimal stoichiometric transfer from the target to the substrate) in order to obtain CIGS thin films of high crystalline quality and, remarkably, at a much lower temperature compared to the alternative growth techniques.

The optimization of the CIGS absorber layer and its doping, by Na addition, allowed to obtain solar cell efficiencies of 18.75% on active area.

The low temperature CIGS deposition process has been successfully tested also on crystalline substrates (GaAs and Ge), onto which monocrystalline CIGS films have been epitaxially deposited; the absence of structural defects such as grain boundaries could furtherly increase the efficiencies (up to a theoretical value of 28%).

The second part of the thesis is dedicated to a pre-industrial development of the PED process. In particular, the solutions to overcame the main problems typical to the high energy techniques have been studied:

i) reduction of the micrometric particulate on the film surfaces, caused by the interaction between the high-energy electronic beam and the target, by applying an appropriate electric field between target and substrate.

ii) increase of the deposition area, by designing and assemble a pre-industrial deposition chamber prototype equipped with different PED sources, suitable to fabricate photovoltaic cells with large area (16x16cm^2, same as the conventional Silicon-based cells) with high thickness uniformity.

iii) Stability of the electronic beam during long deposition time, limiting the PED sources heating. This has been achieved by designing realizing and testing a new type of heater based on the Joule effect (flowing a current through the solar cell metal back contact), enabling the growth of high quality CIGS on thermolabile and flexible materials such as polymers.

This thesis work contributed to the rapid development of CIGS-based thin film solar cells with efficiencies comparable to the highest values at international level, with a simple and potentially scalable industrial process.

Outline

Introduction

Global energy demand is growing very fast. The continuous world population increase and the consumption associated to the rising level of life require more and more energy. Fossil fuels, extensively used in the past, are no longer able, alone, to satisfy the global demand. Besides, other issues related to the increasing environmental pollution and greenhouse effect and the socio-economic and political problems in areas hosting the remaining oil reserves, are seriously impacting our everyday life. In this scenario it is vital to find alternative energy resources that must be renewable, clean and low-cost.

The sun is by far the energy source that could better meet global needs. Indeed, the energy produced by the sun is unlimited, cheap, available everywhere and nonpolluting. The solar energy reaching annually the earth's surface is 20,000 times greater than the current world consumption.

The photovoltaic technology, directly converting sunlight into electricity is the most promising method to harvest energy from the solar radiation. Nowadays, many research centers are strongly committed to increase the efficiency of these systems. The research in this area has been going on since the 70's, but only in the latest years, the photovoltaic installations reached the market maturity (and are continuously increasing). Recently, solar cells achieved high conversion efficiencies (≈25% in silicon-based devices), improved robustness (service lifetime >25 years) and reduced cost (<1€/W_p). The current price of turnkey photovoltaic systems guarantee payback period of few years.

The photovoltaic industry is essentially dominated by crystalline silicon. However, the segment of thin film solar panels, based on amorphous Si and II-VI semiconductors (CdTe and $Cu(In,Ga)Se_2$), is rapidly expanding. This technology allows greater savings in terms of costs and amount of raw materials. In a thin film solar cell the thickness of the absorber layer is about 100 times lower than in a standard silicon cell. Among thin films, $Cu(In,Ga)Se_2$ (CIGS) is the material with the highest absorption coefficient and the highest conversion efficiency, close to 22%, a value approaching the silicon-based solar cells.

In spite of that, the market penetration of cells based on CIGS is being limited by the high cost of the growth technologies. The commonly used techniques (thermal co-evaporation and sputtering/selenization) are based on long-lasting and complicated multistage processes for overcoming the challenges related to the CIGS complex composition and incongruent melting.

In order to simplify the CIGS-growth technology, in the last years the IMEM-CNR in Parma has developed a novel growth process based on the Pulsed Electron Deposition (PED) technique. From 2009 IMEM-CNR has been leading an industrial research project called "PED4PV" (Pulsed Electron Deposition for Photovoltaics), funded by the Italian Ministry of the Economic Development, in the frame of the “Industry 2015 - Energy Efficiency” Programme. The PED4PV project aims to: i) prove that high efficiency thin film solar cells (η>15%) can be fabricated by a simple and low-temperature process based on the PED technique, and ii) scale-up the PED technology for the fabrication of commercial modules.

PED is a Physical Vapour Deposition technique based on the generation of a pulsed electron beam (duration of ~100 ns) with high kinetic energy (>10 keV). This e-beam is accelerated and guided by a dielectric tube towards a CIGS target, leading to the "ablation" of the latter and to the formation of a cloud (or "plume") of plasma containing Cu, In, Ga, Se, in elemental form. The high e-beam energy allows a proper stoichiometric composition transfer from the quaternary target to the substrate, where the four elements condensate and the CIGS tetragonal phase re-forms.

This thesis, carried on in the frame of PED4PV project, aims to: i) the optimization of the deposition process, by exploiting the characteristics of the PED technique (i.e. simple single-stage deposition, stoichiometric transfer, internal energy of the plasma cloud) to develop a low-temperature and "easy" CIGS solar cells and ii) definition of a pre-industrial CIGS solar cell fabrication route based on PED technique.

The first part of this thesis is devoted to optimize the deposition process to obtaining high crystalline quality CIGS films at a growth temperature (<300°C) much lower compared to the traditional techniques (450-550°C).

Since the optimum absorber carrier concentration (usually dependent on the concentration of sodium (Na) diffused from the glassy substrate) must be achieved, the intentional deposition of a NaF precursor layer between the Mo back contact and CIGS is introduced to provide the necessary Na content, that can no longer diffuse from the substrate at such low temperature. The study of the effects of a post-growth annealing treatment on the cell performance uniformity over areas >6 cm^2 is also carried out. The design of the cell architecture, and in particular the transparent conductive oxide for minimizing resistive effects in the cells is also significantly improved. Finally single-crystal CIGS films are epitaxially grown on crystalline substrates (GaAs and Ge); by reducing the structural defects related to the CIGS polycrystalline structure, solar cells with theoretical efficiencies > 28% could be obtained.

The second part of the thesis is dedicated to the pre-industrial implementation of the PED technique. Specific solutions to mitigate some intrinsic challenges of the high energy techniques, are studied and tested:

1. Reduction of the micrometric particulate generated on the target surface and deposited on the growing film. Appropriate electric fields applied between target and substrate are used to repulse the particles from the substrate surface.
2. Larger deposition area. By studying the narrow-peaked angular distribution of the elements ablated from a single PED source over the deposition area, a mathematical simulation model for maximizing the coating uniformity using

an array of PED sources is built. In particular this model is used to optimize the thickness uniformity of CIGS layer over a 16x16cm^2-wide area (corresponding to a conventional silicon-based solar cell).

3. Long-term stability of the electron beam. With the goal of limiting the PED source heating, a new type of substrate heater is designed. The customized heater locally and rapidly heats the surface of Mo-coated glass substrates by Joule effect, without warming the PED source and the vacuum chamber. The limited heating of the substrate bulk allows the CIGS deposition by PED even on thermolabile and flexible materials such as plastics.

In collaboration with industrial partners, all the achieved results have been utilized to draw and built a pre-industrial prototype deposition chamber, equipped with a multi-PED system, for fabricating 16x16cm^2 CIGS-based solar cells. The prototype, recently installed at IMEM-CNR, is now fully operating.

The thesis is summarized as follows. The characteristics of a thin film solar cell, with particular attention to the physical properties of CIGS as absorber layer, are explained in Chapter 1, where the features and the limitations of the standard CIGS deposition techniques are discussed. The main features of the PED technique, in particular its peculiarities with respect to other growth methods, its advantages and the technological issues, are described in Chapter 2, together with a detailed description of the operating principles and the parameters leading the PED process. In Chapter 3 the experimental setup and the characterization techniques used to analyze the CIGS layers ("in situ" and “ex-situ” methods) are illustrated. The experimental results obtained during the thesis work are reported and discussed in Chapter 4. In the first part of this Chapter, the different methods to achieve cell efficiencies > 18% are treated, while in the second the technological improvements for drawing and assembling a pre-industrial prototype to realize solar cells (16x16 cm^2-wide) are described. In the last Chapter, the main results of the thesis are summarized with the perspectives for exploiting them both in fundamental understanding and for possible applications.

Chapter 1: CIGS Thin Film Solar Cell

The silicon-based modules are by far the most used in the photovoltaic (PV) market. This material allows to reach high efficiencies (25.6% on laboratory scale [1]) at low prices thanks to the long lasting research started over 40 years ago. In recent years, research moved to new materials and new technologies. The second generation of photovoltaic devices is based on thin film. The market analysts agree that this technology will play soon an important role, for allowing a significant material saving (the absorber layers are about 200 times thinner than the silicon slices used in the first generation) and, thus, enabling the fabrication of flexible solar cells.

Besides the lower material usage, thin film solar cells must possess high conversion efficiencies to be cost-effective; for example Cu(In,Ga)Se_2 (CIGS) reaches 21.7% efficiency on laboratory scale [2] and CdTe-based solar cells 21% (obtained by First Solar [3]).

A number of parameters in the complex structure of a photovoltaic cell have to be properly combined the get an efficient multilayer architecture. In particular, a material presenting its band gap optimally matched with the solar spectrum is required to maximize the cell performance. In the Figure 1.1 is shown the theoretical efficiency of a solar cell according to different absorber layer band gaps.

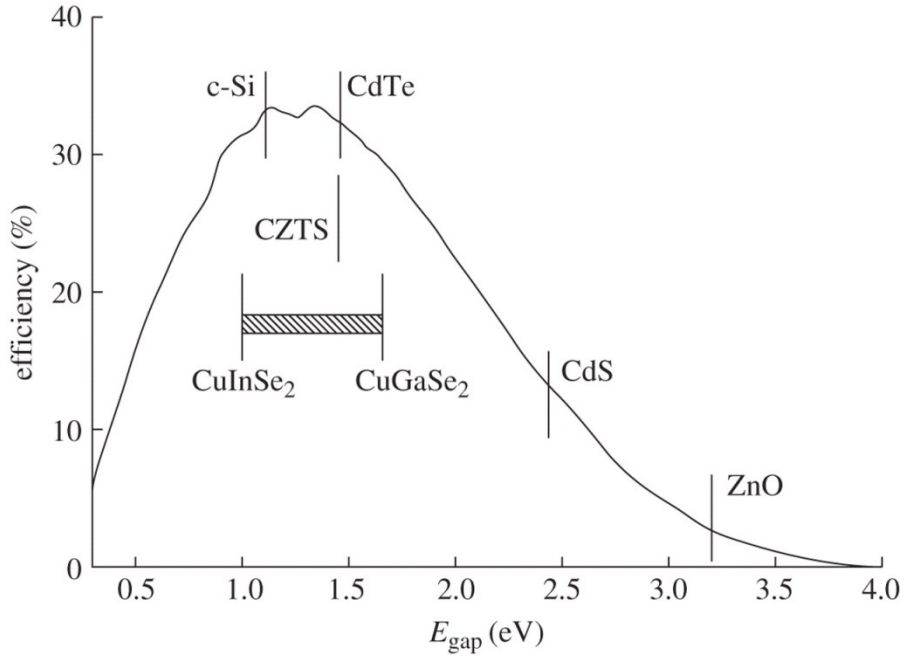

Figure 1.1: Maximum theoretical efficiency (Shockley–Queisser limit) for solar cells under AM1.5 illumination without concentration [4].

CIGS is a p-type semiconductor with a tunable band gap by varying the In/Ga ratio. CIS (without gallium) and CGS (without indium) have band gap values of 1.04 eV. and 1.70 eV, respectively. Therefore, CIGS presenting an intermediate composition (typical is $Cu(In_{0.7},Ga_{0.3})Se_2$) is an excellent material to be used as absorber layer in a photovoltaic cell.

A further CIGS advantage is the high absorption coefficient (Figure 1.2); therefore, only very few microns of material are sufficient to absorb the whole solar radiation [5].

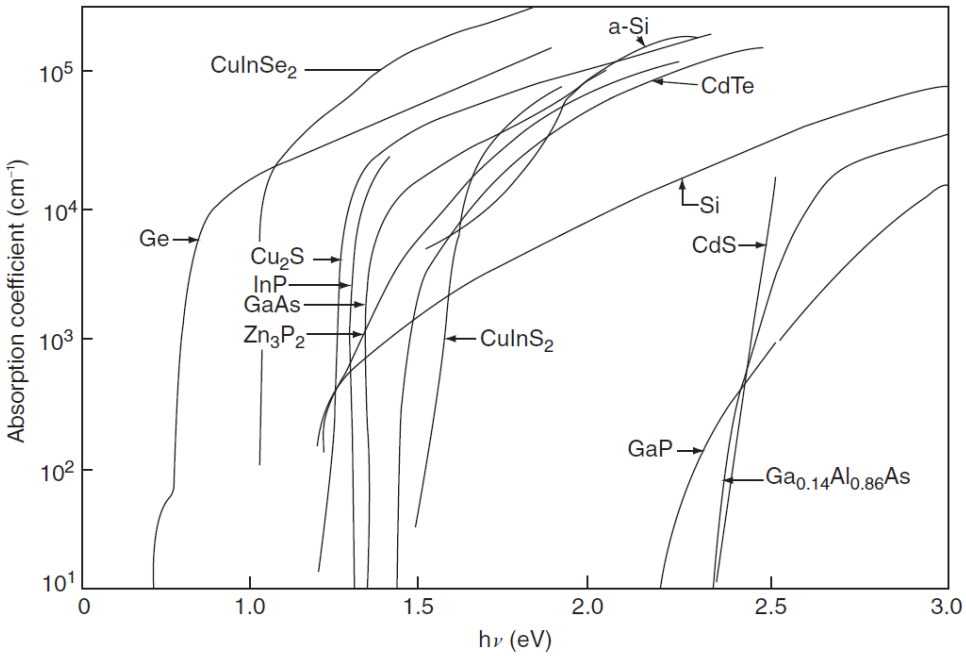

Figure 1.2: Absorption spectra of different semiconductors. [6]

The 2nd generation PV cells present a complex multilayer configuration. How the absorber layer (including its lattice parameters and energy level) fits within the structure of the cell is a key parameter to reach stable and efficient devices. The standard structure of a CIGS based solar cell is illustrated in Figure 1.3.

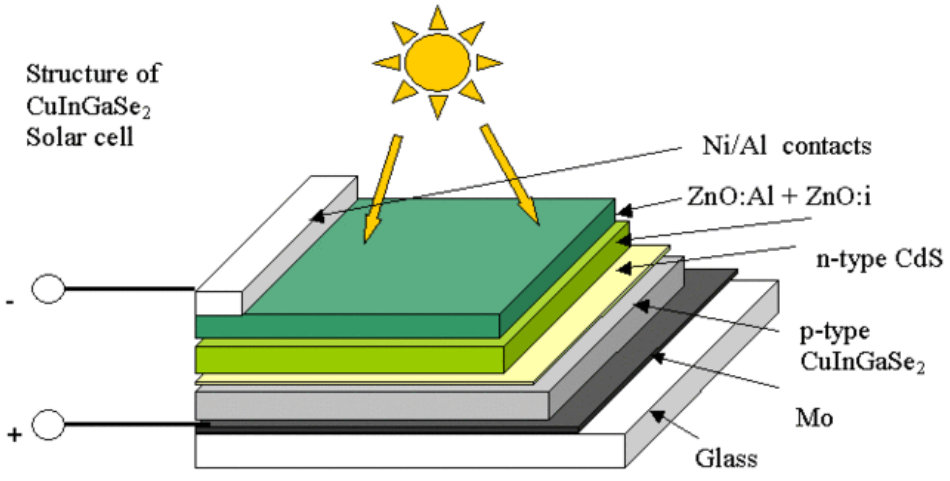

Figure 1.3: Representative scheme of CIGS-based solar cell [7].

In the realization of a conventional photovoltaic cell, a molybdenum (Mo) 500 nm thin layer is deposited by sputtering on a soda-lime glass (SLG), a widespread and commercially available substrate. Since the production of PV cells involves a high temperature process, the thermal expansion coefficient of the substrate must be taken into account; it should be as similar as possible to the absorber's one in order to prevent the layer detachment during the heating and the cooling process. SLG is a very good candidate as a substrate; it presents a suitable thermal expansion coefficient, it's easy to find, very cheap and contains sodium (Na). Na content is critical for the CIGS-based solar cell operation and Na migration from the glass substrate is the easiest way to "dope" the CIGS layer; this feature will be discussed in detail in Chapter 5. Other types of substrates can be used, in particular for flexible solar cells, such as Mo-coated plastics (polyimide) or metals (stainless steel, titanium).

About 2 μm of CIGS are then deposited onto the Mo layer. The most commonly used deposition technique is the co-evaporation [8] in which the four elements are simultaneously evaporated in 4 independent crucibles heated by Joule effect; the CIGS formation is the result of the condensation of the species on the substrate kept at high temperature (about 550 °C) [9]. The next layer is the n-side of the junction and it is based on a thin (≈ 50 nm) buffer layer of CdS grown by chemical bath deposition (CBD) and the cell is closed with a bi-layer by RF-sputtering: the first one is an intrinsically doped ZnO layer of about 70 nm, while the last is a 500nm-thick Aluminum(2%)-doped ZnO (AZO). These ZnO-based layers combine transparency and conductivity properties and belong to the group of the transparent and conductive oxide (TCO). These features allow the light to reach the underlying absorber layer and simultaneously the collection of the carriers generated by the incident photons. Finally the cell is completed with the electrical contacts on top, based on a metal aluminum grid.

As far as the $Cu(In,Ga)Se_2$ structural properties concern, the film usually shows a polycrystalline nature with typical grain size of ≈1μm and a pseudo-columnar growth direction perpendicular to the surface (Figure 1.4). This structure seems to be

particularly efficient to transport the charges towards the contacts, since the electrons photo-generated, driven by the internal electric field at the junction perpendicular to the growth plane, have not to cross the grain boundaries, which are macroscopic defects causing carriers recombination and annihilation. In this way, the electrical conduction occurs primarily along the grain, minimizing recombination and increasing the cell efficiency.

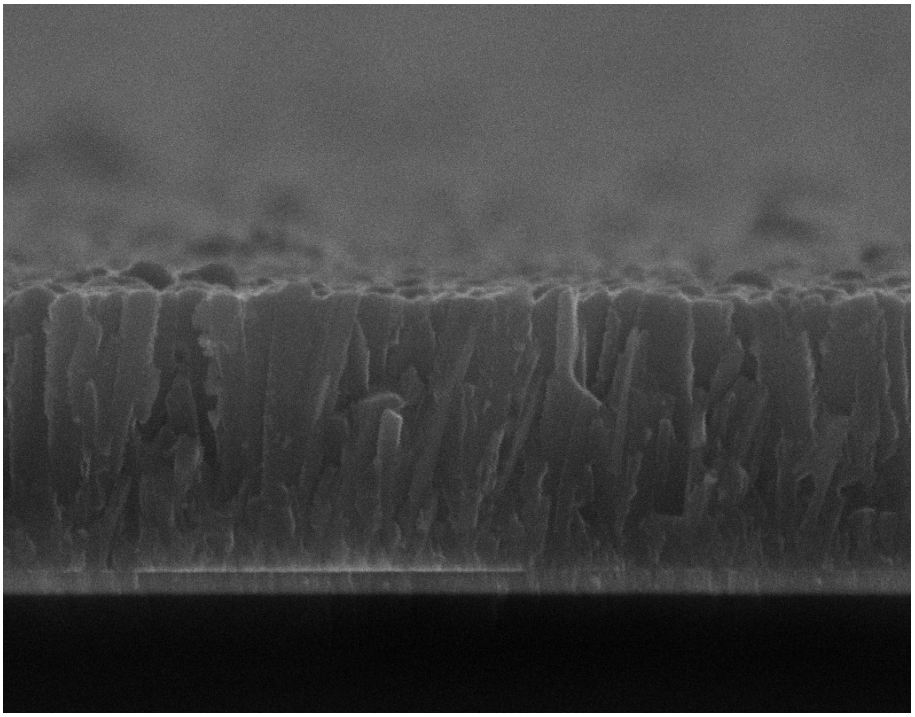

Figure 1.4: SEM cross section of CIGS absorber layer. Columnar grains perpendicular to the surface.

Another fundamental CIGS property to optimize is clearly is the chemical composition. The CIGS is a quaternary material composed by copper, indium, gallium and selenium; indium and gallium occupy interchangeable positions in the chalcopyrite structure. The CIGS can be considered a solid solution of other two compounds: $CuInSe_2$ (CIS) and $CuGaSe_2$ (CGS). The most important crystalline phase for a solar cells is the α phase shown in Figure 1.5 where the binary diagram

Cu_2Se-In_2Se_3 is depicted. The α phase occupies a very restricted area (stability region) in this phase diagram [10].

The CIGS growth is therefore extremely complex for all techniques working at the thermodynamic equilibrium (such as evaporation or sputtering) due to the incongruent melting of $Cu(In,Ga)Se_2$.

The α-polycrystalline CIGS has a p-type conductivity mainly due to the presence of copper vacancy, (V_{Cu}), which operate as electron acceptors.

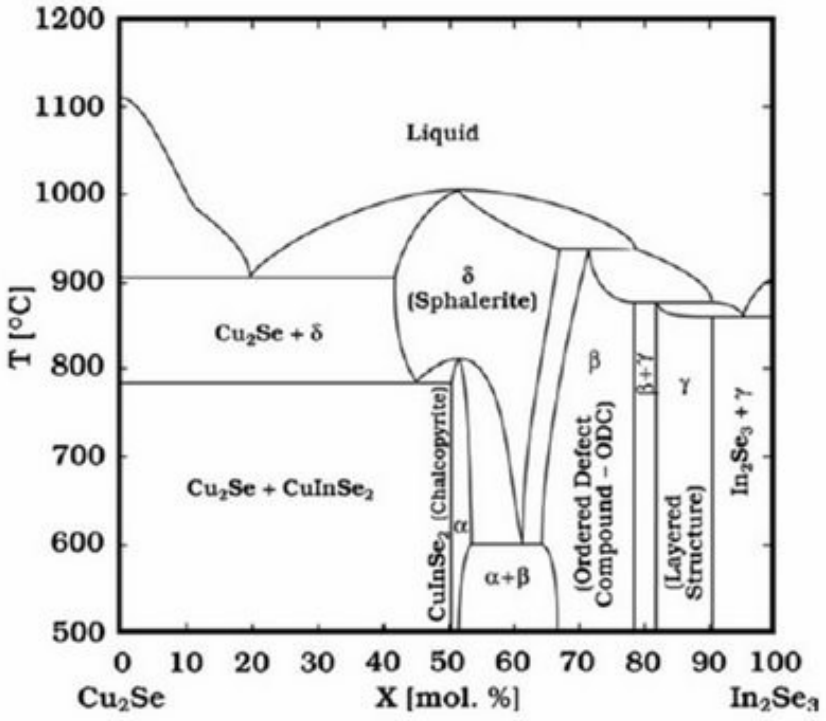

Figure 1.5: $CuInse_2$ phase diagram [11][12].

Among the various crystalline phases, it's very important to minimize the β phase, also called Ordered Defect Compound or Ordered Vacancy Compound (ODC/OVD) [13]: its composition is characterized by a Cu deficiency, which can be find in various phases: $Cu_2(In,Ga)_4Se_7$, $Cu(In,Ga)_5Se_8$, $Cu(In,Ga)_3Se_5$. All ODC phases are characterized by high resistivity and n-type conductivity.

Obviously, with β-CIGS layer the solar cell would not work, impeding the formation of the p-n junction. Therefore, in order to obtain a good quality absorber, one has to carefully control the Cu content; the compound requires the presence of a slight Cu deficiency (V_{Cu}) without producing the β phase.

In addition to the Cu vacancies, even the selenium (Se) concentration is a crucial parameter for the CIGS composition. Indeed, films poor in Se show vacancies (V_{Se}) that decrease the carrier number and consequently the cell efficiency, since V_{Se} operate as electron donors and compensate the holes in the film. Moreover, V_{Se} affect the CIGS chemical stability, making the CIGS surface highly reactive to oxygen, substituting Se in the structure, that is known to be detrimental for the quality of the absorber [14].

On the contrary, the excess of Se excess, tents to accumulate in the grain boundaries, passivating them and improving the cell operation. Another advantage of the interstitial Se is the reduction of the oxygen reactivity. For these reasons, after the CIGS deposition, a selenization treatment is required. This process involves the evaporation/diffusion of selenium on the film surface during the annealing process.

1.1 CIGS sodium doping

One of the main aspects to be considered during CIGS growth is sodium (Na) doping. The main role of Na is to increase the open circuit voltage (V_{oc}) and to optimize the fill factor (FF) (the ratio of maximum power measured and the product of the open-circuit voltage and short-circuit current, as shown in Chapter 3) of the cells, while the short circuit current (J_{sc}) remains virtually unchanged. The Na effects on CIGS are essentially related to the increase of the free carrier density, obtained by the Na inclusion inside the grains and by the passivation of defects at the grain boundaries. Solar cells based on Na-doped CIGS exhibit more stable performance for a wider range of Cu concentration [15 16 17] .

To explain why Na-doped CIGS show higher efficiencies, many experimental results reported in the literature have to be reviewed. The changes in CIGS layer due to Na addition can be classified into four points [15] (see Figure 1.6):

1. The first and most important feature is the effect on the increase of the carrier concentration. Although the reason for this increase is still debated, this has been reported by various groups and now is accepted by the scientific community as directly due to Na incorporation.

2. A decrease of the ratio Ga/(In+Ga) near the central region of the absorber (far from the interfaces) causes unwanted band gap gradients, affecting the carrier production and the carrier collection.

3. The variation of the CIGS crystal structure. A preferred orientation of grains along the (112) direction has often been reported in Na-doped CIGS.

The CIGS morphology is also affected by the Na presence: doped polycrystalline films exhibit smaller grain size with respect to the undoped CIGS.

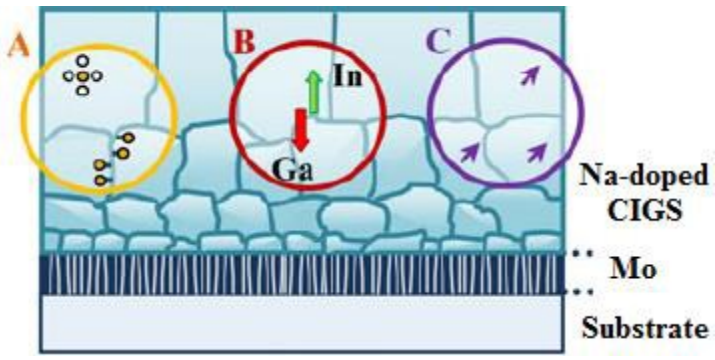

Figure 1.6: Sodium effect in CIGS: (A) Carrier density increase due to doping and grains boundaries passivation; (B) gallium segregation; (C) structural preferred orientation changes [18].

The technological strategies developed to incorporate sodium inside the CIGS are listed below (see Figure 1.7):

1. The standard method is based on the sodium diffusion from a Na-rich Soda-Lime Glass (SLG) substrate. Na migrates through the back contact to the polycrystalline CIGS film, where it segregates at the grain boundaries (see Figure 1.7.a). The substrate temperature is a key factor to maximize Na diffusion during the nucleation and the grain growth of CIGS while the post-growth annealing favors the propagation of Na towards the CIGS surface.

2. By the precursor route, depositing a Na-based layer. This precursor, generally sodium fluoride (NaF) is deposited before the CIGS and thus affects the growth dynamics of the absorber (see Figure 1.7.b). An annealing process enables the Na diffusion inside the CIGS.

3. The simultaneous deposition of CIGS and Na-based compounds allows the direct incorporation of Na into the absorber layer without needing any annealing process (see Figure 1.7.c). This also include the incorporation of Na into the CIGS target; this solution has been ruled out, since Na, being highly hygroscopic, causes the fragmentation of the bulky target once exposed to the air.

4. The Post Deposition Treatment (PDT) is based on the NaF deposition after the CIGS growth (see Figure 1.7.d). In this case, during the nucleation and the growth of CIGS, Na is not present, but its diffusion into CIGS is triggered by a post deposition annealing performed after the deposition of a NaF layer. Both temperature and duration of the PDT process are crucial parameters [15].

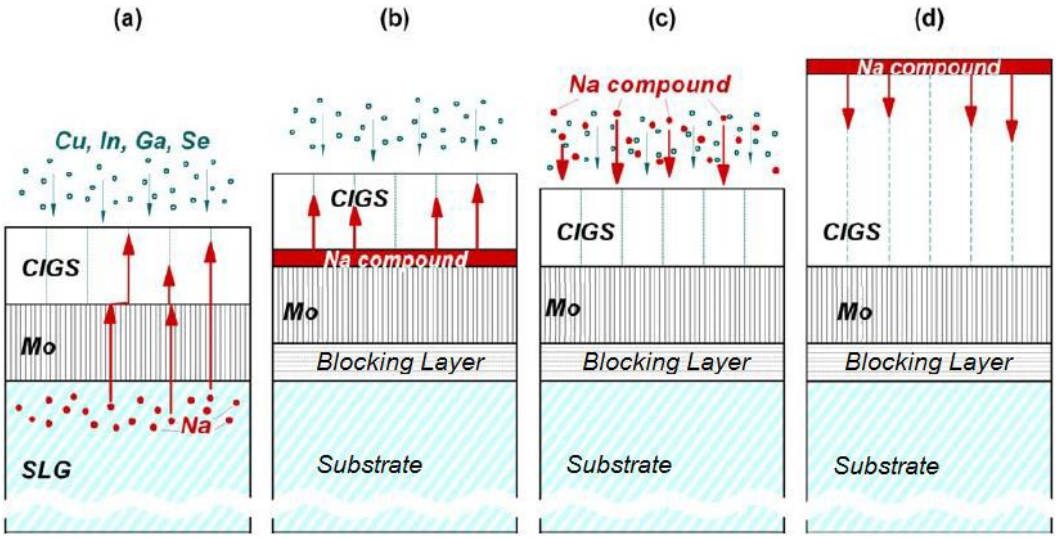

Figure 1.7: Different Na incorporation method: standard SLG method (a), precursor method (b), simultaneous deposition (c) PDT (d) [15].

1.2 CIGS film industrial deposition technique

In recent years, many companies and research centers focused to develop of CIGS-based thin film solar cells on standard (glass) substrates and unconventional (flexible) substrates. There are different approaches to deposit CIGS thin films; some groups use vacuum deposition methods, others work with liquid phase growth techniques. The latter allows to obtain devices with lower efficiencies, but it offers considerable advantages from the point of view of the experimental apparatus and the investment costs.

The CIGS thin film growth techniques can be divided in two different groups:

1. Physical techniques (PVD, Physical Vapour Deposition): thermal co-evaporation, sputtering, high-energy techniques (PLD and PED);
2. Chemical techniques: Electrodeposition, Spray Pyrolisis, Ink Jet, and others.

The most used methods to produce CIGS based solar cell at industrial level belong to the PVD techniques, namely co-evaporation, sputtering and pulsed electron deposition.

1.2.1 Thermal co-evaporation

The best CIGS in term of efficiency has been obtained by the thermal co-evaporation technique [2], nowadays, most of the CIGS modules on the market are produced using this technique. It is based on the simultaneous evaporation of the material elements from different sources. It can be performed in a single process or in a sequential way (see Figure 1.8).

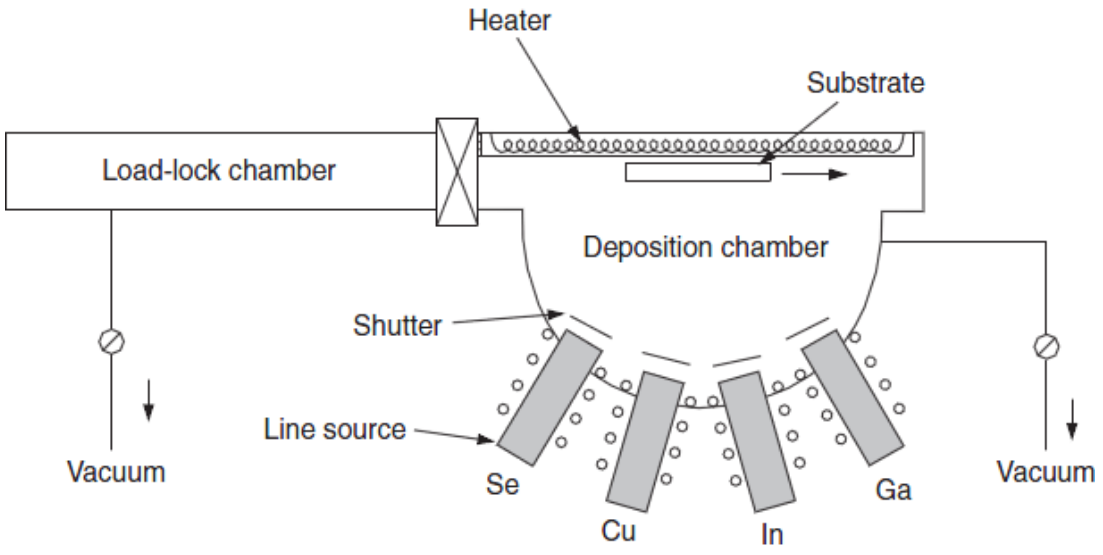

Figure 1.8: Schematic representation of thermal co-evaporation system used for CIGS thin film deposition [19].

In this growth method, since the energy of the evaporated specie is very low, the substrate temperature is high (500-600 °C) value because the atoms arriving on the substrate surface need some additional energy to move and reach the right sites. There are different methods to grow the CIGS layer, classified according to the Cu evaporation profile (see Figure 1.9).

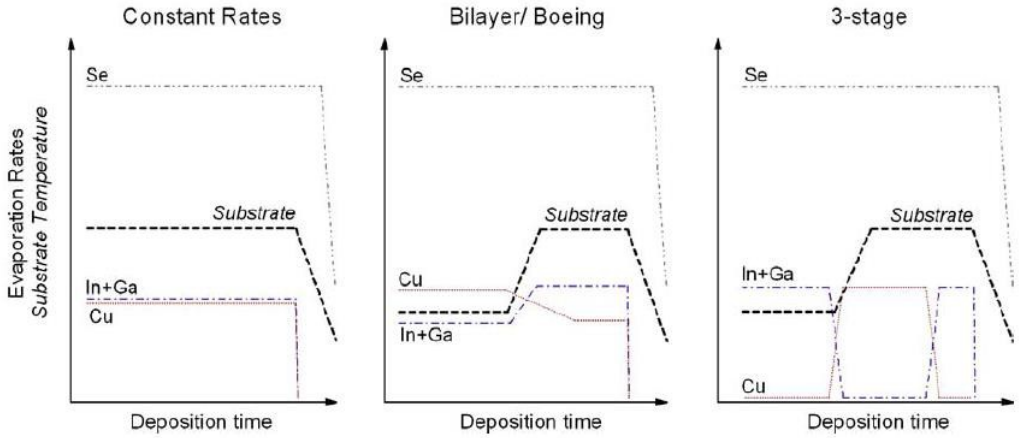

Figure 1.9: Different method to grow CIGS by thermal co-evaporation [15].

The diffusion of Cu into the film during the growth is fast enough to allow a homogeneous distribution in the final absorber layer while the interdiffusion of In and Ga is slower than Cu. By varying the evaporation flow during the process, the [Ga]/[In] ratio can be tuned, leading to a different concentration of the two elements into the film (Ga grading). In all co-evaporation processes, excess of Se is supplied during the film growth. Due to the low evaporation temperature, the Se exceeding the stoichiometry is not embedded in the film but re-evaporate from the hot surface. After the CIGS layer formation, in order to avoid Se losses from the absorber surface in the cooling step, a selenization process is needed. This is a high-temperature treatment involving a H_2Se atmosphere. H_2Se is a volatile very toxic compound which requires the use of expensive security systems.

The most efficient solar cells have been obtained by applying three different stages to produce CIGS absorber layer (the so called 3-stage method). As reported in Figure 1.10, the first step is the deposition of $(In,Ga)_2Se_3$ precursor at low substrate temperature (250-400 °C), In the second stage, Cu and Se are deposited at high temperature (typically 550 °C) with a slightly Cu-rich composition. Finally, in the third and last step, In,Ga and Se are evaporated keeping the same high substrate temperature, until the desired stoichiometry (Cu poor CIGS) is reached.

This type of CIGS growth leads to smoother and more regular surfaces, reducing the interface area with the buffer layer and even the morphological defects inside the junction [15].

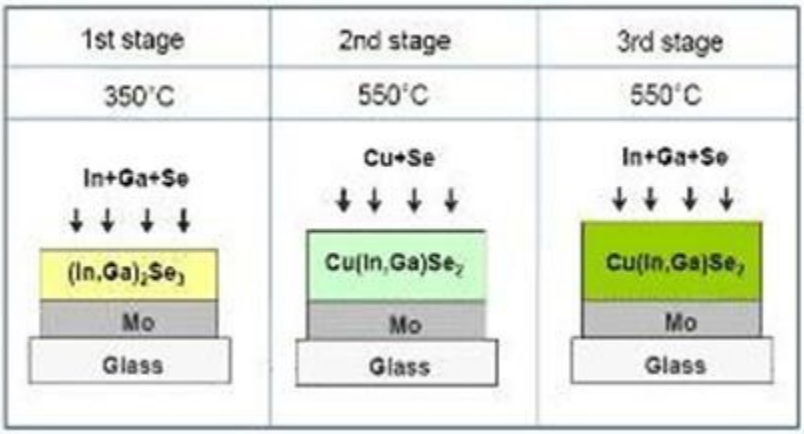

Figure 1.10: Three stage process schematic representation.

1.2.2 Sputtering

Sputtering is a physical deposition technique, widely used at industrial level for the large-scale production of a number of materials over large areas. Its operation is based on the ion-bombardment of a target obtained from the plasma formation of an inert or reactive gas inside the vacuum chamber and the subsequent acceleration towards the target. The gas atoms are ionized by a high voltage applied to the cathode holding the target; the plasma ions are accelerated by the electric field towards the target, and the collisions cause the surface atoms ejection. The acceleration voltage, the gas pressure and the anode-cathode distance are the basic parameters of the process. In order to ensure both a good deposition rate and a low gas pressure in the chamber, a magnetic field in a special geometry is often used ("magnetron sputtering"). It keeps the electrons confined on the target surface creating multiple ionizations and maintaining the plasma on even at lower pressure. Depending on the material to be deposited, different power supplies are available; for example an AC voltage at high frequencies (> 1 MHz) where only the electrons

can follow the rapid field inversion ("RF sputtering"), can be used for dielectric targets. In this way, it is possible to neutralize the charge stored on the target surface in order to avoid the voltage drop and consequently the ion kinetic energy that means a less effective bombardment.

Similarly to the co-evaporation process, also for sputtered CIGS different precursors are deposited in consecutive steps (InSe, GaSe and Cu or InSe, GaSe, Cu and GaSe) (Figure 1.11), treated in high temperature (about 500 °C) and selenized in a final “ex-situ” stage where the wanted phase is formed.

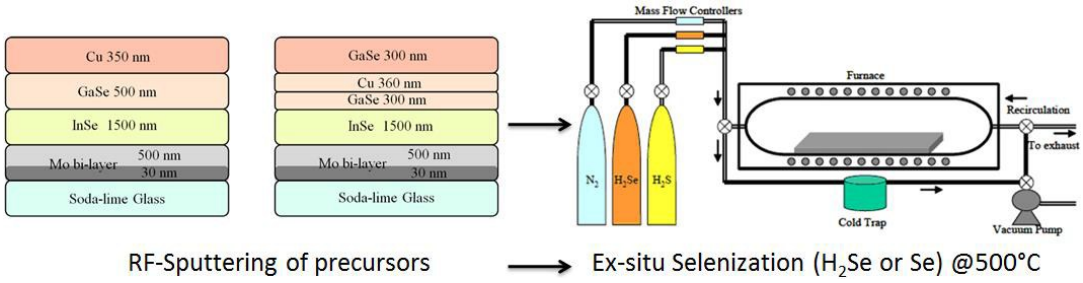

Figure 1.11: Schematic representation of CIGS growth by sputtering system. [20]

This technique is suitable for photovoltaic thin film technology because it is used to deposit other layers constituting the solar cell, such as the molybdenum back contact, the buffer layer (CdS, ZnS or other compound) and the TCO’s.

References

[1] K. Masuko, M. Shigematsu, T. Hashiguchi, D. Fujishima, M. Kai, N. Yoshimura, T. Yamaguchi, Y. Ichihashi, T. Mishima, N. Matsubara, T. Yamanishi, T. Takahama, M. Taguchi, E. Maruyama, S. Okamoto, IEEE J. Photovolt 4 (2014) 1433 - 1435

[2] P. Jackson, D. Hariskos, R. Wuerz, O. Kiowski, A. Bauer, T. M. Friedlmeier, and M. Powalla, Phys. Status Solidi RRL, 9 (2015) 28–31. doi: 10.1002/pssr.201409520

[3] First solar builds the highest efficiency thin film PV cell on record, First Solar Release, August 5, 2014, http://investor.firstsolar.com/releasedetail.cfm?ReleaseID=864426

[4] L. M. Peter, Phil. Trans. R. Soc. A 369 (2011) 1840-1856

[5] A. L. Fahrenbruch and R. H. Bube, Fundamentals of solar cells. New York: Academic Press, 1983

[6] S. R. Kodigala CIGS BASED THIN FILM SOLAR CELLS. s.l. : Elsevier, 2010. pp. 16

[7] http://www.speedace.info/honda.htm

[8] S. R. Kodigala CIGS BASED THIN FILM SOLAR CELLS. s.l. : Elsevier, 2010. pp. 29-36

[9] T. Negami, T. Satoh, Y. Hashimoto, S. Nishiwaki, S.-I. Shimakawa, S. Hayashi, Sol. Energy Mater. Sol. Cells 67 (2001) 1

[10] M.L. Fearheiley, Solar Cells 16 (1986) 91

[11] B.J. Stanbery, Critical Reviews in Solid State and Materials Sciences, 27 (2) (2002) p. 73-117.

[12] T.Anderson, Processing of $CuInSe_2$-Based Solar Cells: Characterization of Deposition Processes in Terms of Chemical Reaction Analyses. 1999, University of Florida: Gainesville, FL. p. 1-56

[13] S. R. Kodigala CIGS BASED THIN FILM SOLAR CELLS. s.l. : Elsevier, 2010. pp. 100-110

[14] R. Noufi, R. C. Powell, R. J. Matson. Solar Cells 21 (1987) pp. 55-63

[15] D. Rudmann, Effects of sodium on growth and properties of Cu(In,Ga)Se2 thin films and solar cells. s.l. : Dissertation for the degree of Doctor of Sciences, Swiss federal institute of technology - Zurich, 2004.

[16] M. Bronzoni, Studio e ottimizzazione del processo di deposizione di CIGS mediante la tecnica pulsed electron deposition (PED). s.l. : Material physics thesis, Università degli Studi di Parma, 2011.

[17] J. Hedstrom, H. Ohlsen, M. Bodegard, A. Kylner, Stolt, Lars, D. Hariskos, M. Ruckh, H. Schock, Proc. 23rd IEEE Photovoltaic Specialists Conf., (1993) pp.364 -371

[18] E.S. Mungan, Xufeng Wang, M.A. Alam, IEEE J. Photovolt. 3 (2013) 451 - 456

[19] S. R. Kodigala CIGS BASED THIN FILM SOLAR CELLS. s.l. : Elsevier, 2010. pp. 30

[20] F. Annoni, Studio degli effetti del Na nelle celle a film sottile di Cu(In,Ga)Se_2 realizzate mediante Pulsed Electron Deposition (PED). s.l. : Material Science Thesis, Università degli Studi di Parma, 2012.

Chapter 2: Pulsed Electron Deposition (PED)

The pulsed electron beams (Pulsed Electron Deposition, PED) is a low cost technique with a high energy conversion efficiency able to grow complex materials (structure, composition, etc.) in thin film form. Therefore, it could be consider a candidate in the search for alternative and efficient methods to grow CIGS-based thin film solar cells solar.

In this Chapter, the operating principle of this technique will be described and the steps to generate the electron beam and its interaction with the target, will be explained. Following, advantages and challenges that make PED a suitable method to deposit CIGS film will be addressed.

PED is a high-energy PVD technique, where a pulsed high-energy electron beam, with high current density, ablates the target surface. The huge power, transferred in a relatively short period, allows to avoid the material fusion in favor of an ideal ablation: all the elements composing the target material rapidly evaporate far from the thermodynamic equilibrium. This allows to efficiently transfer the stoichiometry from the target to the growing film, necessary to grow complex or incongruent melting materials, such as composite metal oxides, complex alloys and polymers [1 2 3 4].

The PED is a recent technique, similar to the Pulsed Laser Deposition (PLD), much more known and widespread based on a laser pulse for target ablation. The two high-energy techniques share common features: ablation mechanisms, degradation

phenomena of the target surface, plasma properties, good stoichiometry transfer and film growth. The main difference is the beam type; the pulsed excimer laser sources of PLD cost about 20 times the electron beam sources used for PED. This makes PED the high-energy technique less expensive available on the market. Further advantages of PED are the larger energy transfer efficiency and the capability to ablate all the materials transparent to the laser photons, such as glass, polymers, TCO and anti-reflection coatings for photovoltaic cells.

The technical characteristics of the PED operation, such as pulse frequency, pulse width, electron beam acceleration voltage and current density, must be carefully calibrated to control the interaction between the electrons and the target matter. Therefore, to prevent target melting below the surface, it is necessary to limit the electrons penetration length, thus accelerating voltages are not settable over 20kV. In any case, the current density required is very high (>10^5 A/cm^2), corresponding to an electron beam power in the order of 10^8 W/cm^2. The pulse frequency (tunable between 1 and 20 Hz) and the short pulse width (about 100 ns) prevent the melting or the evaporation of the material at the thermodynamic equilibrium avoiding an eventual stoichiometry loss due to the incongruent melting point of the target.

Although PED is a rather new technique, it's becoming more and more popular and has been successfully used to growth superconducting films (YBCO), absorbers layer in solar cells (CIGS), semiconductors (ZnO) and various oxides (Al_2O_3, soda-lime glass) with high structural and compositional quality [1 2 3 4].

2.1 Electron beam generation and acceleration

The formation and acceleration of electron beams with high current density are nearly impossible in high vacuum, primarily because of the mutual repulsion between the electronic charges. Is therefore needed at least a low pressure gas atmosphere (background) to neutralize the electron space charge and confine the beam.

2.1.1 Electronic source

The electron source to produce high current beams is the “heart” of the PED technique; it’s based on a hollow cathode made with a particular geometry which basically consists in a metal tube, positioned in front of a plane anode.

The electrons are extracted from the internal walls of the cathode due to photoelectric effect and to the ion impacts. In a first step, the electrons move slowly because of the weak electric field inside the hollow cathode increasing the probability of ion formation. The special geometry forces the electrons to oscillate around the axis, efficiently ionizing the gas present in the cavity. In a second stage, they are accelerated towards the anode. This type of source operates in continuous current.

The pulsed mode is essential to achieve extremely high currents, requiring a change the hollow cathode. A tight hole is used to collimate the beam when the electrons are extracted. This particular setup is called transient hollow cathode (THC). In this way it is possible to obtain pulsed discharges lasting about 100 nanoseconds with some kA/cm^2 of current density; the repetition rate is controlled by a trigger. In series with the cathode an electrolytic capacitor stores and provides the charge; it can be discharged, in a very short time, defining the pulse duration. To ignite the controlled breakdown, a proper amount of gas is needed; too low pressure does not allow the avalanche ionizations and the beam propagation, while too high pressure induce the self-discharge phenomena. In this case the electron beam loses its pulsed nature, becoming a continuous discharge with much lower current density. The geometrical factors also play an important role; the Paschen curve (Figure 2.1) illustrates the discharge voltage as function of gas pressure inside the electron gun and the distance between the electrodes d:

$$V_B \times P \times d = cost$$

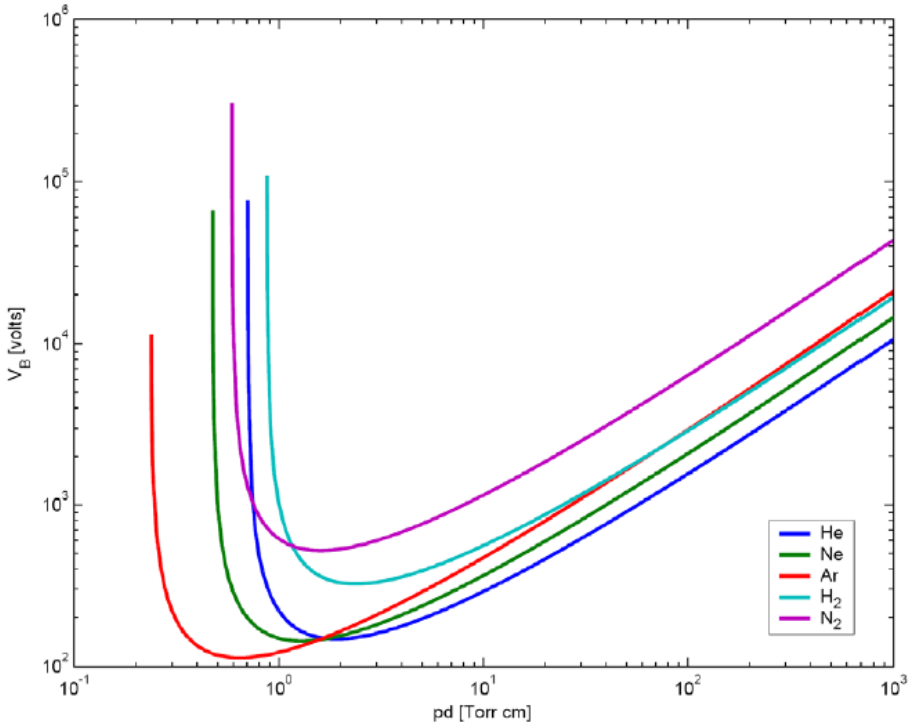

Figure 2.1: Paschen curve of different kind of gas. Breakdown voltage as function of pressure x distance.

The best region to trigger the discharge is the left side of the Paschen curve, where it is possible to work at low pressures without any risk of self-triggering. It minimizes the scattering effects of electrons and also between the particles ablated from the target, increasing the deposition rate and promoting a high quality growth of the films.

2.1.2 Electron beam acceleration and propagation

Once the electrons are generated, the beam propagation requires a collimation and acceleration towards the anode direction. This can happen in Channel-Spark mode, introducing a dielectric tube of radius r through which the beam can propagate. From the Paschen law, in the pressure range of 10^{-3}-10^{-4} mbar and in presence of high voltage (tens of kV) necessary to induce the ablation, the distance d between the

anode and cathode would be in the order of some mm. In this new configuration, the law driving the discharge is:

$$V_B \times P \times 2r = cost$$

Therefore, the distance between anode and cathode becomes arbitrary (Figure 2.2).

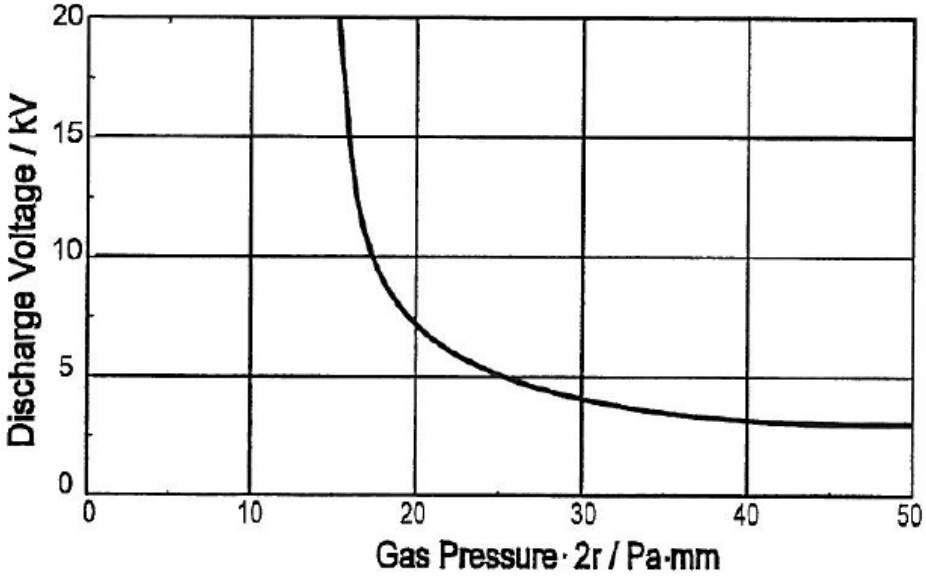

Figure 2.2: Breakdown voltage as function of gas pressure in dielectric tube with internal diameter d =5 mm [3].

Furthermore, in this configuration, the beam generated and propagated inside the insulating tube is very stable making the energy conversion efficiency in the Channel-Spark PED technique as high as 30%.

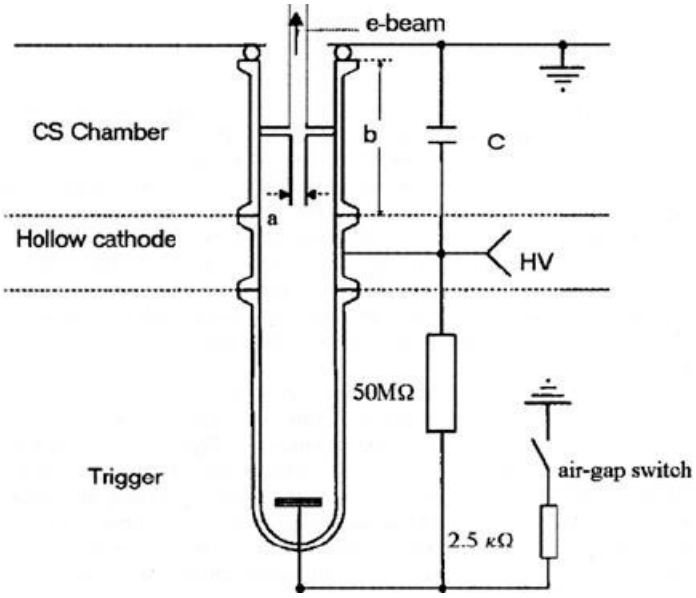

Figure 2.3: Schematic representation of PED source in channel-spark configuration [3].

2.1.3 Constrain discharge dynamics

The Channel-Spark system consists of a THC connected to a dielectric tube operating at low pressure conditions. Beam generation in the Channel-Spark mode can be summarized in the following steps:

1. The trigger generates a low current discharge;
2. THC inject the electrons;
3. The electrons generated create the beam;
4. The electron beam is accelerated inside the dielectric tube;
5. The electrons exit from the tube and strike the target material, ablating it.

The beam product is a plasma channel formed by the positive ions where high-energy electrons flow in. Different devices, such as Faraday cups [5] or Rogowski Coils [6] have been used to study the beam current and energy evolution during the pulse, allowing to understand the poly-energetic nature of the beam (Figure 2.4).

The beam power can be divided in three different contributions as a function of the time:

1. The beam head is constituted by a few electrons (low current) but very fast and with high energy;
2. Following, a relatively low current due to electrons average energy;
3. Finally, the pulse ends with an high current, due to low-energy electrons (the slowest)

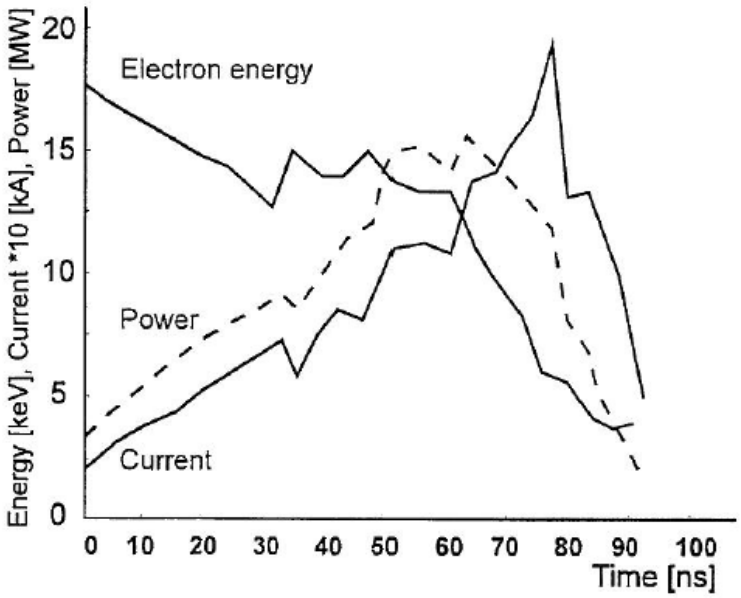

Figure 2.4: Energy, current and power of electron beam as function of time in a channel spark system [3].

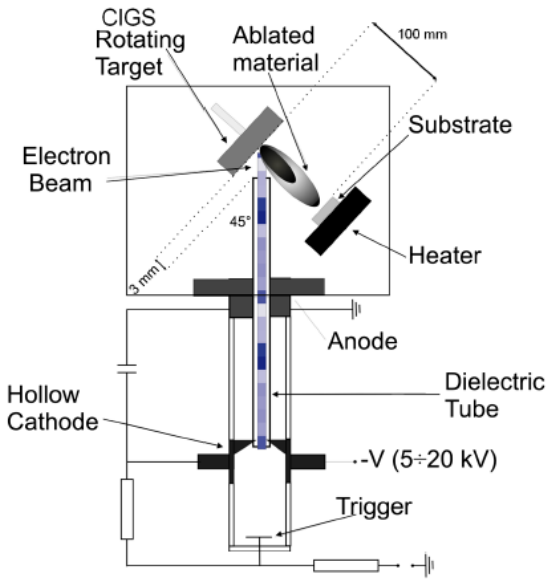

Input voltage	115-230 VAC, 50/60 Hz, single phase
Gas pressure, oxygen	5-20 mTorr
Energy of electrons	8-20 kV
Single pulse energy	0.1 – 0.8 J
Pulse energy variation, maximum	±10%
Energy conversion efficiency	25-30%
Pulse width	~100 ns
Pulse repetition rate, maximum	15 Hz
Beam cross section, minimum	6 x 10^{-2} cm^2
Beam cross section variation, maximum	±20%
Pulse power density, maximum	1.3 x 10^8 W/cm^2
Z alignment range	50 mm
XY alignment range	±20 mm
Cathode module lifetime	10^7 pulses
Temperature of PEBS body, maximum	85°C (180°F)

Figure 2.5: Schematic representation of channel-spark PED system [7][3].

2.2 Interaction between the electron beam and the target

When the electron beam hits the target, the electrons transfer their kinetic energy through inelastic collisions to the target atoms, causing a rapid temperature increase of the material surface. If the beam power is sufficient to exceed the material ablation threshold (the minimum power density required to ablate, generally in the range 1-5x10^7 W/cm^2) [8] [9]. The evaporation process is out of thermodynamic equilibrium. This leads to the plasma plume generation, which propagates in the perpendicular direction to the target surface at supersonic speed towards the substrate placed in front. The interaction between the electron beam and the target atoms depends only by the cross section of electronic scattering; consequently, the pulsed electron beams technique is independent on the target material in the ablation conditions [8].

2.2.1 Electrons penetration length

The electrons penetration depth inside the target is a crucial parameter. In fact, in the PED technique is essential that the interaction volume between the electrons and the target material is greater than the heat diffusion volume during the beam-target interaction time. This is necessary to avoid the target heating; if the temperature increases without exceeding the ablation threshold, this mainly generates two problems:

1. The energy diffusing by thermal conduction in the material does not contribute to ablation and it is wasted. In addition there is a reduction of the amount of ablated material in each pulse and then a decrease of the deposition rate. The ablation under the threshold increases the time deposition.

2. Processes at thermodynamic equilibrium such as melting and evaporation. In case of materials with an incongruent melting point (i.e. a different composition of the solid and the liquid phase), a stoichiometry variation between the target and the deposited film occurs and the film grows enriches in elements with the lower melting temperature.

The electron penetration length (δ) in the material is a function of their energy (E) and the material density (ρ) according to the equation:

$$\delta = 5.37 \times E \times \left(1 - \frac{0.9815}{1 + 0.0031 \times E}\right) \times \frac{1}{\rho}$$

where ρ is expressed in g/cm^3 and E in keV (1-20 KeV). The electron beam penetration depth, with energy of between 10 keV and 20 keV, is about 1 micron below the target surface. Furthermore, high density materials completely absorb the beam in a thicker layer than the lighter ones. The heat diffusion length for a pulse width τ is equal to:

$$\delta_T = 2\ (\alpha \times \tau)^{1/2}$$

In the PED technique, the condition of congruent ablation is:

$$\delta > \delta_T$$

Density and thermal conductivity are intrinsic features of the target material and they require an optimum voltage to obtained the congruent ablation. If this condition is not verified, the heat would diffuse in the target causing the fusion of the material, leading to incongruent evaporation phenomena and "splashing" or "surface super-boiling" (degradation phenomena of the target surface morphology which also cause the particulates deposition on the film). There are two different ways to keep the system in congruent ablation conditions:

1. Maximizing the electrons penetration depth in the target, but this is not the best strategy, because the increase of the interaction volume reduces the power density absorbed by the material. The minor power density cannot ablate the target creating problems of surface super-boiling;
2. Minimizing the diffusion range of the heat by controlling the pulse width: shorter pulses can reduce the thermal diffusion length.

The latest electron source available on the market are moving towards this latter option to reduce the pulse width and to increase the ablation process efficiency.

2.2.2 Target power absorption

The ablation process is closely related to the power absorbed by the material. As already mentioned, the non-thermodynamic equilibrium ablation process is possible only if the power absorbed by the material exceeds a specific threshold. The following relation describes the rate of temperature:

$$\frac{dT}{dt} \propto \frac{I \times V}{S \times C \times \rho \times (\delta_T + \delta)}$$

where I is the beam current, V the electrons acceleration voltage, S the interaction area with the target, C is the target thermal capacity, ρ the target material density,

δt the thermal diffusion length and δ the electronic diffusion length of the target. The ratio dT/dt represents the heat variation in the unit time, directly proportional with the beam power (IxV) and in inverse proportion to the interaction area, to the heat and electric diffusion processes. Therefore, the absorbed power density is an important factor and should be carefully studied. As already noticed, the electron beam produced by the PED source is not monochromatic, but poly-energetic: it consists of several groups of electrons that impact on target surface at different times and different currents and energies characterize them. The power transferred by the PED electron beam can be divided into the sum of different mono-energetic contributions (see Figure 2.6).

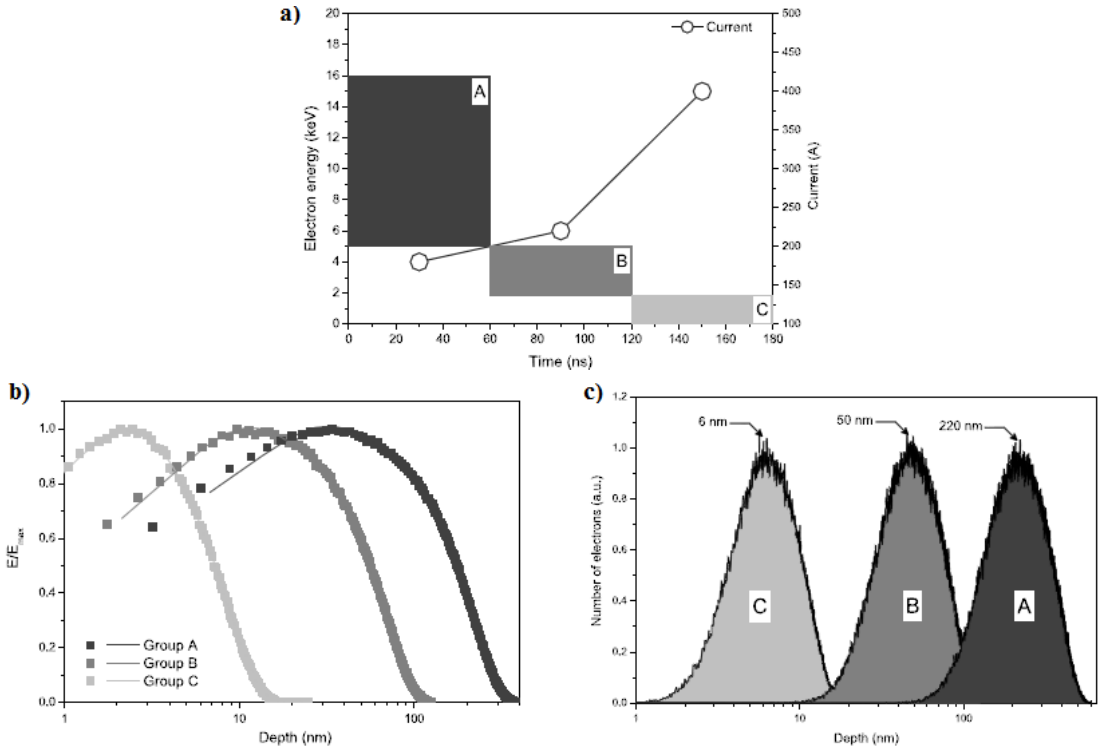

Figure 2.6: (a) Different electron beam component as function of energy and current. (b) Normalized distribution profile of energy transfer of different electron beam component. (c) Number of electron as function of penetration length [8].

The sum of the different distribution ends up to the confinement of the maximum power absorption near the surface. This PED feature permits to minimize the target

degradation effects during growth process, as "surface super-boiling" and incongruent evaporation.

2.2.3 Macroscopic ablation

When a particle beam hits a solid target, several processes occur; they can be divided in four categories:

1. Collisional ablation: It is due to impact of high-energy massive particles and the material target nuclei, therefore the atoms are expelled for simple moment transfer (Ex: Sputtering);

2. Thermal ablation: the energy is transferred by the coupling between the electron beam and vibrational and electronic modes in the matter (Ex: PLD in nanosecond pulse width; secondary mechanism in PED);

3. Electronics ablation: the beam interacts with the electrons, create electron-hole pairs, promotes atoms ionization and electrons excitation in the target. (Ex: PED and PLD in lower picosecond pulse);

4. Macroscopic ablation:

    a. Exfoliation: material thin layers are expulse from the target. It occurs in materials with high thermal expansion and high sublimation temperature (higher ablation threshold);

    b. Hydrodynamics: liquid and vapor phases are present simultaneously. In this case the liquid surface tension contrast the gas expansion, generating an equilibrium between the two phases. The partially molten surface area is dragged away by the supersonic gas expansion in low pressures condition (see Figure 2.7). This phenomena is divided into two categories: "super-subsurface boiling", when irregular macro-particulate is ejected from the surface, and "splashing" when there is a surface explosion followed by formation and expulsion of various sized drops (called "droplets").

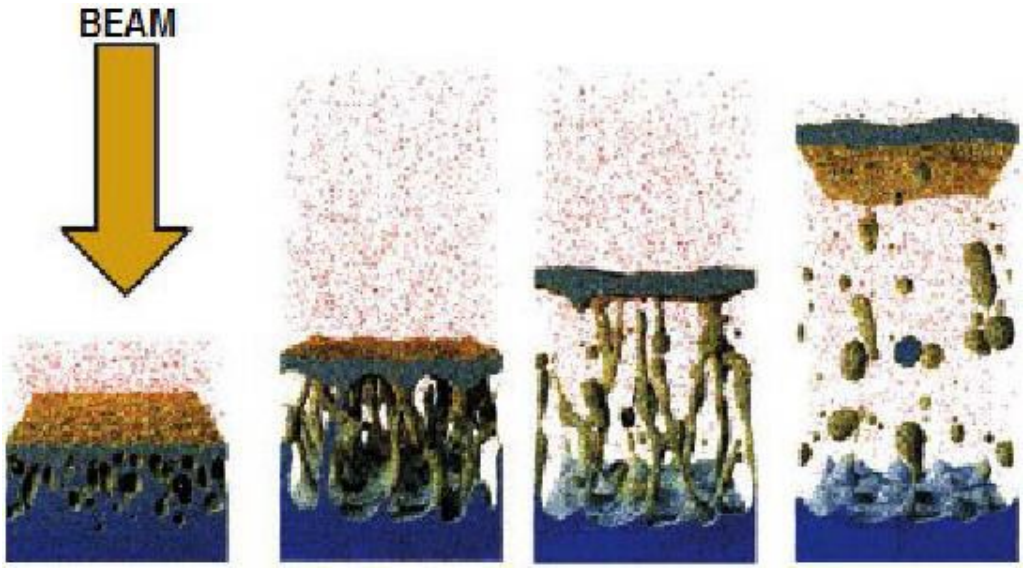

Figure 2.7: Representation of different step of macroscopic ablation phenomena.

All high-energy deposition technique cause macroscopic ablation and thus the deposition of a large number of macro-particles on the substrate. In the PLD these problems are unavoidable and very critical during the film growth. The PED, thanks to the poly-energetic electron beam, is able to generate a pulsed beam, which is absorbed in the very first layers of the target surface reducing the overheating of under-surface region; this means that the subsurface super-boiling and splashing phenomena can be minimized, nevertheless they are always present due to the electrons with energy below the ablation threshold. (see in Figure 2.8 the effect on the film).

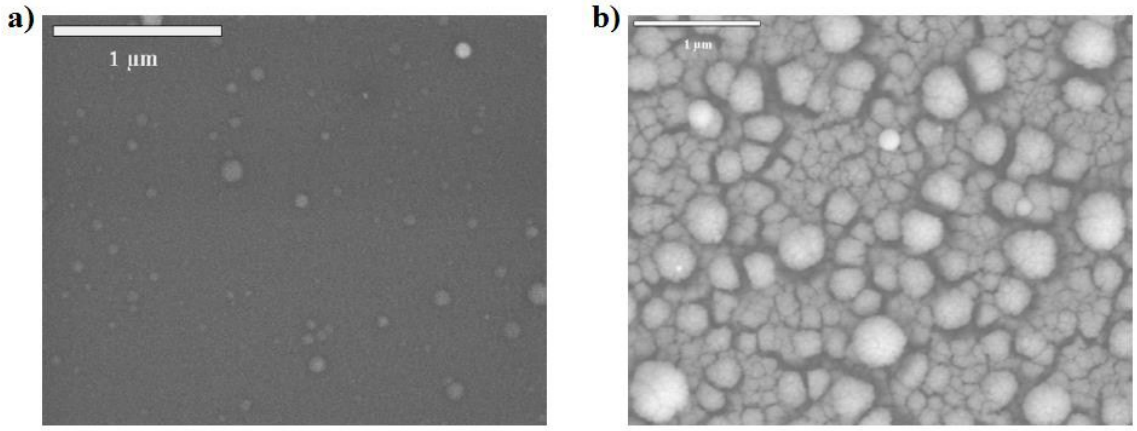

Figure 2.8: SEM images of film surface of $Zr_{0,8}Sn_{0,2}TiO_4$ growth by PED (a) and PLD (b). The comparison show that in the film by PED there is a reduction of particulate density and size [10].

The presence of droplet on the film surface proves that the macroscopic ablation occurred on the target. In high energy techniques, it is impossible to completely prevent their formation, but their average size and density on the film surface can be reduced. Fortunately, not all the particulates create problems for the film morphology, but only the large ones, with size comparable with the film thickness. This part will be discussed in details in Chapter 5.

2.3 PED source time stability

As shown in the previous paragraph, the electrons accelerated at nominal voltage are the most energetic [11]. Those are indeed the faster reaching the target and are followed by slower ones.

In Figure 2.9 the electron flux on the anode is shown at 6 different moments.

In the first phase (a), the pick is represented by the accelerated electrons at the cathode nominal tension (2kV).

In the next phases, the electrons flux maximum moves towards lower energies, increasing the flux itself as shown in Figure 2.10

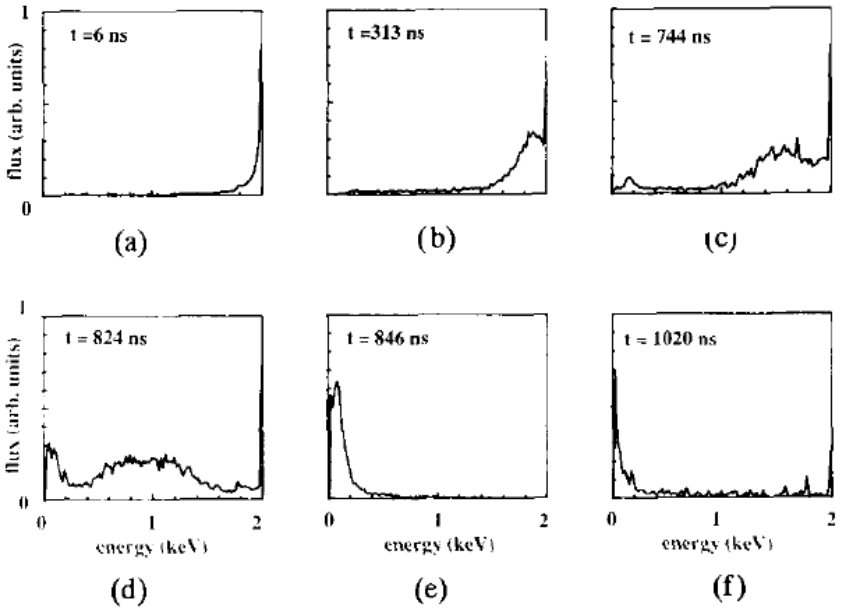

Figure 2.9: Electron flux distribution on the anode at six different times during the discharge formation obtained with the Montecarlo simulations [11].

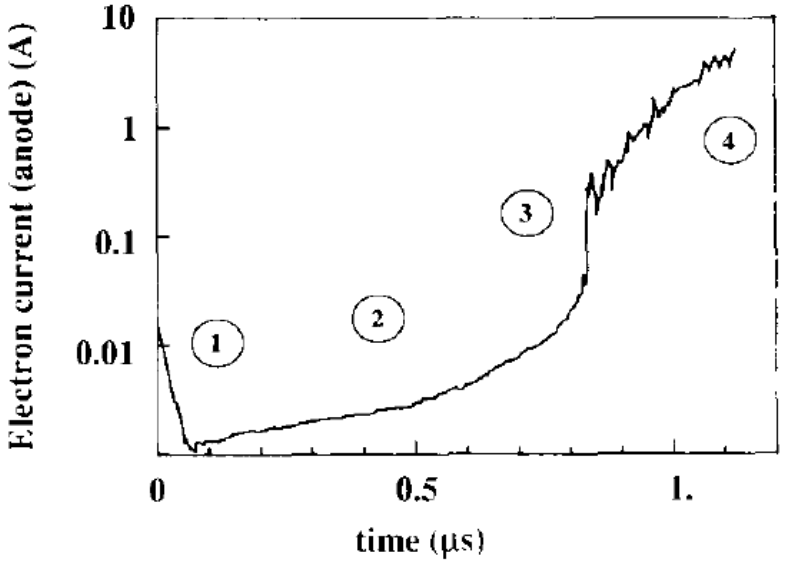

Figure 2.10: Electron flux distribution on the anode at six different times during the discharge formation obtained with the Montecarlo simulations [11].

The electron flux enhancement keeps increasing in time. In fact, PED source during prolonged use overheats some parts involved in the beam generation. In particular, the hollow cathode is very sensitive to this effect that increases during the prolonged use of the PED. A cathode heating causes indeed an electron emission due to the thermo-ionic effect. Those electrons add up to the less energetic part of the beam contribute.

The higher the cathode heating, the greater the thermo-ionic electrons emission is. In order to limit this detrimental effect, commercial sources are usually power restricted reducing the pulse rate depending on the voltage applied, allowing the cathode cooling down between successive pulses.

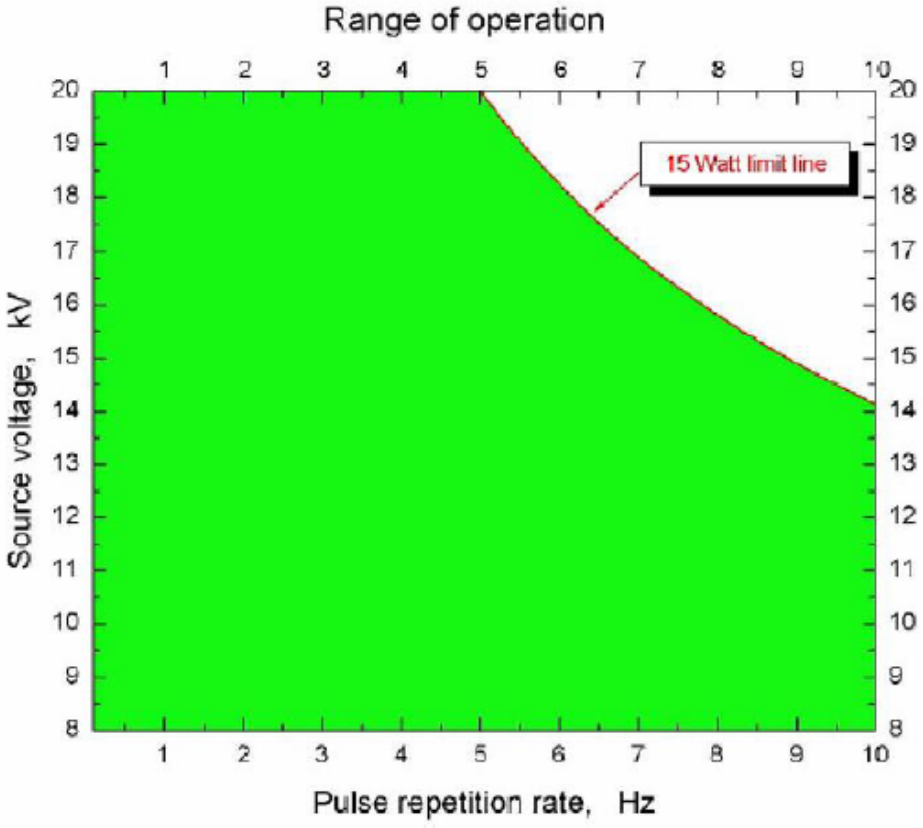

Figure 2.11: Maximum voltage of PED source (red line) as function of frequency [12].

In Figure 2.11 the operation range of a commercial source, (Neocera PEBS 20) restricted at 15 W to avoid the overheating.

The cathode heating can be caused not just by an extended source use, but also by external factors such as the presence of massive heaters in the deposition chamber. The substrate heating is an inevitable part of the process, nevertheless the reduction of all external factors affecting the PED source performances is of primary importance. This topic will be extensively addressed in the experimental part of this thesis (Chapter 4) with the aim of minimizing this issue.

2.4 Angular distribution of the ablated material

The plasma plume generated by the ablation process propagates very quickly in the perpendicular direction to the target surface [3] [11].

The ionic diffusion velocity inside the plasma reaches values of 10^4 m/s and linearly decreases depending on the distance from the plume center, forming a much narrowed evaporation cone compared to a standard thermal evaporation. The ablated material angular distribution is shown in Figure 2.12. The angular distribution can be approximated with a function of $\cos^{2.5}(\varphi)$, where φ is the angle with the target normal direction [3].

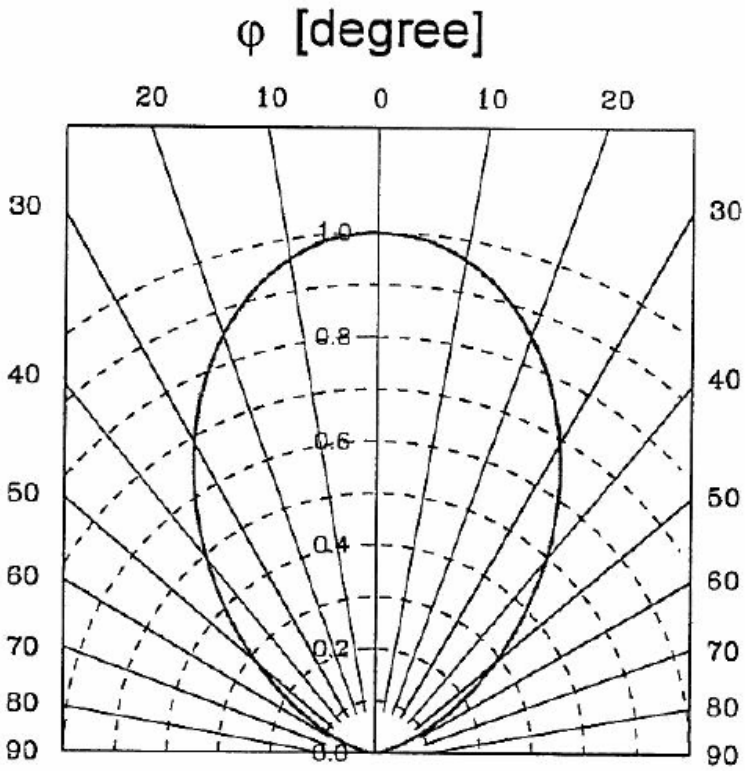

Figure 2.12: Angular distribution of ablated material [3].

Such a narrow distribution of the ablated material reflexes in a likewise narrow thickness distribution on the deposited layer. In this case the distribution on a flat surface, parallel to the target, is proportional to $\cos^{5.5}(\varphi)$.

The thickness uniformity depends therefore on geometrical factors, such as the plume size and its distance from the target. A higher distance from the target improves the deposited film uniformity but drastically reduces the deposition rate. In Figure 2.13 the thickness distribution of a film realized on a flat substrate is shown.

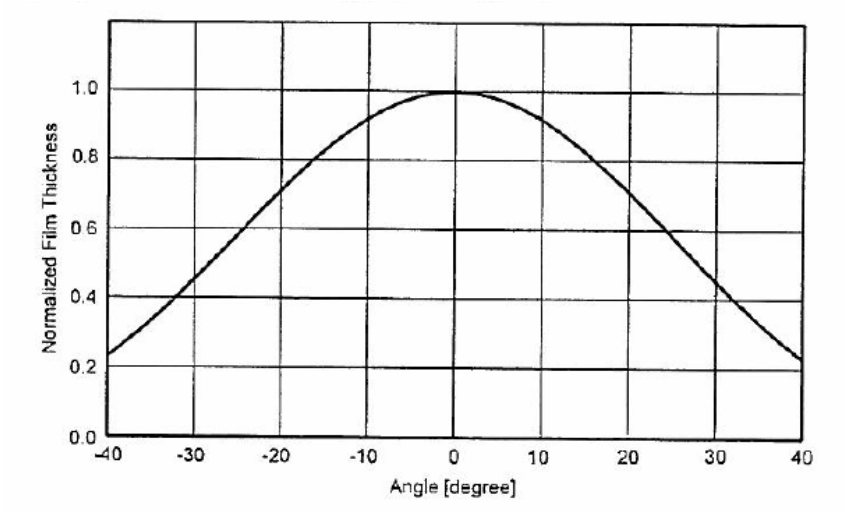

Figure 2.13: Film thickness distribution on a plane surface [3].

This aspect limits the use of the PED technique for applications on small area substrates or at reduced deposition rate. In Chapter 4, the deposition area enlargement, using the combined effect of the different PED sources, will be illustrated.

2.5 CIGS deposition by Pulsed Electron Deposition

In Chapter 1 the characteristics making the CIGS a good material to be used as absorber layer in thin film solar cells discussed; in summary:

1. CIGS is the material with the higher absorption coefficient between those used in thin film solar cells.
2. CIGS has a bandgap that can be varied by changing the In/Ga ratio of the material.

3. It allows to achieve the highest efficiencies among the 2nd generation solar cells

On the other hand, the advantages of the PED deposition of CIGS-based thin film solar cells compared to the other techniques can be summarized as follows:

1. The PED allows to deposit complex materials (such as the quaternary CIGS) in a single stage by using the ablation process independently of phase diagram.
2. The high energy transferred from the electron beam to the target and subsequently to the ablated material allows to reduce the substrate temperature, suggesting the use of thermolabile materials, ideal for flexible solar cells.
3. PED process does not require additional post-growth treatments such as selenization.

In the following Chapters the experimental setup used in deposition process and the techniques used to characterize the CIGS films obtained are described.

References

[1] D. Hariskos, S. Spiering, and M. Powalla, Thin Solid Films, 480 (2005) 99-109.

[2] O. Rau, M. Schmidt, Thin Film Solid, 148 (2001)

[3] G. Muller, M. Konijnenberg, G. Rafft, Deposition by means of pulsed electron beam ablation. in F.C. Matacotta and G. Ottaviani. Science and Technology of Thin Films. s.l., World Scientific, 1995, pp. 89-119.

[4] K.S. Harshavardhan, M. Strikovski Pulsed electron-beam deposition of high temperature superconducting films for coated conductor applications. Second-Generation HTS Conductors. s.l. : Amit-Goyal, 2005.

[5] M. Nistor, N. B. Mandache, J. Optoelectron. Adv., 7 (2005) 1619-1622

[6] T. Zhang, J. Lin, A Patran, D. Wong, S. M. Hassan, S. Mahmood, TWhite, T. L. Tan, S. V. Springham, S. Lee, P. Lee, R. S. Rawat, Plasma Sources Sci. Technol. 16 (2007) 250–256

[7] S. Rampino, F. Bissoli, E. Gilioli, F. Pattini, Prog. Photovolt: Res. Appl. 21 (2013) 588

[8] S. Tricot, et al. J. Phys. D: Appl. Phys., 2010, Vol. 43.

[9] M. Strikovski, K.S. Harshavardhan, Applied Physics Letters, 82 (2003)

[10] M. Nistor, N. B. Mandache, J. Perrière, J. Phys. D: Appl. Phys. 41 (2008) 165205

[11] J.P. Boeuf, L.C. Pitchford, IEEE Trans. Plasma Sci. 19 (1991) 286-296

[12] Neocera operating manual PED source PEBS-20

Chapter 3: Experimental details

The CIGS films were grown using a commercial source PED (PEBS-20 by Neocera Inc.). The source allows to control the growth parameters, such as the acceleration voltage of the electron beam in the range 8-20 kV and the repetition pulse rate, usually settled at 10 Hz. Alumina tubes (3 mm internal diameter) are used for the collimation and the transport of the electron beam to the target. The PEBS-20 is installed in a vacuum chamber; a base pressure of $1x10^{-7}$ mbar is kept before the deposition, while Argon (5N purity) is used at $5x10^{-3}$ mbar working pressure during the film growth. The chamber is equipped with a load lock used for the insertion of the substrates, preventing the vacuum break inside the main chamber. A gate, through which the substrate is moved using a magnetic feedthorugh, separates the chamber and the load lock.

Two distinct graphite susceptors heated by halogen lamps are located inside the chamber, the first is used during the growth process and the second for the post-deposition heat treatments. The sample is heated (from the back side) by thermal radiation, and its temperature is continuously monitored and eventually adjusted during both the CIGS growth and the annealing step.

The targets are glued on a carousel holder facing the PEBS sources, able to host four targets, enabling the sequential deposition of different materials simply by rotating the holder. Each of the four target rotates in order to homogenize the material erosion, leading to a more uniform ablation process; the target rotation speed can be adjusted according to the material and the source's pulse rate.

3.1.1 Targets preparation

All the targets used during this thesis are produced at IMEM-CNR; they can be divided into two categories:

1. Precursor targets: Sodium Fluoride, NaF, typically used to dope CIGS with and increase the carrier concentration. This type of target is obtained by cold pressing NaF powders and by sintering the pellets at high temperature. Dense and compact target are required to increase the ablation efficiency in the PED technique.

2. Absorber targets: CIGS-based targets. A number of different types of absorber targets have been made to investigate:

a. different compositions (variation of the Ga/(In+Ga) ratio, from CIS to CGS)
b. different doping materials (by incorporating Na in the target). The details for using these targets will be explained in details in the following Chapter.

The process targets are synthesized from melt under pressure in a semi-closed system with radiofrequency heating, starting from the constitutive elements (99.999% purity). The grown CIGS ingots are finally cut in slices to obtain the PED targets (Fig. 3.1).

Figure 3.1: Typical 1” diameter CIGS target for PED synthesized at IMEM.

3.1.2 Sample holders

In the deposition chamber the metallic sample holder is placed 8 cm above the target. Depending on the substrate size and the heating mode, different holders have been realized:

1. "Standard" sample holder. They are made of steel, suitable for different substrate sizes and shapes. The most used holders allocate 3 separated 1"x1" (26x26mm^2) square substrates (left side, in Figure 3.2) for conventional (graphite susceptor) heating.

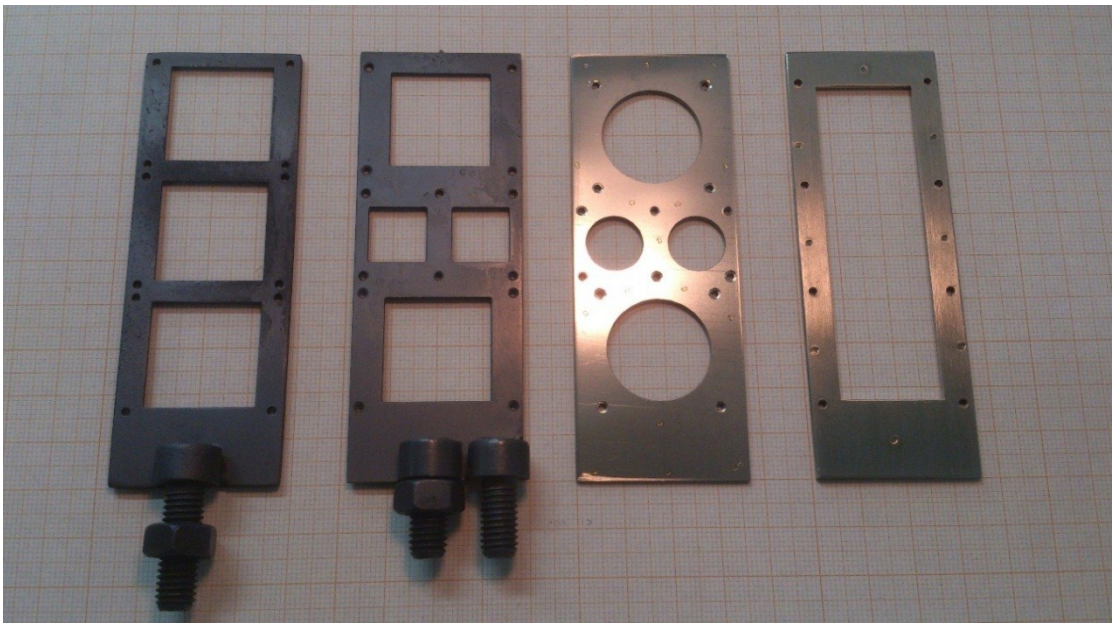

Figure 3.2: Standard sample holders

2. "Joule heated" sample holder. It is essentially a conventional holder with two parallel Cu rods (Figure 3.3), connected to a 0-10V DC voltage generator and contacting a 25x25mm^2 Mo coated-glass substrate. By using this

configuration, the generated DC current is forced to flow across the Mo film, thus heating the substrate (see Chapter 5).

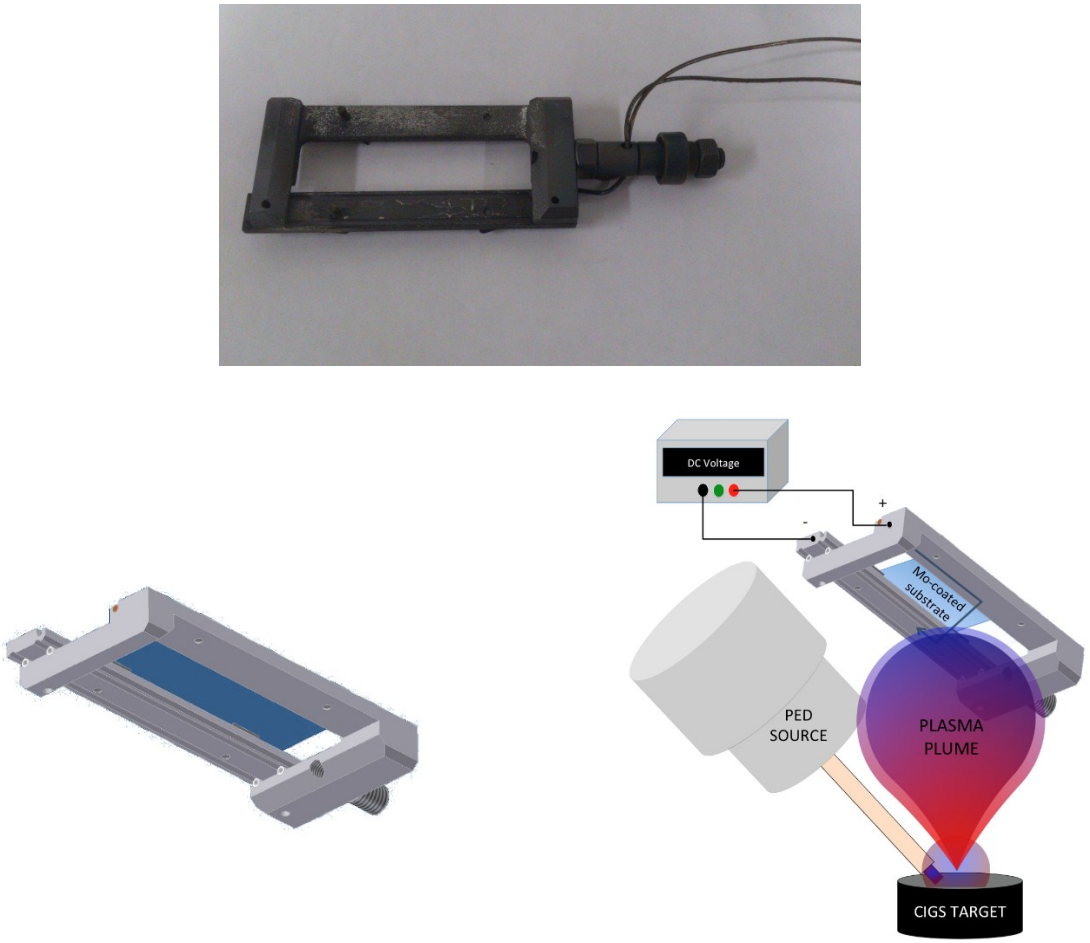

Figure 3.3 – Picture of the Joule heating sample holder (above). Representative scheme of the Joule heating sample holder (left) and the experimental setup (right).

3. “Biased” sample holder: the same sample holder used for the Joule effect heating is employed, but with a different electrical contacts. The contacts are connected to the same voltage with respect to ground (target) in order to create a voltage difference between the target and the substrate without any flow of current trough the substrate.

3.2 Solar cell structure

This section shows the standard structure of the solar cells and the growth processes of the individual layers, as represented in Figure 1.3

3.2.1 Back contact

The first layer of the solar cell is a molybdenum (Mo) film, acting as a back contact. Two types of back contact layers have been used: i) 500 nm sputtered Mo onto SLG substrates and ii) commercial Mo metalized substrate (by Singulus Technologies).

3.2.2 Absorber layer

The CIGS is the absorber layer, grown by PED from the stoichiometric target, as described at the beginning of this Chapter. The growth parameters and the thickness control (1.5 μm has been found to be optimal) will be discussed in the Chapter 4: Experimental results and discussion.

3.2.3 Buffer layer

Cadmium sulfide (CdS) is the typical buffer layer in CIGS-based thin film solar cell; it's grown by CBD (Chemical Bath Deposition), a commonly used technique for its simplicity and low deposition cost. The CdS deposition is preceded by a wet treatment in ammonia (NH_3) solution, primarily to "clean" the surface and to remove the surface oxides. The CdS film grows from a solution of ammonia and ammonium salts to maintain the pH value to 11, while the thiourea and cadmium salt provide the right concentrations of S^{2-} and Cd^{2+} in the 2:1 ratio [1].

3.2.4 TCO layer

The final layer, to electrically and physically close the solar cell, is a thin film of aluminum-doped (2%) zinc oxide (AZO) grown by RF-Magnetron Sputtering, as TCO (transparent and conductive oxide. Both commercial (obtained by HIP, Hot Isostatic Press) and home-made targets (by synthering cold pressed ZnO and Al_2O_3 powders) are used.

A study on the AZO characteristics [2], as a function of the growth parameters (sputtering power, pressure, and distance target-sample), allowed to define the following working conditions:

Power	Argon Pressure	Target-Substrate distance
120 W	$5 \cdot 10^{-3}$ mbar	8 cm

Table 3.1: Optimized settings for AZO deposition process.

The optimized AZO layer (30' deposition time) shows good electrical and optical properties, as reported in Table 3.2.

Thickness (nm)	Resistivity (Ohm*cm)	Trasmittance (%)
890 ± 30 nm	$6{,}7 \times 10^{-4}$ ± $0{,}3 \times 10^{-4}$ Ω·cm	86 ± 3%

Table 3.2: Typical characteristics of AZO layer grown by sputtering.

No anti-reflection coating is deposited on top of the cell.

3.3 Characterizations

The activity of the characterization of the CIGS-based thin film grown by PED can be divided into two main categories:

1. *in-situ* characterizations, to monitor in real time both the chemical composition and the thickness of the growing layer
2. *post-growth* characterizations, to study the properties of the deposited films.

3.3.1 *In-situ* characterizations

Film thickness

During the growth of the CIGS film a pyrometer was used with a twofold purpose. In the most common use, the pyrometer provides the temperature of the substrate from the emitted electromagnetic radiation, while in a less conventional way it gives the real-time measurement of the film thickness during the growth.

The radiation due to the temperature of the heated substrate is monitored using a pyrometer (RAYTEK MARATHON MM), detecting the radiation wavelength = 8 μm. The pyrometer is placed perpendicularly to the substrate surface. By knowing the emissivity of the measured material, the exact temperature of the substrate is measured before the deposition process. The temperature variation of the substrate as a function of time is also a result of a second contribution due to the growing thin film interference. Since CIGS is transparent in the infrared range detected by the pyrometer, the infrared radiation coming from the hot substrate is reflected both at the substrate-CIGS and the CIGS-vacuum interfaces, modifying the optical paths of the infrared photons, reaching the detector with a phase shift. This shift leads to constructive and destructive interference of the detected light intensity, and the position of maxima and minima are related to thickness of the growing film, as clearly visible on the graph time vs. temperature shown in the Figure 3.4.

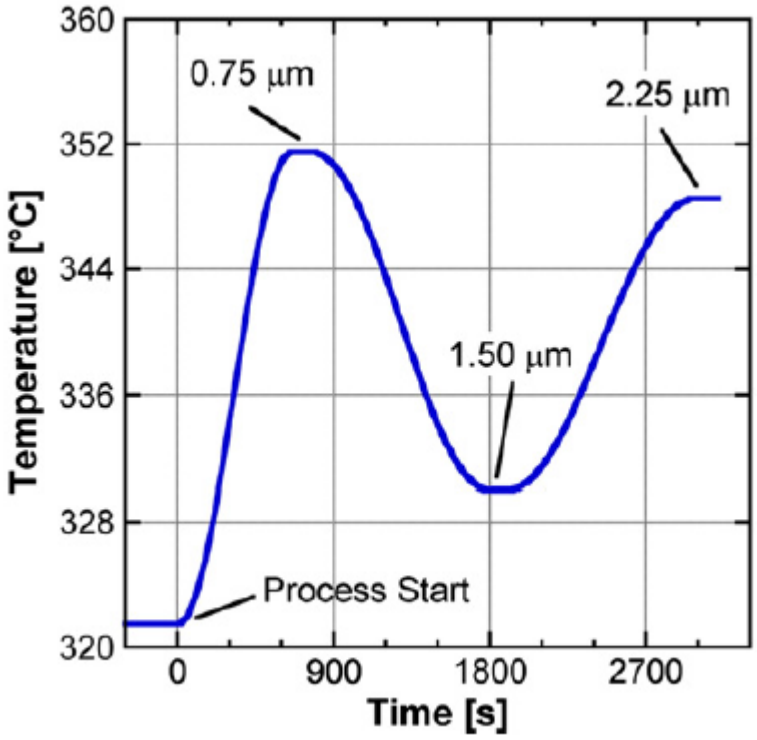

Figure 3.4: In situ measurements of heat radiation from growing CGS films as a function of time. The interference fringe extrema and the relating film thicknesses are indicated.

The thickness, d, corresponds to the maximum and minimum according to the following equations:

$$maxima: d = \frac{(2m+1)\lambda}{4n}$$

$$minima: d = \frac{(2m+2)\lambda}{4n}$$

where *n* is the refractive index of the film, λ (= 8 µm) is the wavelength detected by the pyrometer, and *m* is the order of the maximum/minimum. In the case of CIGS (n = 2.70) the 1st maximum corresponds to a thickness of 750 nm, the 1st minimum at 1500 nm, the 2nd maximum at 2250 nm and so on. Very simply, to achieve the

desired CIGS thickness (1.5 μm), the deposition is stopped on reaching the first minimum.

Thermography

Thermography (FLIR thermocamera T450SC) is used to obtain two-dimensional thermal images; the thermography physical principle is the same as pyrometry, but the signal can be detected from a wider substrate area. The temperature of different regions of the substrate can be simultaneously acquired in real time, thus generating a thermal map of the sample (Figures. 3.5-3.6).

The use of a thermal imaging camera during CIGS growth has a double advantage:

1. It allows the thermal mapping of the substrate to show temperature gradients.

Figure 3.5: Thermo-image of two samples before the CIGS deposition

2. Analogously to the pyrometer it enables to monitor the temperature variations and the thickness in real time during the film growth. Interestingly, it is possible to measure both the local film thickness and a real time map of the thickness distribution.

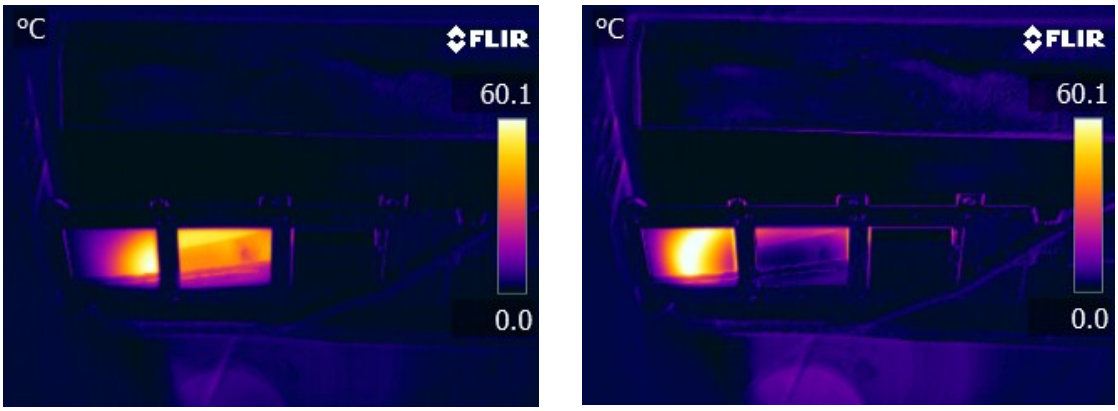

Figure 3.6: Substrate temperature during CIGS mid- (left) and end-growth (right), corresponding to the temperature maxima and minima of interference fringes, respectively.

3.3.2 *Ex-situ* characterization

X-ray diffraction

The X-ray diffraction (XRD) is utilized to analyze the presence of unwanted phases, the crystal structure and quality, and the (preferred) crystallographic orientation of the samples. In the case of CIGS thin films, the structural properties are studied using a Siemens D500 diffractometer, equipped with a Cu Kα X-ray source (λ = 1.54 Å) in the Bragg-Brentano geometry. Possible strain due to lattice mismatch can also be detected by the position shift of the XRD reflections in the pattern.

UV-Vis Spectroscopy

UV-Visible spectroscopic analysis aims to investigate the optical absorption and the reflectivity of the films, using a commercial spectrophotometer (Jasco-155).
UV-Vis spectrometry is also used to calculate the materials optical energy gap; when the energy of the incident light reaches the energy gap (E_g) value in a semiconductor, it starts to absorb the incident radiation, promoting electrons from the valence band to the conduction one (valence-to-conduction band transition).

In direct bandgap semiconductors, such as CIGS, the photon absorption in the bandgap region is defined by the equation:

$$\alpha h\nu = A\left(h\nu - E_g\right)^{\frac{1}{2}},$$

where α is the material absorption coefficient, $h\nu$ is the energy of the incident photons, A is a multiplicative constant and E_g is the value of the energy gap.

The energy gap can be easily derived from the intercept on the axis of the energies of the linear part of the graph $(\alpha h\nu)^2$ as a function of $h\nu$ (the so-called Tauc plot).

The UV-Vis spectrometry is also employed to measure the thin films thickness. In analogy with the methods previously described, the physical principle is the interference phenomenon that occurs when the film thickness have the same order of magnitude of the incident wavelength. The incident radiation is subjected to multiple reflection at the substrate-film and film-air interfaces, leading to a phase shift and hence to constructive and destructive interferences depending on the film thickness.

3.3.3 Electric characterization

Photovoltaic Conversion

The photovoltaic cells technology is based on the photoelectric effect. When a p-n junction is hit by a photon, if it has enough energy, it excites an electron, jumping from the valence band to the conduction band. In this way, an electron-hole pair is created. In absence of an internal electric field, the carriers crosses the barrier between the p and n region to recombine [3].

The solar cell is based on a hetero-junction interface between two semiconductors with different energy gap. The semiconductor with the smaller band gap is known as "absorber". The semiconductor with the largest band gap is known as "window".

The output current of the circuit is:

$$J = J_L - J_D - J_{SH}$$

where J_L is the photo-generated current, J_d the diode current and J_{SH} current shunt. The equivalent circuit of a solar cell is shown in Figure 3.6.

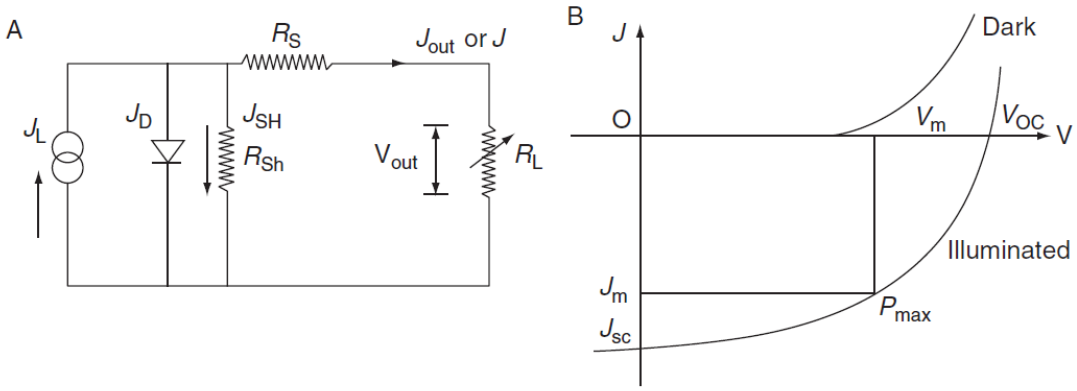

Figure 3.6: Equivalent solar cell circuit (A), J-V characteristics of solar cell under dark and light illumination (B) [3].

The shunt current is equal to:

$$J_{SH} = \frac{V_j}{R_{SH}}$$

The voltage can be written as

$$V = JR_S - V_j$$

Where R_S is the series resistance, V_j is the diode voltage and RSH the shunt resistance. In the dark a solar cell is equivalent to a diode and it can be represented by the Shockley equation:

$$J_D = J_0 \left[e^{\left(\frac{qV_j}{Ak_BT}\right)} - 1 \right]$$

where J_0 is reverse saturation current, q is electron charge, A is diode quality factor, T is temperature and k_B is Boltzmann constant. Using the previous expressions, the equation that describes the operation of photovoltaic cell can be written:

$$J = J_0 \left\{ e^{\left[\frac{q(V-JR_S)}{Ak_BT}\right]} - 1 \right\} + \left(\frac{V - JR_S}{R_{SH}}\right) - J_L$$

The parameters that describe the photovoltaic characteristics of solar cell are four:

1. Open-Circuit Voltage (V_{OC}): It is the voltage measured when J = 0.
2. Short-Circuit Current (J_{SC}): It is the current measured when V = 0. J_{SC} is a function of the photons number that illuminate the solar cell.
3. Fill Factor (FF) is the ratio between the maximum power produced by the photovoltaic cell, corresponding to the product $J_{SC}xV_{OC}$ (Figures 3.6). FF mainly depends from parameters such as series resistance and shunt resistance and describe the cell stability.

   $$FF = \frac{J_m V_m}{J_{sc} V_{oc}}$$

   where J_m and V_m are the current and voltage corresponding to the maximum power point respectively (figure 3.6).
4. Efficiency (η): the efficiency of a photovoltaic cell is described by the equation:

   $$\eta = \frac{J_m V_m}{P_{in}}$$

   where P_{in} is the total input power to the cell.

J-V measurement

J-V measurements are typically carried out under standard lighting conditions: 100 mW/cm^2 with spectrum AM1.5° 25 °C, in order to compare and qualify the photovoltaic cells. To measure the current-voltage characteristic of a solar cell under illumination (using a solar simulator ABET SUN 2000), the voltage is applied to the device and the corresponding current produced is measured.

C-V measurement

The techniques to measure the capacitance are based on the analysis of a p-n junction capacitance variation as a function of the electric excitation. The application of these techniques allows to unveil the electrical properties of semiconductors forming the p-n junctions, such as the concentration profile of the charge carriers, the extension of the space charge region and to study the electrical characteristic parameters (energy and concentration) of deep levels in the space charge region.

References

[1] F. Annoni, Studio degli effetti del Na nelle celle a film sottile di Cu(In,Ga)Se_2 realizzate mediante Pulsed Electron Deposition (PED). s.l. : Material Science Thesis, Università degli Studi di Parma, 2012.

[2] J.P. Garcia, Fabrication of optimized aluminum-doped zinc oxide film as front conctats for CIGS-based solar cells via RF magnetron sputtering. IMEM-CNR Parma - International SERP-Chemistry Master, 2013.

[3] S. R. Kodigala, CIGS BASED THIN FILM SOLAR CELLS. s.l. : Elsevier, 2010. pp. 10

Chapter 4: Results and discussion – Part 1

The main purposes of this thesis have been the study and optimization of pulsed electron deposition technique for the production of efficient and economic photovoltaic cells.

In the course of this Chapter, the following experimental activities and the corresponding results will be shown.

1. Implementation of a low-temperature PED route for the deposition of high quality crystalline CIGS absorber layers, enabling the solar cell fabrication even on flexible and low melting point substrates.
2. A successive research labor is focused on the p-type doping of CIGS films in a low temperature deposition process. Since Na thermal diffusion from the glass, essential to enhance CIGS free carrier concentration and hence the cell efficiency, is hampered at low substrate temperature, an alternative approach based on the deposition of a NaF precursor prior to the CIGS has been tested. The dependence of the electrical properties of both CIGS and the corresponding solar cells are reported in the second paragraph of the Chapter. Thanks to the optimization of the NaF thickness, 15% efficient cells have been obtained on a 0.1cm^2-wide area.
3. A further study concerns the investigation of the role of CIGS post-deposition annealing on the solar cell performance. An optimized CIGS annealing

process enabled a better Na diffusion on large area allowing the enhancement of the cells efficiency up to 16% on larger areas (> 6cm^2).

4. The insertion of an additional layer of undoped ZnO into the solar cell architecture has been found to minimize the influence of resistivity losses on the cell fill factor. Such a solar cell architectures with Fill Factors > 75% and efficiencies > 18% have been obtained.
5. Since theoretical models predict a great efficiency enhancement (up to 28%) if single-crystal CIGS absorber layers are used, the optimized low temperature process has been finally tested also on Germanium epitaxial substrates. The unique structural, optical and electrical properties of single crystal CIGS films grown by PED will be shown.

4.1 Optimization of the substrate temperature

As already mentioned in Chapter 2, the high energy distribution of PED primary e-beam allows a great stoichiometric target-to-substrate transfer of complex multi-elemental materials in a single stage. Moreover the high kinetic energy of PED adatoms allows to deposit ordered layers even at low substrate temperatures. The former peculiar feature of PED technique was capitalized by using quaternary CIGS starting target with the desired final composition. The latter PED distinctiveness was exploited by applying the study of the growth temperature to a very large from room temperature (RT) to 500°C. For better understanding the materials characteristics and in order to find the best growth conditions, targets with different GGI ratios (varying from 0 to 1), have been created. This helped to understand the dependence of the physical properties of CIGS with different GGI ratios on the substrate temperature, thus obtaining the optimized recipe (target composition and temperature). This study is shown below.

Prior to this Thesis, a study about the compositional and structural properties of $Cu(In_{0.7},Ga_{0.3})Se_2$ (GGI = 0.30) depending of the substrate temperature, was already carried out [1]. During this Thesis, the former analysis was completed by ranging the GGI ratio between 0 and 1.

The results are consistent with the study previously carried out, leading to the foremost conclusion that the behavior of compositional and structural CIGS properties on the substrate temperature is substantially independent on the GGI ratio. For this reason the results shown below refer only to the case of CGS films (GGI=1) case [2]. The same trend of the physical properties vs. temperature is followed in the case of starting targets with different CGI ratios.

A list of compositional and structural properties of CGS films deposited on soda-lime glass (SLG), as a function of substrate temperature, T_g, is shown in Table 4.1.

T_g [°C]	Cu/Ga	%Cu	%Ga	%Se
RT	0.71	18.7	26.4	54.9
100	0.79	20.4	25.8	53.8
200	0.76	20.4	26.8	52.8
300	0.77	20.5	26.5	53.0
400	0.94	23.1	24.5	52.4
450	0.92	22.2	24.1	53.7
475	0.96	23.5	24.4	52.1

Table 4.1: Growth temperature and compositional properties of CGS films grown on SLG substrates.

From the compositional point of view, all the samples exhibit a slightly Cu-poor stoichiometry. EDS measurements show that Cu content is dependent on the temperature, increasing linearly from 18.7% to 23.5% by rising T_g from room temperature (RT) to 475 °C. On the contrary, Ga ratio remains very close to the target level of 25% at all temperatures. Consequently the [Cu]/[Ga] ratio is strongly influenced by the sample temperature, as one can see from table 1: lower temperatures promote a reduction of [Cu]/[Ga] ratio value down to 0.71 at RT, while at $T_g \geq 400$ °C the ratio tends to be ≈1, as measured in the starting target. Se concentration is influenced by the substrate heating as well, varying from ≈55% at RT to 52% at 475 °C. The variation of the sample composition vs. T_g is driven by

ablation mechanisms [1]. The sample grown at RT is useful to understand the phenomenon: when the substrate is unheated, the composition of the film reflects the elemental flux inside the expanding plume, hence Se evaporating from the target appears to be in excess with respect to Cu ([Se]/[Cu]=2.9), while Ga content remains substantially constant ([Se]/[Ga]=2.1).

This differential transfer of species has been demonstrated to be due to the typical poly-energetic distribution of pulsed e-beams [3], generated by the PED sources. Depending on the electrical parameters of the source and on the Ar pressure inside the hollow cathode, a continuous energetic distribution of electrons, from few eV to 15 keV, is produced. Faster electrons (>1 keV) are able to penetrate inside the target, releasing on it a very high amount of energy and thus achieving a congruent and stoichiometric evaporation of the material. Slower electrons interact only with the target surface, and the low energy generated by the beam impingement is only able to heat the surface. This leads to a further incongruent evaporation and enhances the presence of Se, the most volatile element, inside the plasma plume. When the substrate is heated beyond the melting point of Se, its surplus in the growing films, subjected to re-evaporation, and the content of this element in the film is reduced. It is important to note that this mechanism induced by PED is proved to be identical to a real-time selenization, since the film experiences a Se vapor overflow during the growth. The employment of a Se overflow is a feature which is common to other physical deposition techniques, such as thermal co-evaporation: whereas in this latter a Se/metal flux ratio higher than 4.5 is requested in order to completely form a single $CuGaSe_2$ chalcopyrite phase, due to the low sticking factor of Se vapor [4], in PED process flux ratios of [Se]/[Cu]=2.9 and [Se]/[Ga]=2.1 are sufficient to grow CGS films, avoiding the formation of secondary metal phases.

From the structural point of view, substrate temperature plays a key role on the enhancement of crystal quality and on the preferential orientation of growing CGS grains. The θ/2θ XRD diffraction patterns of CGS films grown at different temperatures are reported in figure 4.1. An important feature of these samples is the crystalline structure of films even when grown at low temperatures: except the RT-grown film, all the samples deposited at $T_g \geq 100$ °C show a crystalline phase. This aspect is strictly related to the distinctive energetic nature of vapors produced

by ablation techniques: driven by their high kinetic energy (1–10 eV), the impinging adatoms have sufficient energy to reorganize in an ordered way on the growth front surface, leading to the formation of a crystalline arrangement [5].

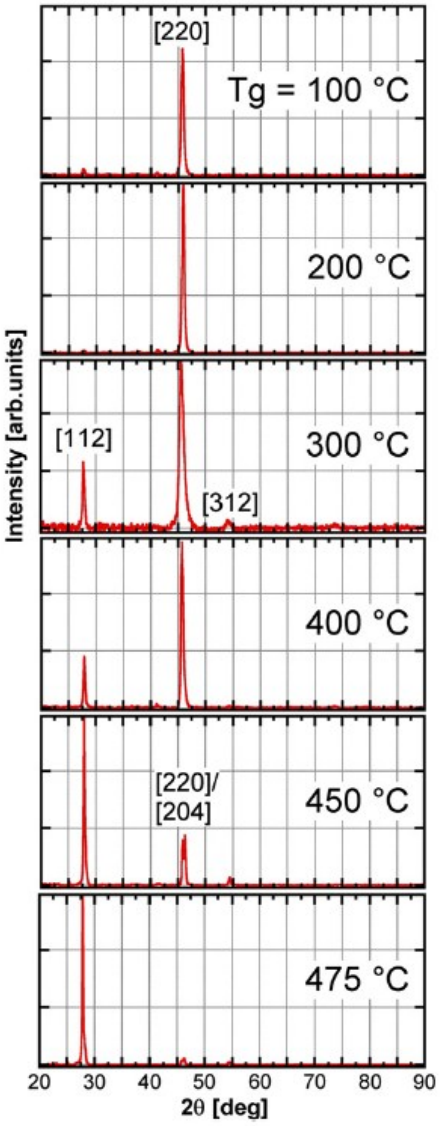

Figure 4.1: XRD patterns of CGS films deposited on glass at different substrate temperatures, T_g, as indicated in the figure [2].

Another peculiar structural aspect of PED-grown CGS films is the dependence of the preferential out-of-plane orientation degree as a function of the substrate temperature. The orientation degree of a layer, $C_{<hkl>}$, along an <hkl> direction (where h, k and l are the Miller indices) is defined from the following formula;

$$C_{<hkl>}(\%) = \frac{\frac{I_{<hkl>}}{I^0_{<hkl>}}}{\sum_{<i>}\frac{I_{<i>}}{I^0_{<i>}}} \cdot 100$$

where $I_{<hkl>}$ is the measured intensity of the <hkl> reflection of CGS, $I^0_{<hkl>}$ is the tabulated intensity [6], $I_{<i>}$ and $I^0_{<i>}$ are, respectively, the measured intensity of the i-reflection and the tabulated one. Depending on the growth temperatures, CGS films are characterized by two preferential orientations, as it is shown from Table 4.2.

T_g [°C]	%C<112>	%C<220>
RT	amorphous	amorphous
100	2.0	98.0
200	1.0	99.0
300	7.0	89.0
400	6.0	92.0
450	29.0	39.0
475	77.0	9.0

Table 4.2: Growth temperature and structural properties of CGS films grown on SLG substrates.

At temperatures between 100 °C and 400 °C, CGS grains are almost totally aligned along the <220> direction, while when the substrate is heated at T_g>450 °C, the <112> orientation becomes preferential,.

The morphological analysis performed by SEM confirms the XRD data about grain dimensions and crystallinity of CGS samples. In Figure 4.2 a comparison about morphological appearance between two samples, grown at extreme conditions, RT and 475 °C, is represented: while at RT the film is completely amorphous (Figure 4.2a), at 475 °C a grain structure is clearly visible: a columnar assembly of CGS grains, with average lateral dimensions of 150 nm, is present (Figure 4.2b).

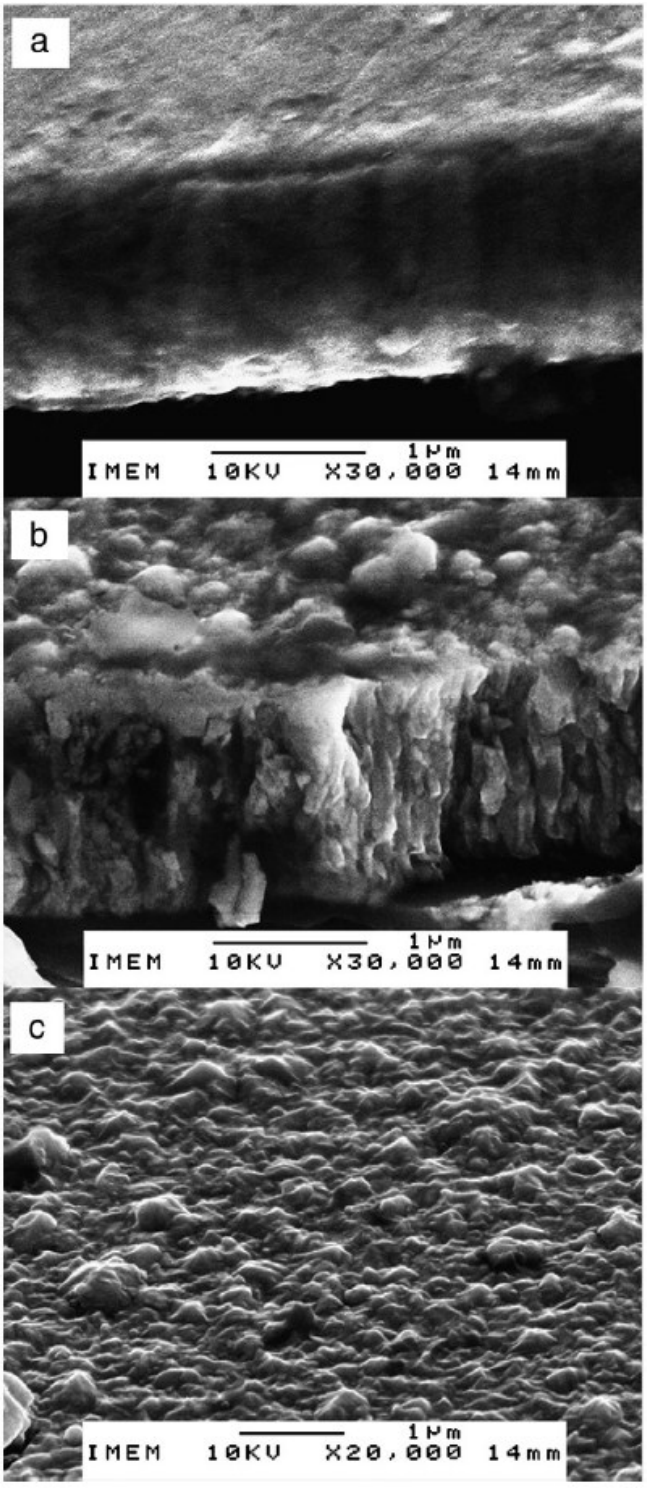

Figure 4.2: SEM images of CGS films deposited at two extreme substrate temperatures: RT (a) and 475 °C (b)–(c). [2]

The analysis of the compositional and structural properties as a function of temperature demonstrated that the crystal quality is strongly correlated with

substrate temperatures. X-ray measurement confirms that temperatures between 200 °C and 400 °C are needed to deposit an oriented <220> polycrystalline film. Compositional measurements show that when the temperature exceeds ≈300 °C the Se content in the film decreases. This can be justified by the Se re-evaporation from the substrate when the temperature exceeds the Se melting point. While in CGS this latter reaches a minimum value of 52% at 475°C, in the case of lower GGI ratio, it decreases well below 50%. As described in Chapter 2, Se-poor films contain a high number of vacancies (V_{Se}) operating as donor centers that compensate the free hole concentration in the CIGS. For this reason a compromise temperature between 250 °C and 300 °C has been selected for growing CIGS films, independently on the GGI ratio.

From the structural properties of the films, it must be noticed that PED technique allows to achieve crystalline CIGS by applying a substrate temperature much lower than the standard methods currently used [7]. This implies that CIGS solar cells could be fabricated by PED at a temperature < 300°C even on low-melting-point plastic and flexible metal tapes.

4.2 Sodium doping in PED deposition

As previously mentioned, the Na incorporation standard method is the thermal diffusion from SLG promoted at high temperature [8]. At temperatures <300°C Na diffusion from the solar cell substrate is hampered, hence an alternative method to allow Na doping in CIGS is required. From the technological point of view, the best Na doping method for PED technique is the precursor approach: a NaF layer is also deposited by PED before the CIGS. This approach exhibits a triple benefit:

1. NaF deposition can be attained using the same vacuum chamber and PED source for CIGS, using a multi-target caroussel.
2. Na is directly diffused into the absorber layer during the CIGS growth process.
3. Na is not forced to diffuse through the Mo back contact.

The precursor layer route enhances the solar cell efficiency with respect to the previous cells made by PED. Using the standard doping method (diffusion from the SLG), high deposition temperatures (500 °C) were needed to reach maximum efficiencies > 7% [1].

Since the properties of PED-deposited films crucially depend on the target morphology and composition, the recipe for the synthesis of NaF target was the result of a thorough optimization process. High-density cylindrical slices of NaF were prepared by a cold pressing process, followed by a powder sintering treatment at 900 °C for 12 h.

The substrates used in this study were made depositing a 500nm-thick molybdenum layer by DC sputtering on a commercial SLG slice (25x25 mm^2 wide and 1 mm thick) at room temperature, according to a bilayer structure described in reference [9]. Prior to the growth process, the substrate is heated at 80 °C. A low e-beam acceleration voltage = 12 kV with a repetition rate = 10Hz was applied for the NaF ablation in order to reduce the droplet generation from the target. Moreover at this voltage a higher precision in the thickness control can be obtained.

Different thicknesses of NaF precursor layer were deposited in order to find the right amount of Na to be embedded into the CIGS film. The NaF thickness was ranged between 0 to 40 nm. The aim was to find the thickness value leading to an optimal doping concentration in the absorber (between $5x10^{15}cm^{-3}$ and $5x10^{16}cm^{-3}$). The NaF thickness was calibrated by an “ex-situ” approach, since no real time measurements are achievable in our PED system and also IR interference cannot give any information about the NaF thickness range taken into consideration (see Chapter 3).

Therefore a post-process calibration was necessary to calculate the growth rate, expressed as nm/pulse. In the first step a NaF film with a thickness of about 1 µm was deposited on glass. In the micrometer range the NaF thickness can be measured by Reflectivity analysis using an UV-Visible spectrophotometer, as described in Chapter 3. Many calibration tests were done using different thicknesses to confirm that the growth rate does not change during deposition. It turned out that

a single PED pulse with an acceleration voltage of 12 kV is able to deposit 0.02 nm-thick NaF film. By dividing the desired nominal NaF thickness (0, 15, 30 and 40 nm, respectively) over the deposition rate value (0.02 nm/pulse), the number of required PED pulses has been calculated. A 1.6 micron-thick CIGS film has been subsequently deposited by switching the target under the PED source CIGS layer and without breaking the vacuum,. The CIGS deposition temperature was kept at 270 °C. The CIGS thickness was monitored during the whole growth using an IR pyrometer, as described in the previous Chapter. The CIGS deposition was carried out by PED using an e-beam acceleration = 16 kV and a repetition rate = 10 Hz. These growth parameters were set to obtain a p-type Cu-poor CIGS film with GGI = 0.30. After the CIGS growth, a 20 minute-long annealing treatment at a temperature of 300°C was made to finalize the sodium diffusion in CIGS layer.

4-point probe measurements using Van der Pauw technique allowed to know the electrical resistivity and to estimate the free carrier density of CIGS films, by considering an electron mobility of 10 cm^2/Vs.

The electrical properties of Na-doped CIGS films grown on glass are reported in the Table 4.3.

PED Pulses	NaF Thickness (nm)	CIGS Resistivity (Ω cm)	CIGS estimated free carrier density (cm^{-3})
0	0	4000	$1.5x10^{14}$
800	15	900	$6.9x10^{14}$
1600	30	100	$6.2x10^{15}$
2130	40	2	$3x10^{17}$

Table 4.3: Electrical properties of Na-doped CIGS films grown on glass as a function of the NaF thickness.

When NaF thickness >30 nm, a detachment of the CIGS film from the Mo surface is always noticed, probably due to the structural weakening of the CIGS caused by an excessive sodium quantity between the crystal grains [10]. Therefore the film is not compact and it is crumbled after a short time exposure in air. From these

experiments an optimum NaF thickness value = 30nm has been found to enhance the CIGS free carrier concentration without affecting the mechanical stability of the multilayer structure.

To better understand the doping process of the absorber layer and the sodium diffusion the experiment was repeated, by depositing different NaF thicknesses and by changing the GGI ratio of CIGS. The table shows the results for CGS films (GGI=1).

PED Pulses	NaF Thickness (nm)	CGS Resistivity (Ω cm)	CGS estimated carrier density (cm^{-3})
1600	30	$6.2x10^{14}$	$6.2x10^{12}$
2130	40	$3.1x10^{14}$	$3.1x10^{13}$
2660	50	1900	$3.3x10^{14}$
3200	60	360	$1.7x10^{15}$
3730	70	70	$8.8x10^{15}$

Table 4.4: Number of PED pulses, NaF thickness and properties of CGS/NaF films grown.

The comparison between the data in Table 4.3 and Table 4.4 indicates that the CGS doping level is lower than that of CIGS, despite the same thickness of NaF layer was deposited. Therefore to obtain a resistivity around 100 Ωcm, suitable for attaining high cell efficiencies, a thicker NaF layer prior to the CGS deposition is needed. These experimental results demonstrate that the sodium diffuses deeper into CIGS than into CGS. This could be due to a higher concentration of Cu vacancies into CIGS compared to CGS, which are the main Na diffusion sites in CIGS [11].

For what concerns CIGS with GGI=0.30, the optimized NaF layer (30nm-thick) was then inserted in the following solar cell architecture: Al:ZnO/CdS/CIGS/NaF(30nm)/Mo/Glass [12].

A 70 nm-thick buffer layer of CdS was deposited on CIGS by chemical bath deposition technique, then the sample was transferred to a second PED chamber for the deposition of a 250 nm-thick TCO of ZnO:Al. No undoped ZnO was deposited between CIGS and TCO. Finally, test solar cell devices were fabricated by evaporating 1.5 mm diameter circular Al top contacts through a shadow mask. The cell size (0.15 cm^2) was defined by mechanical scribing and no antireflection coating was applied. The solar cell architecture is displayed in Figure 4.3.

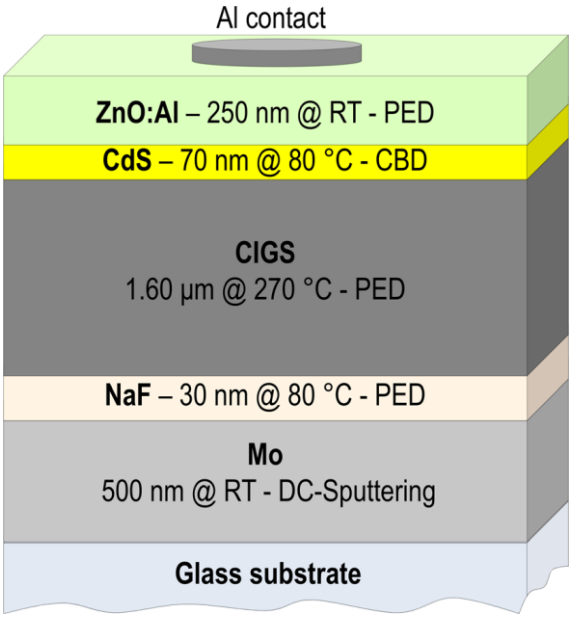

Figure 4.3: Representative scheme of the solar cell architecture: the thickness of the constituent layers, together with their growth temperature and the respective deposition technique are indicated [12].

The net carrier density in the CIGS light-absorbing layer was estimated from the capacitance-voltage (C-V) characterization of the solar cell structure. Figure 4.4 shows the C-V profile at 120 K obtained by using an AC test signal with 25 mV amplitude at a frequency of 1 MHz. At this temperature, only free carriers are expected to respond to the test signal and the "freeze out" of the majority carriers should be negligible [13 14].

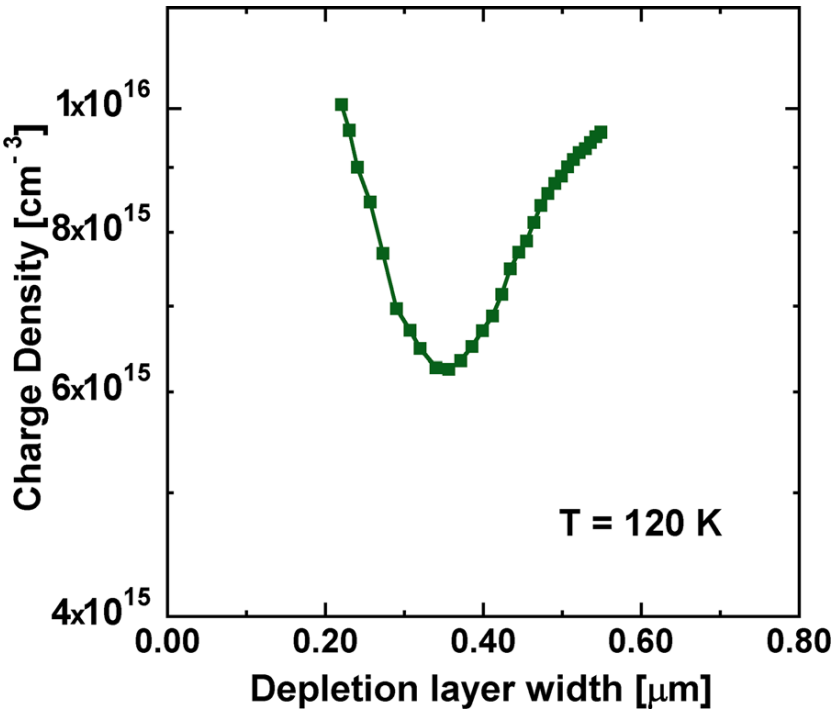

Figure 4.4: C-V profile obtained on the full solar cell stack; the applied DC bias goes from +0.5 to -1 V, the area of the investigated junction is 0.15 cm^2 [12].

Furthermore, to avoid metastability effects, the sample was cooled down with no applied voltage after being kept in the dark for 1 h at 330 K [15].The experimental profile exhibits the typical U-shape with a minimum corresponding to a depletion layer width of about 350 nm. Following the procedure proposed by Cwil [13], the net acceptor concentration N_A is estimated at the minimum of the C-V profile and turns out to be about 6.2x10^{-15} cm^{-3}, in agreement with the value estimated in the corresponding CIGS/NaF/Glass samples (Table 4.3). The apparent increase of the doping level towards the back contact (depletion layer width > 400 nm) could be attributed to the accumulation of static charge in deep acceptors present in concentrations much higher than N_A [13]. Apart from a slightly lower N_A value, the observed C-V characteristic is qualitatively similar to those reported in the literature for high efficiency CIGS solar cells prepared by more conventional growth techniques.

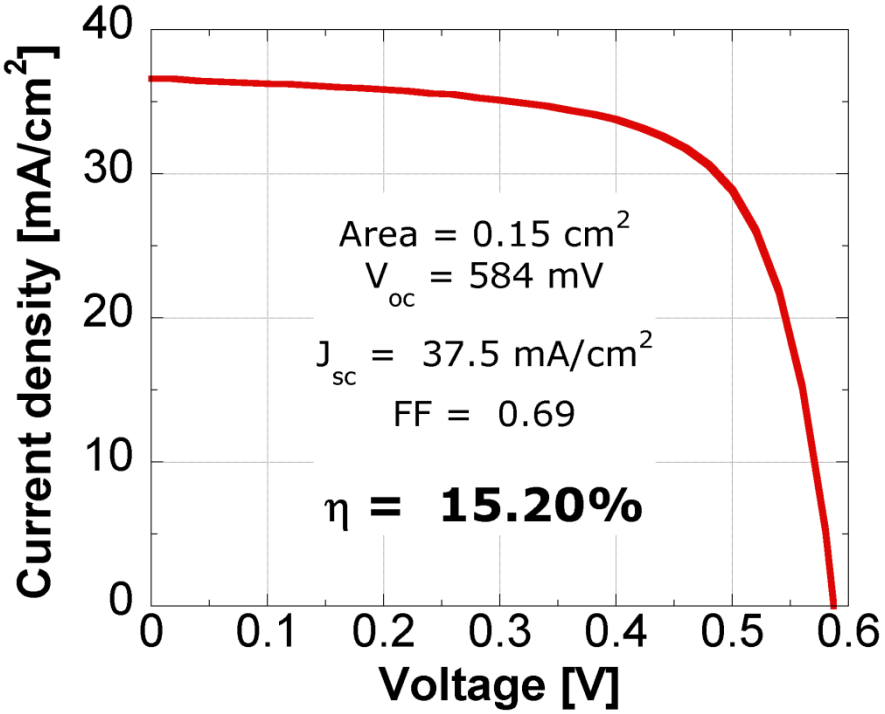

Figure 4.5: Current-voltage characteristics of CIGS solar cells, measured at 25 °C under AM 1.5G (100 mW/cm^2) illumination [12].

Figure 4.5 shows the solar cell J-V characteristic and the parameters are given in the Table 4.5.

Area (cm^2)	Voc (mV)	Jsc (mA/cm^2)	FF (%)	Efficiency (%)
0.15	584	37.5	69.4	15.2

Table 4.5: Photovoltaic parameters of CIGS-based cells fabricated at T_{sub} < 300 °C. The top metal contacts are excluded from the estimation of the illuminated area.

A quantitative electron beam induced current (EBIC) analysis was carried out in a scanning electron microscope fitted with a current amplifier and a high-resolution digital image acquisition system. A sequence of 11 digital maps of the EBIC signal generated by the electron beam while scanning the solar cell top surface were collected at different beam accelerating voltages between 7.5 kV and 32.5 kV at a constant beam current of 30 pA. Each image was processed to obtain a statistical

distribution of the EBIC gain (generated current/beam current) over the 2048x1536 pixels of the map. All the histograms exhibit a narrow Gaussian peak with a FWHM between 6.5% and 10% of the peak EBIC gain. By fitting the peak EBIC gain data to the number of e-h pairs generated by the scanning beam as computed by a Monte Carlo simulation [16], a step-profile of the charge collection efficiency was obtained as a function of depth from the top surface of the cell. The profile shown in Figure 4.6 includes the contribution of both diffusive and depletion region whose width was estimated to be 350 nm from the C-V measurements.

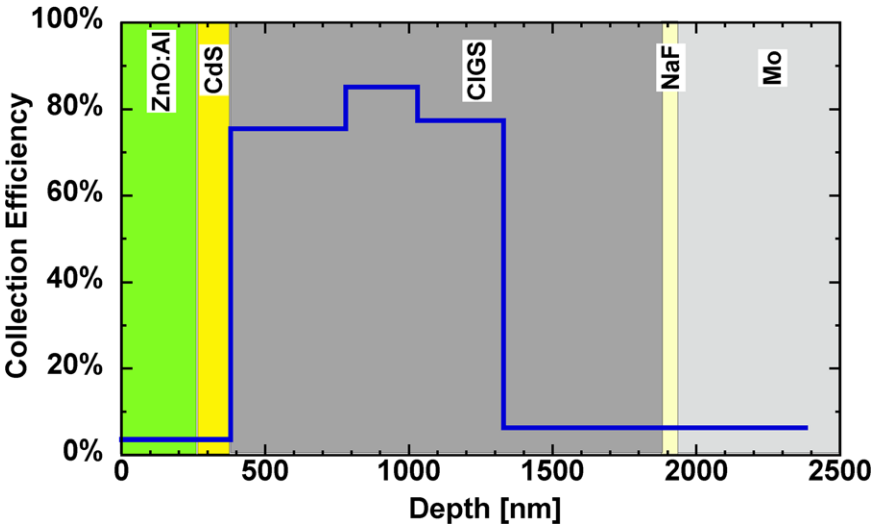

Figure 4.6: Average charge collection efficiency as a function of distance from the top surface of the cell as obtained from EBIC. [12]

The collection efficiency is negligible on the n-side of the junction and reaches a maximum just below 90% at a distance of about 500 nm below the interface between CIGS and CdS. This result not only provides evidence that the CdS/CIGS physical interface acts as a strong carrier recombination center but also indicates that the actual depletion region is located well inside the CIGS layer.

These data demonstrate that efficiencies higher than 15% are achievable by accurately controlling the Na doping into the absorber layer. The use of a NaF precursor layer led to an enhancement of the conversion efficiency (15.2%) with

respect to that obtained using Na diffusion from the glass substrate at high temperature (7.2%). These results obtained by low temperature PED route become comparable to those obtained at high temperature by standard techniques [17], which are based on complicated multi-steps for accurately control the film composition. Otherwise the results of this Thesis activity were obtained by a single-stage stoichiometry transfer process without needing further treatments to correct the chemical composition of the absorber layer. Moreover, the low PED growth temperature < 300 °C, allows the adoption of sodium-free glasses or low melting plastics as alternative substrates.

4.3 Towards 18% efficient solar cells

The efficiency increase in solar cell requires not only an optimized absorber layer, but each individual films in the cell architecture must be engineered. Many challenges as rough morphology, high resistivity and poor transparency of both CIGS and subsequent layers can reduce the electrical performances.

As previously described and confirmed by the results, Na doping is essential for passivating the CIGS grain boundaries: if Na diffusion is not sufficiently induced during the CIGS deposition, recombination shunts can be created at the CIGS/CdS interface. A reproducible Na diffusion from the NaF layer through the CIGS thickness and also a uniform doping content over the whole cell area are then needed to limit resistance losses given by such shunting paths, which lowers the cell performance, in particular the V_{oc}. An improved reproducibility in the Na doping can be attained by applying a correct post-deposition thermal annealing: this activity is described in the first paragraph of this section. Further progress can be succeeded if the shunt resistance of the cell is increased by inserting a high resistance ZnO layer. On the other hand by depositing a metal front contact with the right shape and geometry to compensate resistive losses in the Al:ZnO layer, even J_{sc} and FF can be increased.

4.3.1 Optimization of post-growth annealing process

To minimize the non-uniformity of the solar cell performances, in particular the spread of the V_{oc} values over the whole cell area, Na diffusion process into the CIGS must be engineered even after the deposition process. A post-growth annealing treatment is useful to modify the Na diffusion profile in CIGS. Two main parameters can be tuned during the annealing process: temperature and time. For what concerns the temperature, annealing treatments > 300°C induce the Se re-evaporation from the deposited film, thus leading to the same electrical compensation mechanism described in the previous part. For this reason a maximum annealing temperature = 300°C was kept, while the effect of the annealing duration on the cell performance has been analyzed.

In this study the fabrication of CIGS and the other layers of the cells followed the procedure described in the last paragraph, while only the duration of the post-growth annealing process was varied between 0 (as-grown sample) and 80 minutes. Solar cells with an active area of 4 cm^2 were processed. The J-V characteristics of the corresponding devices are shown in Figure 4.7 and the related cell parameters are summarized in Table 4.6.

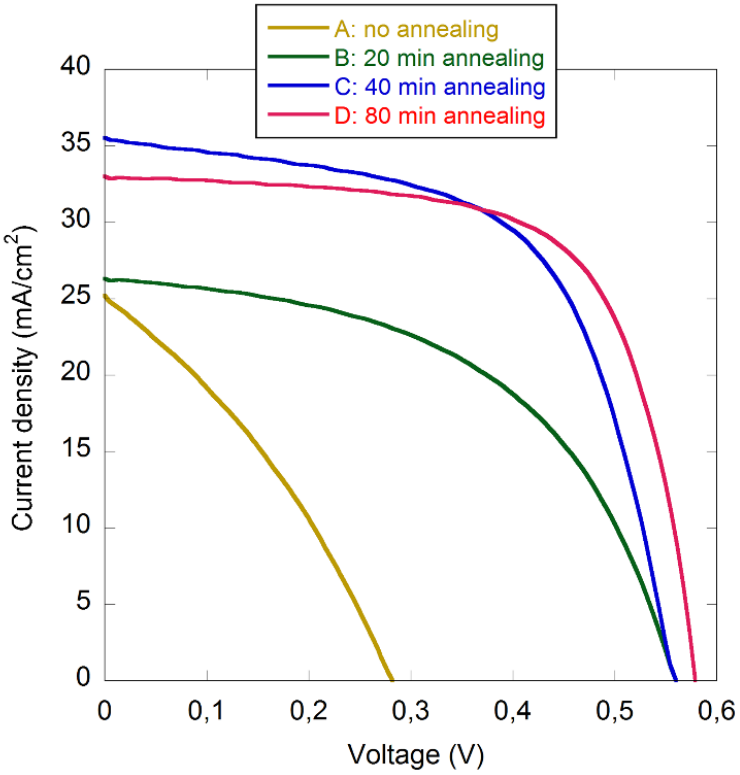

Figure 4.7: Comparison between JV characteristics of different annealed solar cells and not annealed solar cell.

	A	B	C	D
Annealing Time (minutes)	0	20	40	80
V_{OC} (mV)	278	555	555	580
J_{SC} (mA/cm^2)	25.1	26.3	35.3	33.0
FF (%)	33	52	62	67
η (%)	2.3	7.6	12.1	12.8

Table 4.6: Photovoltaic parameters of different annealed CIGS-based cells.

A monotonic increasing of all the cell parameters (J_{sc}, V_{oc}, FF, ETA) by extending the annealing duration can be clearly noticed. In particular the application of the annealing treatment seems to greatly enhance the values of FF and V_{oc}, respectively, with respect to the as-grown sample.

An increase of the annealing time (from 20 to 80 minutes) allows a significant J_{sc} improvement (from 25 mA/cm^2 to 33 mA/cm^2). Annealing time of 80 minutes can further improve the performance due to large area uniformity. In this case efficiency close to 13% on areas of 4 cm^2 was obtained. Certainly longer post-growth annealing treatments increase the cell uniformity over larger areas. In this case 12.8% efficiency over 4 cm^2 wide area must be compared to previous 15.2% efficiency record over an area 25 times smaller (0.15 cm^2).

4.3.2 Structural solar cell improvement: i-ZnO layer

A good crystal quality and thus a large grain size are usually desirable for polycrystalline absorber films, since grain boundaries can act as potential recombination centers for photogenerated electron-hole pairs. This is due to high defect densities, impurity segregation, and carrier collecting fields often found at the grain boundaries [9]. Furthermore, grain boundaries extending from top to bottom of the absorber film can act as recombination paths reducing both the parallel resistance of the device and the V_{oc}.[18]. When these paths are present, the electron charges separated across the p-n junction exploit the former to flow the junction backward, reducing the V_{oc} values across the cell.

To overcome this problem it is necessary to create a high-resistance paths for the recombination current. This has been possible by the insertion of a new high-resistivity thin layer into the cell structure (Figure 4.8).

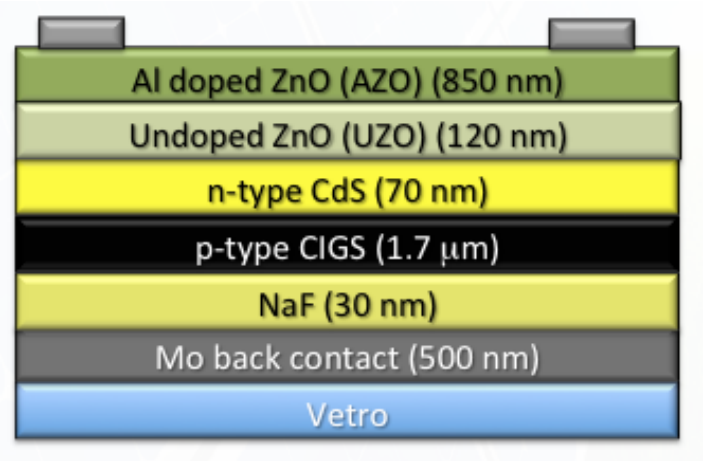

Figure 4.8: Representative scheme of the solar cell architecture: the thickness of the constituent layers.

The presence of an intrinsic zinc oxide (i-ZnO) layer creates a high resistance path along the perpendicular direction to the junction, reducing the shunting currents. Undoped ZnO is a material with a resistivity significantly higher (>10^2 Ωcm) than that of Al:ZnO (<10^{-3} Ωcm), but retaining high optical transparency in the visible range (>90%).

The i-ZnO thin films have been grown by RF-Magnetron Sputtering. The commercial target used is obtained pressing ZnO powders by a Hot Isostatic Press equipment.

The study of the i-ZnO characteristics by varying some growth parameters (such as sputtering power, pressure, temperature and target-sample distance) allowed to obtain a capable recipe to maximize solar cell efficiency by minimizing the effect of the defects present in the material. The main goal was to obtain a very thin ZnO layer exhibiting very high resistivity and optical transmittance > 85% in the visible range. The best undoped ZnO sample was obtained by applying a RF power = 120 W and a Ar background pressure = 5x10^{-3} mbar. Its electrical and optical properties are summarized in Table 4.7.

Thickness (nm)	Resistivity (Ωcm)	Trasmittance (%)
120	>10^5 ohm cm	90

Table 4.7: Standard electrical and optical properties of undoped ZnO layer.

Roughly speaking, if a shunted region or grain is present in CIGS films, such a resistive ZnO thin layer creates an electrical path parallel to the layer surface with a shunt resistance > 10^6 ohm, hindering the presence of parasitic parallel currents. The presence of i-ZnO is automatically reflected on the solar cell performance. In Figure 4.9 the illuminated J-V characteristic of a i-ZnO based CIGS solar cells (active area = 0.1cm^2) is shown.

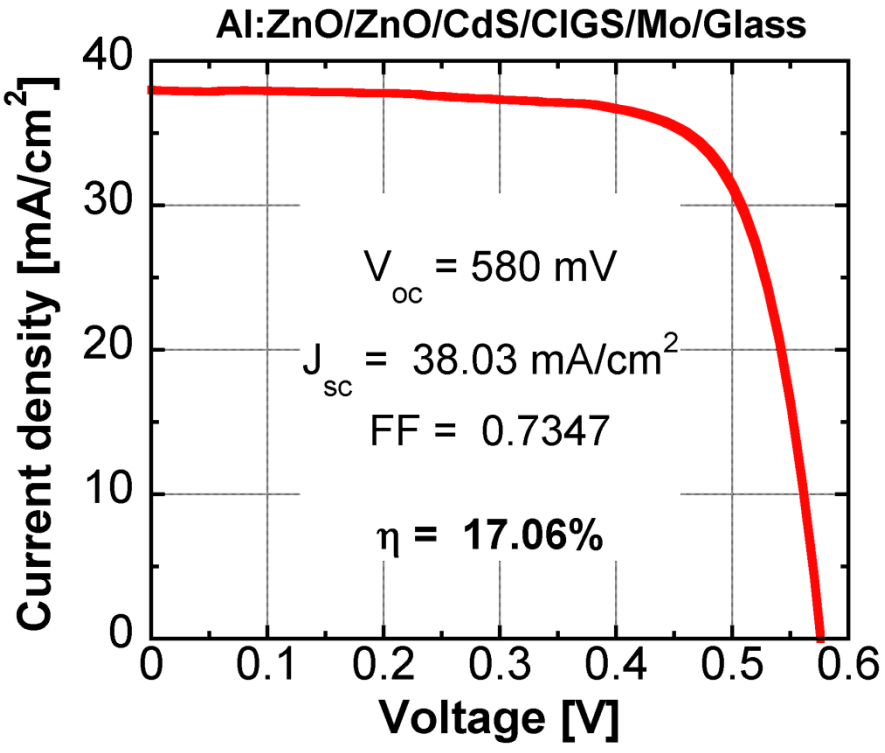

Figure 4.9: Current-voltage characteristics of CIGS solar cells, measured at 25 °C under AM 1.5G (100 mW/cm^2) illumination.

The enhancements of both FF (from 0.69 to 0.73) and J_{sc} (from 37.5 mA/cm^2 to 38.0 mA/cm^2) are the most evident improvements led by the insertion of a i-ZnO layer.

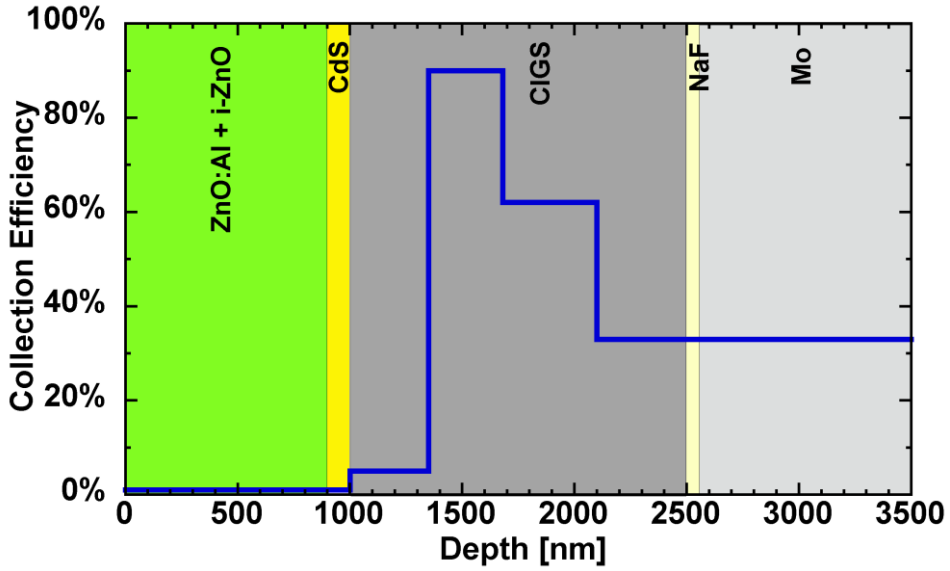

Figure 4.10: Average charge collection efficiency as a function of distance from the top surface of the cell as obtained from EBIC.

By fitting the peak EBIC gain data to the number of e-h pairs generated by the scanning beam as computed by a Monte Carlo simulation, the results are shown in Figure 4.10. Average charge collection efficiency as a function of distance from the top surface of the cell.

Confronting the two figures regarding the charge collection as a function of surface depth in the solar cell at 15% efficiency (earlier descripted) with this one it appears that in both cases the junction does not correspond with the CdS/CIGS physical interface. This result is also confirmed by the CV measurements previously shown. In both cells the depletion region is localized inside the CIGS layer and a maximum charge collection efficiency of about 90%, is observed.

4.3.3 Design of solar cells with η = 18.75%

If Fill Factor values higher than 0.7 must be obtained, the charge collection of the cell must be optimized. To meet this requirement, the quality of cell contacts becomes crucial. In particular the geometry, the position and the size of the top contact must be studied to minimize the effect of the series resistance across the TCO layers.

In order to optimize this point a mathematical model for the power loss minimization [19], depending of the distance covered by the electrons inside the TCO to reach the cell top contact, was used. The power loss is depending of three different contributions.

1. Resistivity of the TCO: the lower the resistivity, the greater the charge collection.
2. Resistance of the contact: depending of the geometry and resistivity of the metal contact.
3. Shadow of the contacts: the presence of the contacts generates a shaded zone on the cell surface

The model used includes a contact geometry with a finger structure. In order to realize the simulation, a resistivity of the TCO of $6x10^{-4}$ Ωcm and a geometry of the contacts composed by fingers in Al ($2x10^{-8}$ Ωm) with a length of 10mm, a width of 100 μm and a thickness of 1 μm, was used. The graph shows (Figure 4.11) the trend of the power loss depending of the spacing between the finger.

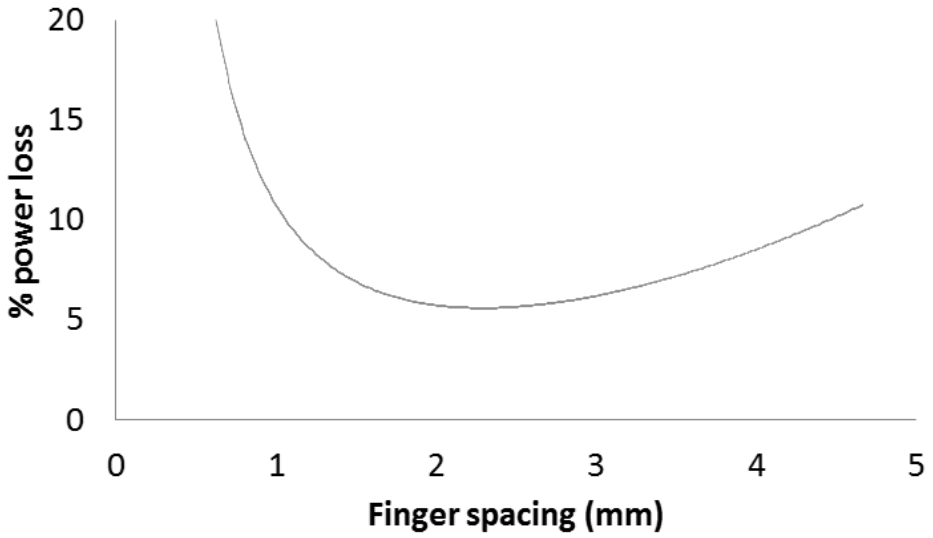

Figure 4.11: Simulated trend of power loss as function of finger spacing.

Following this model, a of 0.15 cm^2 wide cell with a single Al finger, where the maximum distance from the maximum distance between the contact and the cell edges is comparable to the finger spacing minimizing the loss [19], was realized. The J-V characteristic of the best solar cell is shown in Figure 4.12.

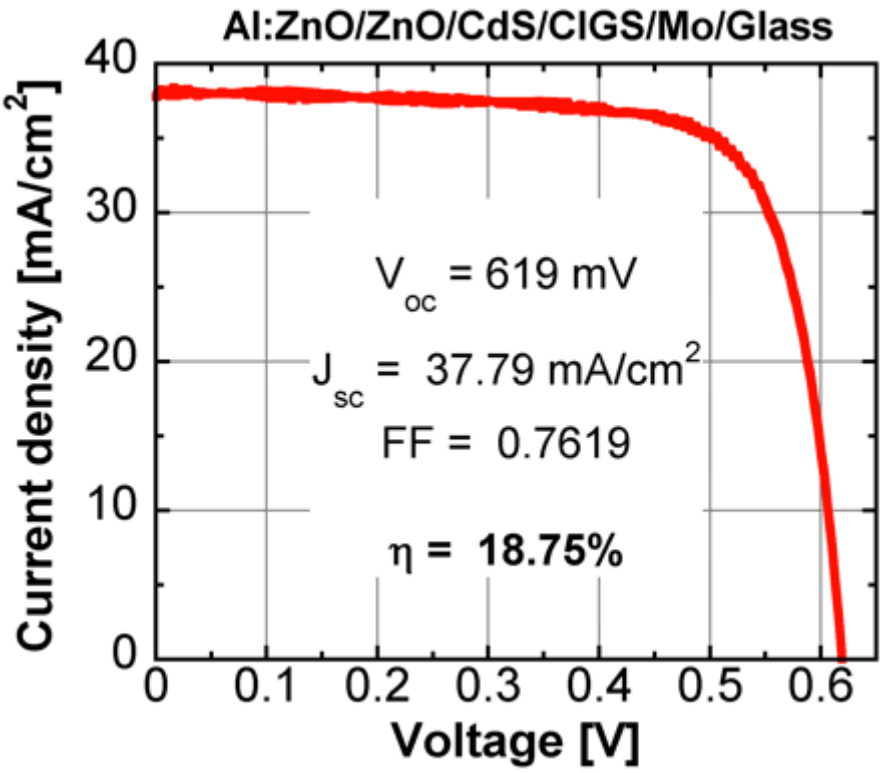

Figure 4.12: Current-voltage characteristics of CIGS solar cells, measured at 25 °C under AM 1.5G (100 mW/cm^2) illumination.

The improvement in FF, from 0.73 to 0.76 is representative of the best efficacy of the charge collection as a result of the optimization of the geometry of the contacts and cell size.

18.75% was the highest efficiency achieved during this work and it is important to take into account that has been achieved by using an innovative technique that allows CIGS absorber layer deposition in a single stage and at temperature 200 °C lower than the standard fabrication conditions. In addition, the result was achieved by depositing a CIGS layer uniformly without any compositional grading into the film.

4.4 Wide area uniformity increase: 6cm^2 area solar cell

By exploiting the results obtained studying sodium diffusion and the improvement due to the i-ZnO layer, it was possible to analyze the photovoltaic characteristics performance as function of the area. In Figure 4.13 the picture of the cell achieved for this work is shown. A 2.5x2.5 cm^2 size solar cell was created. To cell growth was used a prolonged annealing, 80 minutes to improve the maximum sodium diffusion. Following, after CdS deposition, 120 nm thick i-ZnO was deposited to minimize the shunt effect of in the cell.

The electrical characteristics uniformity of the cell was studied by dividing the area into 16 sub-cells of equal size (0.18 cm^2), aluminum contact was deposited on each cell to improve the charge collection, as shown in Figure 4.13.

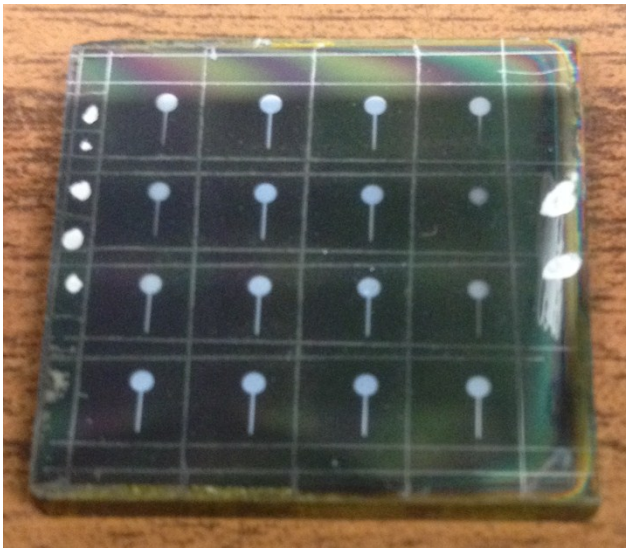

Figure 4.13: Picture of 16 sub-cells of equal size (0.18 cm^2).

η=14.71%	**η**=15.57%	**η**=15.23%	**η**=14.44%
η=15.79%	**η**=16.23%	**η**=17.33%	**η**=16.38%
η=16.33%	**η**=16.76%	**η**=17.50%	**η**=16.40%
η=16.29%	**η**=16.51%	**η**=16.86%	**η**=15.97%

Table 4.8: Efficiency of the 16 different solar cells displayed in figure 4.13

The table shows the 16 cells efficiency. The uniformity over the entire area of 6 cm^2 is very good, there was an average efficiency of 16.02±0.78%. Other average parameters are V_{oc}=574 ±8 mV and J_{sc}=36.9±1.4 mA/cm^2. Fill factor of 71.8±1.5% confirms the excellent uniformity over the entire solar cell.

The data show that during this work, in addition to high efficiency, 18.75%, on a small area (0.1 cm^2) also a great efficiency has been reached on a large area (6 cm^2).

4.5 Efficiency increasing by growing single-crystal CIGS

Even though the current efficiency record for CIGS devices is 21.7% [20], these results are still quite far from the Shockley–Queisser theoretical limit of 33% [21]. Despite extensive work carried out on the loss mechanisms in CIGS solar cells to achieve the theoretically predicted limit, this topic is still under intense debate. The most relevant losses are related to the following effects [22 23]:

1. Shockley–Read–Hall recombination in the space charge region and at the grain boundaries
2. Bandgap fluctuations induced by lateral stoichiometry non-uniformity

3. Low electron mobility due to impurity scattering and band bending at charged grain boundaries
4. Fluctuations of the electrostatic potential caused by extended defects such as dislocations and grain boundaries.

Although the beneficial role of grain boundaries as hole barriers in polycrystalline films is widely accepted, their presence induces strong fluctuations on the electrostatic potential, leading to an increase of the diode saturation current and to the consequent net reduction of the open circuit voltage [22 23].

For these reasons is important to investigate the role of the CIGS crystal structure and grain size on the solar cell performance. Three-dimensional model for ZnO/CdS/CIGS/Mo solar cells to be included in Sentaurus Technology Computer Aided Design (TCAD) semiconductor device simulation tool was studied [24]; the simulations strongly indicated that the cell efficiency would benefit from larger grain size over a wide range of values of the photogenerated carrier's surface recombination rate, both at the CdS/CIGS heterojunction(Sn), and at the grain boundaries(V_r), as summarized in Figure 4.14.

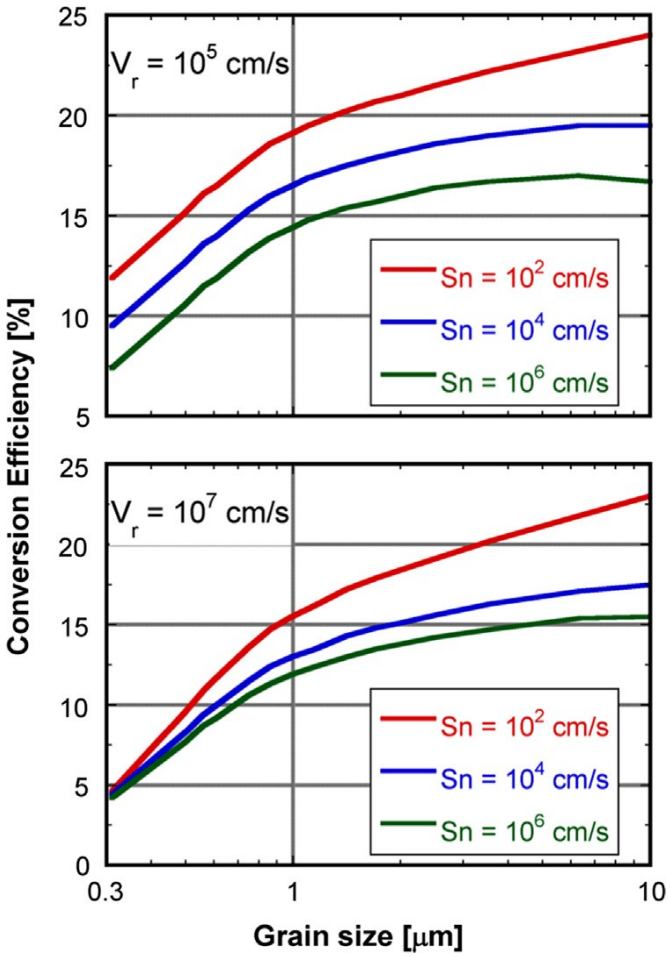

Figure 4.14: Conversion efficiency versus grain size for different surface recombination rates at the CdS/CIGS heterojunction (Sn). The efficiency trends are simulated for two different recombination velocities at the grain boundaries, V_r=10^5 cm/s (top) and V_r=10^7 cm/s (bottom).

The results suggest that significantly improved solar cell absorbers can be expected from single crystal CIGS films [25], obtainable only by epitaxial growth on substrates with reduced lattice mismatch. GaAs has been exploited as epitaxial substrate in literature [26 27]: from these studies, it turned out that substrate temperatures above 550°C were found necessary for the epitaxial growth of CIGS by Molecular Beam Epitaxy (MBE) and Metal Organic Chemical Vapour Deposition (MOCVD) techniques [28]. In this case the epitaxial deposition of CIGS films on Germanium wafers at low substrate temperature (300 °C) by the PED technique was studied.

Germanium was chosen as epitaxial substrate alternative to GaAs, because of:

1. Its lattice parameter (a=5.652 Å) that yields a lattice mismatch <1%
2. Its similar thermal expansion coefficient ($5.8x10^{-6}$ K^{-1})
3. Its capability to act as low-bandgap absorber in a hypothetical CIGS/Ge-based tandem solar device.
4. Its possibility to be realized as virtual substrate, thus reducing the costs of wafer substrates.

PED technique was proven to be a viable route for depositing high-quality CIGS: in previous paragraph reported 15%-efficient CIGS-based solar cells fabricated by PED on Mo-coated glass substrates at 270 °C. The above mentioned TCAD simulations are in good agreement with the experimentally measured photovoltaic parameters, the efficiency value expected being ≈15% (average grain size ≈1 μm and Sn and Vr≈10^5 cm/s).

As substrate, n-type Ge wafer (100) (n=$1x10^{17}$ cm^{-3}, 15x15 mm^2 wide) with a 6° miscut towards [110] has been used, treated in diluted hydrofluoric acid for removing the surface oxides. The substrates were placed 8 cm away from the target, under a graphite susceptor heated by halogen lamps and its temperature was kept at 300 °C and monitored by a thermocouple. Analogously to the solar cells deposited on Mo-coated glass by PED, the thickness of CIGS films was ≈1.5 μm.

The XRD patterns of CIGS films grown on Ge at 300 °C in comparison with a typical polycrystalline CIGS deposited on Mo/Glass under the same conditions are shown in Figure 4.15. While the polycrystalline CIGS/Mo/Glass pattern exhibits the expected preferred grain orientation along the (112) direction [1], only the (008)-CIGS and the (400)-Ge reflections are observed in the case of CIGS/Ge, thus confirming epitaxial growth of CIGS on (100)-Ge.

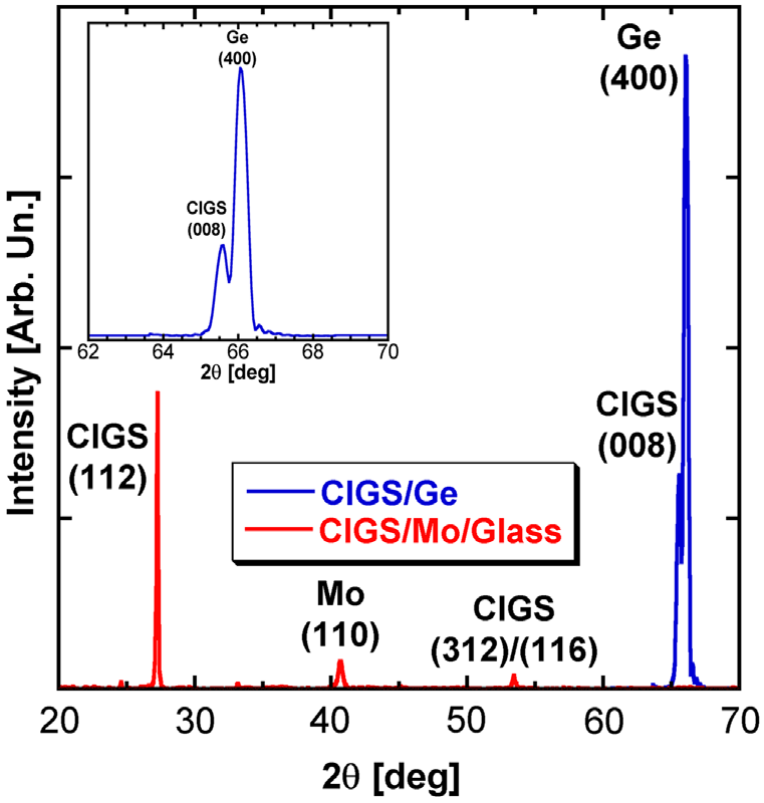

Figure 4.15: XRD patterns of an epitaxial CIGS/Ge heterostructure (blue line) and a typical polycrystalline CIGS/Mo/Glass (redline) grown at the same temperature =300 °C. The inset shows a close-up of the CIGS/Ge diffraction pattern.

By analyzing the position of the (008)–CIGS peak, a lattice parameter c=11.383 Å of the CIGS tetragonal phase can be calculated. The achievement of the epitaxial growth of CIGS on Ge at such low temperature is a noteworthy result when compared with literature [25 26 27] where substrate temperatures larger than 550°C were found necessary for epitaxially growing CIS and CIGS films by traditional deposition techniques as MBE and sputtering [29 30]. High Resolution Transmission Electron Microscopy (HRTEM) analysis confirms the epitaxial growth at the CIGS/Ge interfaces, Figure 4.16a. The corresponding Fast Fourier Transform (FFT) image shown in the inset reveals the presence of a perfect epitaxial relationship CIGS(001)//Ge(001), with a lattice mismatch within the instrument sensitivity (≈1%). Neither dislocations nor Kinkerdall voids, commonly noticed in CIGS/GaAs systems [26 28 31], are observed.

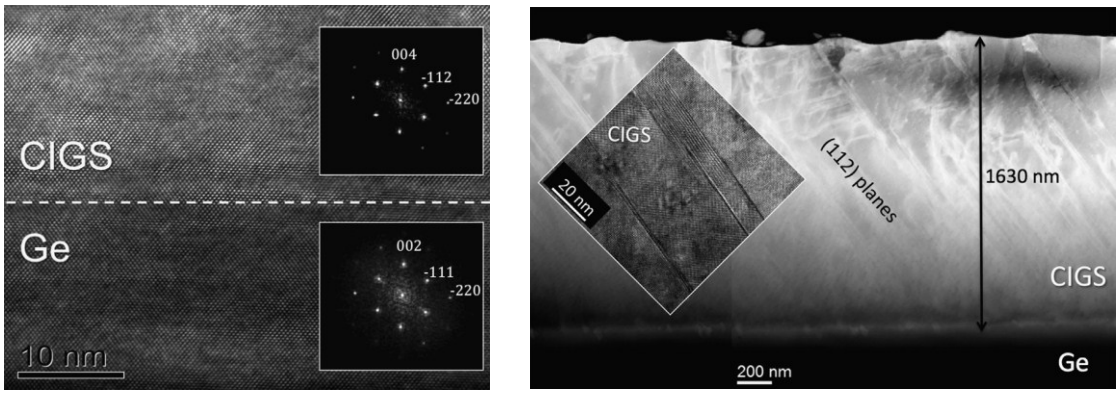

Figure 4.16a: HRTEM image of the CIGS/Ge interface. The insets show the corresponding FFT patterns. Figure 4.16b: HAADF cross-sectional image of the CIGS/Ge structure. The inset shows a HRTEM image of the twin boundaries along the (112) direction.

The High-Angle Annular Dark-Field (HAADF) cross-sectional image of the sample reported in Figure 4.16b confirms that the single crystal structure is preserved over the whole CIGS thickness. Twin boundaries along the (112) direction start to appear at ≈300 nm from the CIGS/Ge interface: these defects have been noticed also in Cu(In,Ga)Se_2/Si heterostructures, and their origin seems to be related to the relaxation of lattice strain accumulated during the growth process [32]. EDS measurements reveal a strong Ga and Cu gradients along the CIGS thickness, with Ga/(In+Ga) (GGI) and Cu/(In+Ga) (CGI) ratios starting from 0.54 and 1.13 at the interface, respectively, and decreasing to 0.30 and 0.85 near the CIGS surface, these trends are showed in Figure 4.17.

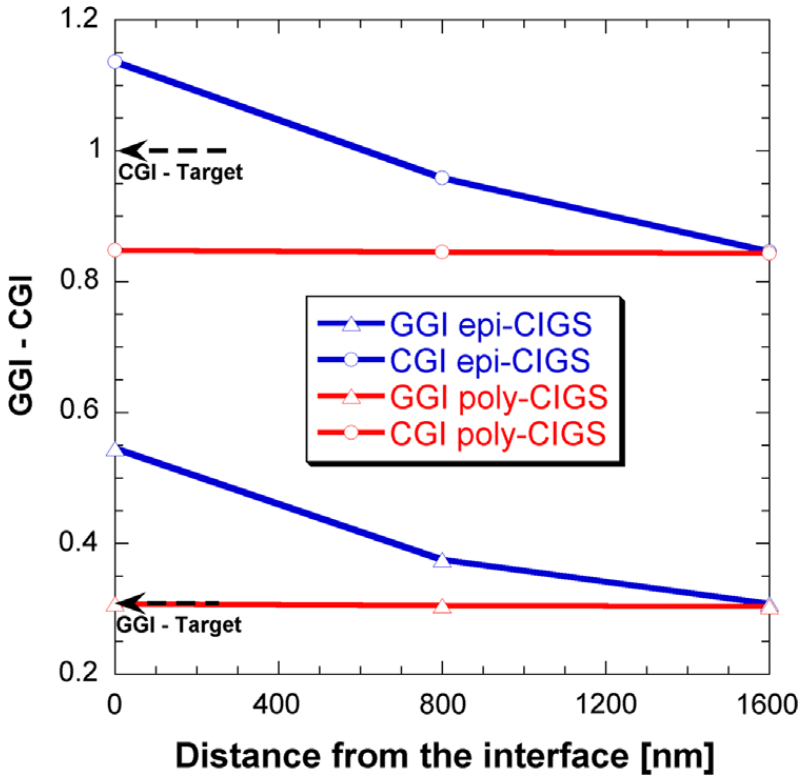

Figure 4.17: Distribution of GGI and CGI ratios along the CIGS thickness in both epitaxial and polycrystalline films. The dashed lines indicate the values of the two ratios in the starting CIGS target.

This Ga enrichment at the interface has been already observed in literature at the epi-CIGS/GaAs interface and it was explained in terms of Ga out-diffusion from GaAs [22 26]. Ga contamination from the substrate is clearly ruled out in this case. Since in CIGS/Mo/ Glass samples, neither GGI(=0.30) nor CGI(=0.85) undergo a variation along the whole CIGS thickness, it can be inferred that in CIGS/Ge system the chemical composition of the layer is self- adapted in order to minimize the lattice mismatch with the substrate. Indeed, for GGI=0.54, the corresponding calculated lattice mismatch with Ge becomes < 0.5% [26]. This effect could explain why misfit dislocations were not detected at the hetero-structure interface.

Photoluminescence spectra of CIGS/Ge taken at 10 K exhibit a dominant narrow symmetric peak centered around 100 meV below the band edge =1.17eV, Figure 4.18, calculated on the basis of the GGI ratio value at the surface = 0.30 [33].

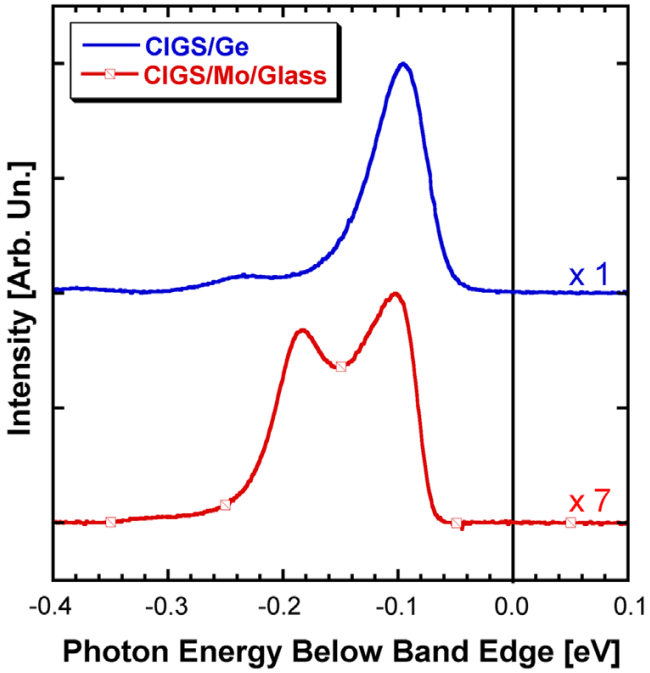

Figure 4.18: Representative PL spectra of CIGS/Ge (up) and CIGS/Mo/glass(down) samples, grown at the same substrate temperature =300 °C. The spectra were taken at 10 K.

The average FWHM value of the peak is ≈55 meV. This emission is usually ascribed to a donor–acceptor pair (DAP) emission related to V_{Cu} and V_{Se} levels [34]. This PL spectrum is very similar to that measured on $CuInSe_2$ epitaxial films grown at 660 °C on (100)-GaAs wafers [35]. On the other hand the PL spectrum of CIGS/Ge appears slightly different from that of polycrystalline CIGS/Mo/Glass grown at the same substrate temperature, where two distinct emission peaks are visible. While the peak at higher energy can be associated with the same DAP $V_{Se} \rightarrow V_{Cu}$ transition of CIGS/Ge, the latter is usually attributed to the $In_{Cu} \rightarrow V_{Cu}$ transition [34]. The absence of a radiative recombination due to the In_{Cu} antisite in CIGS/Ge confirms a lower density of cation substitutional defects in epitaxial CIGS with respect to polycrystalline layers. Other relevant differences between epitaxial and polycrystalline CIGS concern:

1. The intensity of the PL emission, stronger by a factor of 7 in CIGS/Ge

2. The spatial uniformity of the spectra: while in polycrystalline CIGS the relative weight of the two peaks changes considerably along the sample area, the shape of the PL spectrum of the CIGS/Ge is unchanged over different regions of the sample.

This latter confirms a higher compositional and structural uniformity of the epitaxial CIGS material in comparison with the polycrystalline one.

For the CIGS/Ge heterojunction electric measurements, ohmic contacts were thermally evaporated both on CIGS (860 μm-diameter Au dots) and on n-type Ge (AuCr stripes).

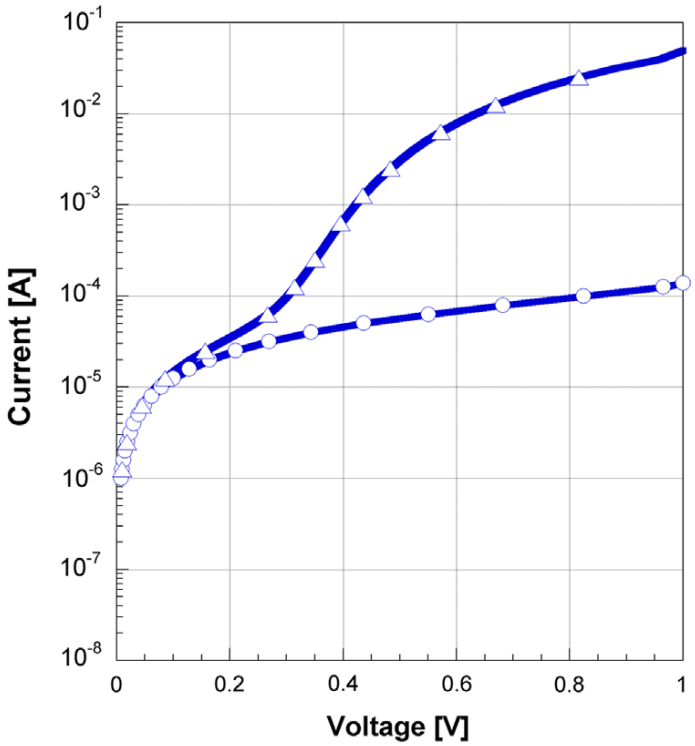

Figure 4.19: Forward (triangles) and reverse (circles) bias current–voltage characteristics of the CIGS/Ge heterostructures.

Figure 4.19 shows the current–voltage characteristics of the CIGS/Ge heterostructure at 300 K. The good rectifying properties of the device confirm the

intrinsic p-type conduction in CIGS layer, forming a good heterojunction with the n-type Ge substrate. The sample shows a high spatial uniformity, since similar I–V characteristics have been obtained over different regions. The calculated diode ideality factor is ≈1.98. The space charge density profiles calculated from C–V curves at 300 K of epi-CIGS/Ge diodes and ZnO:Al/CdS/poly-CIGS/Mo solar cells are compared in Figure 4.20.

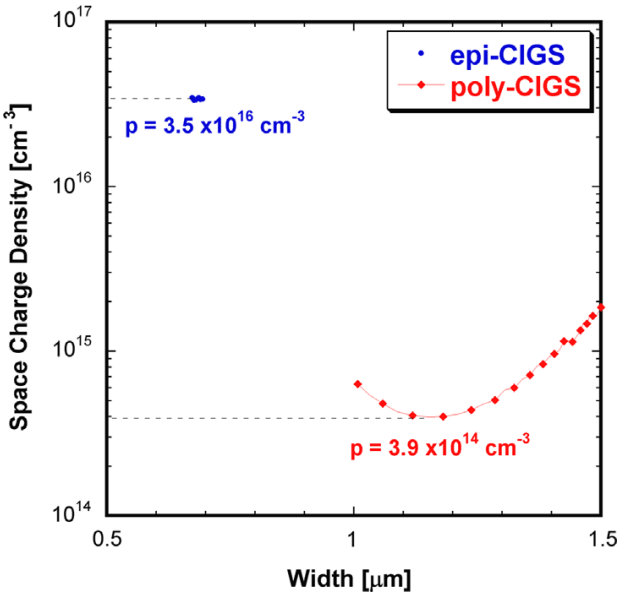

Figure 4.20. Space charge density profiles in both epitaxial (blue dots) and polycrystalline (red diamonds) CIGS layers calculated from CV measurements at 300 K.

The minimum in space charge density profile has been taken as a value of free hole concentration, resulting in $p=3.5x10^{16}$ cm^{-3} in the case of epitaxial CIGS, about two orders of magnitude larger than in polycrystalline CIGS solar cell ($p=3.9x10^{14}$ cm^{-3}). This large difference can be accounted for by different degrees of electrical compensation in the two systems. While compensation is a well-known feature of Na-free polycrystalline CIGS [36], where a high density of both donor and acceptor defects are simultaneously present, this effect seems to be less prominent in single-crystal CIGS. Since In_{Cu} antisites are known to be the main compensating donors in CIGS, it can be concluded that the density of such substitutional defects in epitaxial CIGS is lower than in poly-CIGS. This hypothesis is in agreement with the

observed annihilation of the emission peak related to $In_{Cu} \rightarrow V_{Cu}$ in the PL spectra of CIGS/Ge samples.

The results obtained during the realization of an epitaxial CIGS layer are very promising. Further developments of this activity include the creations of a photovoltaic cell based on an absorbing layer in monocrystalline CIGS growth on a Ge substrate. The realization of this kind of structure makes it necessary to face several challenges:

1. Studying a way to realize an ohmic back contact on Ge back surface
2. Developing a protection system or using alternative processes to the chemical bath because using the standard deposition technique the Ge back surface is covered by the buffer layer during chemical bath process.
3. The single crystal CIGS is too hard for mechanical scriber then laser scribing is needed.

Chapter 4: Results and discussion – Part 2

In the previous part of this Chapter, it has been shown that a proper optimization of the PED technique leads to highly efficient CIGS-based solar cells.

To summarize, the main achievements were:

1. an efficiency value of 18.75% (on 0.15 cm^2 area), comparable to the best state of the art results It's worthwhile to recall that the world record efficiency is 21.7% on 0.5cm^2 area [20], obtained with much complex and expensive techniques.
2. The process optimization to achieve efficiencies exceeding 16% over 6 cm^2 wide samples, using a single PED source.

These very promising results where the basis of an industrial partnership to scale-up the process and build a pilot line for the CIGS based photovoltaic cell production by PED.

The second part of this Chapter is focused on the solutions of the main issues that might prevent large and homogeneous efficient solar cells:

1. Minimization of droplet density and size onto the CIGS film, causing unwanted shunts on large areas
2. Further increase of the deposition area. The area of 6 cm^2 reported in the previous part of the present Chapter, is the maximum area which can be uniformly coated with a single PED source.

3. Further stability of the electronic beam during long deposition time. With the goal of limiting the PED sources heating, a new type of heater has been designed, realized and tested.

The goal is the deposition on 16x16 cm^2 wide substrates (same as conventional silicon-based solar cells), using a multi-PED system. The numerical modeling and simulations demonstrated its feasibility and the prototype deposition chamber equipped with 4 PED sources has been finally designed and realized, which is now fully operating at the IMEM-CNR "Thin Film Lab" in Parma.

4.6 Control of droplet density and dimensions by substrate bias

As already mentioned in the 2nd Chapter, one of the main feature of the PED is the high energy density of the pulsed electron beam, allowing the complex material ablation, regardless the melting point or the vapor pressure of the single element forming the target.

However, the high energy beam also causes some drawbacks, which are mainly related to the generation of μm-sized particulates and droplets [37 38]. These droplets are expelled from the target surface (hydrodynamic splashing, described in Chapter 2) and, after traveling inside the plasma plume, are finally deposited on the substrate. Since high-performance thin-film solar cells require an extremely smooth surface [39], the density and the size of the particulates produced by high energy pulses techniques must be minimized.

In a similar high energy pulsed technique such as the PLD (Pulsed Lased Deposition), many different technological approaches, like filters [40], off-axis [41] and dual-beam depositions [42] have been attempted in order to minimize the droplet deposition on the substrate. However, because a side effect of these PLD solutions is the reduction of the deposition rate, they are not suitable for large-scale applications.

A more interesting approach, first adopted again in PLD, is the application of a DC bias between the target and the substrate. Lubben et al. have shown that a negative substrate bias can significantly diminish the particle density on the film surface [43]. They observed a five-time decrease in the droplet density on a −150 V biased sample with respect to the unbiased one. The authors explain this phenomenon as the result of a negative charge of the droplets that receive an electrostatic repulsion from a negatively biased substrate.

A similar experimental approach has been applied in this work to the PED process to minimize the presence of particulate on the CIGS surface. Several types of DC voltage were tested, positive and negative in order to understand the phenomenon and study the correlation droplet vs. bias [44].

All films were grown by following the same procedure as described above, with the same number of pulses ($5x10^4$) in order to keep the film thicknesses and the target heating as homogeneous as possible. A customized sample holder has been used to generate a bias field between the substrate and the target. A metallic sample holder allows the contact between the molybdenum-coated substrate and the external DC voltage generator connected to the grounded target through the other pole. Different voltages, V_{ext}, applied to the substrate were studied and the samples were compared to the “benchmark” unbiased sample obtained by electrically insulating the substrate holder. A schematic design of the experimental set-up is shown in Figure 4.21.

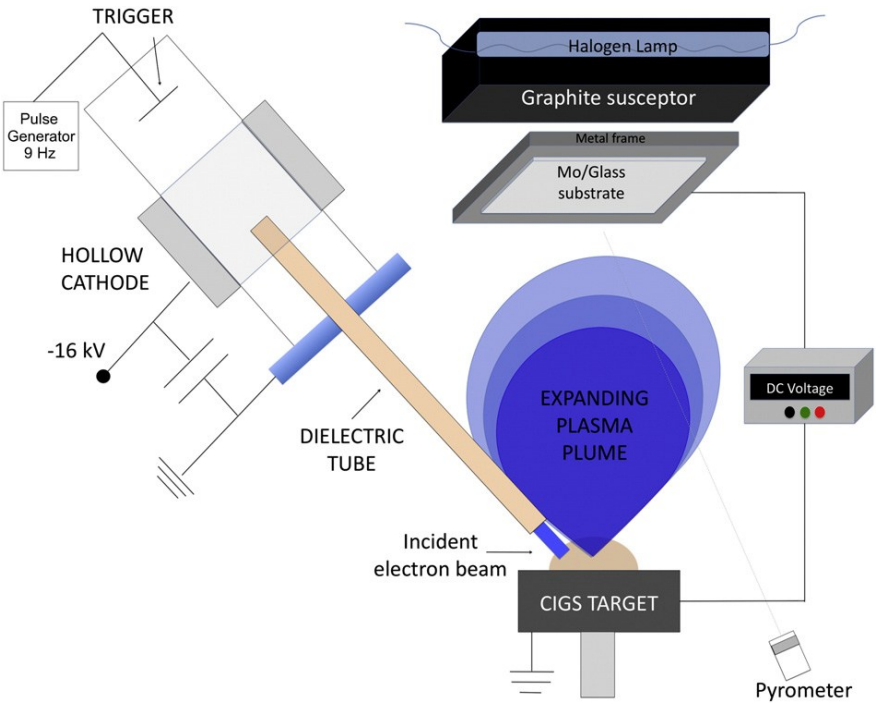

Figure 4.21: Representative scheme of the experimental set-up used to study the bias effect on droplets.

The typical morphology of an unbiased CIGS film grown by PED is shown in the top part of Figure 4.22. The film exhibits a great number of spherical droplets with a radius larger than 0.3 μm and a maximum size of ≈1.2 μm.

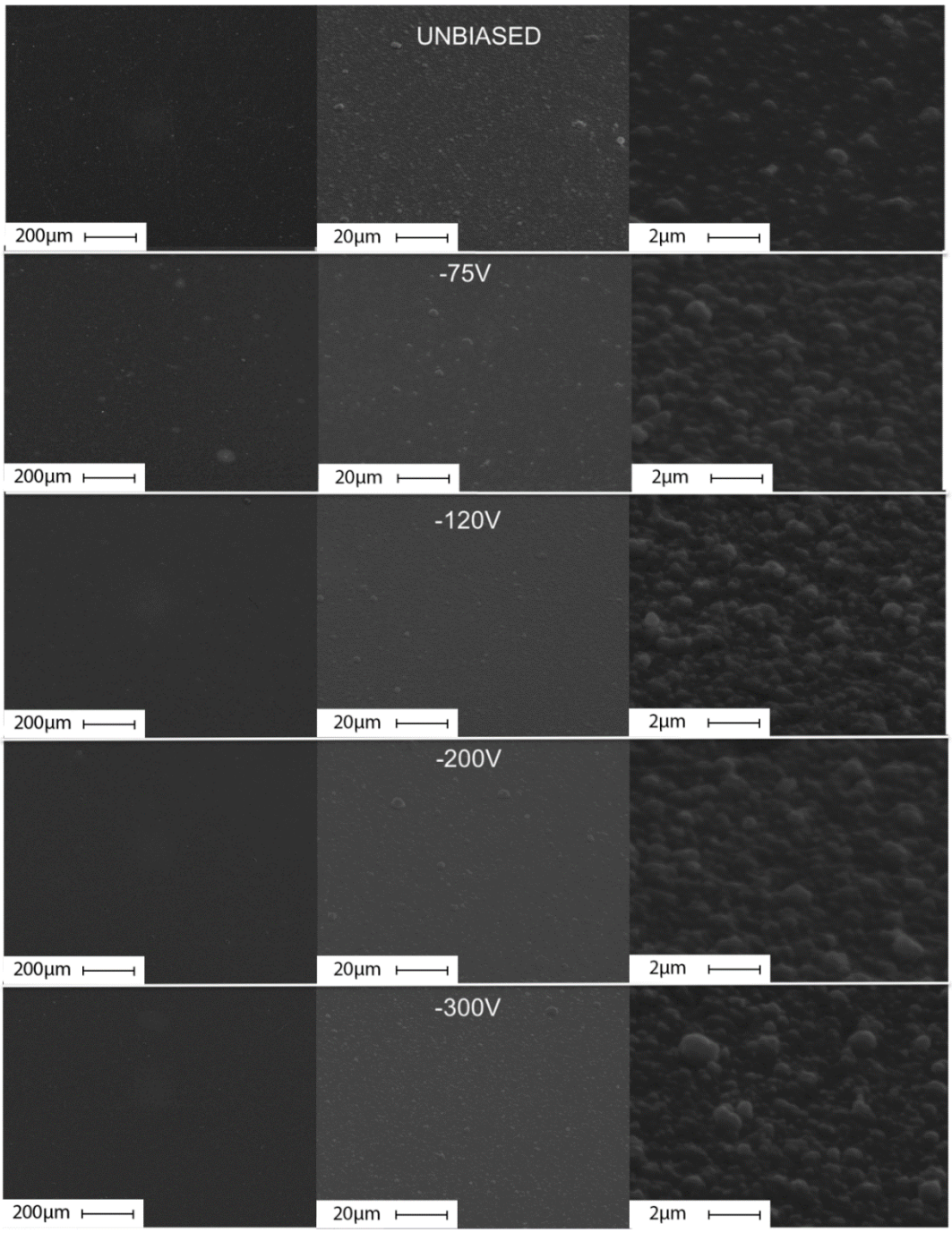

Figure 4.22. SEM images of the surface of CIGS films grown at different negative substrate biases. The pictures were taken at three different magnifications, 100x, 1000x and 10,000x, respectively.

The measured droplet density on the surface is about ≈6x10^5 cm^{-2}, which is a lower value compared to the samples grown by PLD (≈10^6–10^7 cm^{-2} [45 46]). The reduced number of macroparticles obtained by PED is a known feature in the literature and

it is probably due to the polyenergetic nature of the PED e-beam with respect to the laser [47]. Indeed, while in the PED technique the power is mainly transferred on the superficial region of the target, in the case of PLD the absorption profile of a monochromatic light beam leads to a faster heating of the sub-surface, which originates a more intense "splashing" effects [48].

At V_{ext}= −75 V, the film surface exhibits a clear reduction of the biggest droplets with respect to the unbiased sample, as shown in the 100x magnification image in Figure 4.22, with denser concentration of the CIGS grains at 10,000x. A summary of the morphological properties of the CIGS films as a function of the bias is reported in Table 4.9.

Substrate bias V_{ext} [V]	**Droplet density (with radius > 0.5 µm) [cm^{-2}]**	**Maximum droplet radius [µm]**	**RMS surface roughness [nm]**
-300	$5.0x10^4$	0.6	42
-200	$1.0x10^5$	0.8	73
-120	$1.5x10^5$	0.9	75
-75	$3.0x10^5$	1.0	81
Unbiased	$6.0x10^5$	1.2	97
+120	$3.0x10^8$	5.0	18
+200	$1.0x10^8$	7.5	19

Table 4.9: List of morphological properties of CIGS films as a function of the applied substrate bias, V_{ext}: droplet density on the surface, droplet maximum radius and RMS roughness.

By varying V_{ext} from −75 V to −300 V, the droplet density is monotonically reduced from ≈$3x10^5$ cm−2 to ≈$5x10^4$ cm^{-2}. The dilution of the droplets on the CIGS surface becomes evident both in the 100x and the 1000x SEM images. At higher negative V_{ext} the maximum droplet radius of the −300 V biased film is reduced from 1.2 µm (unbiased film) to 0.6 µm.

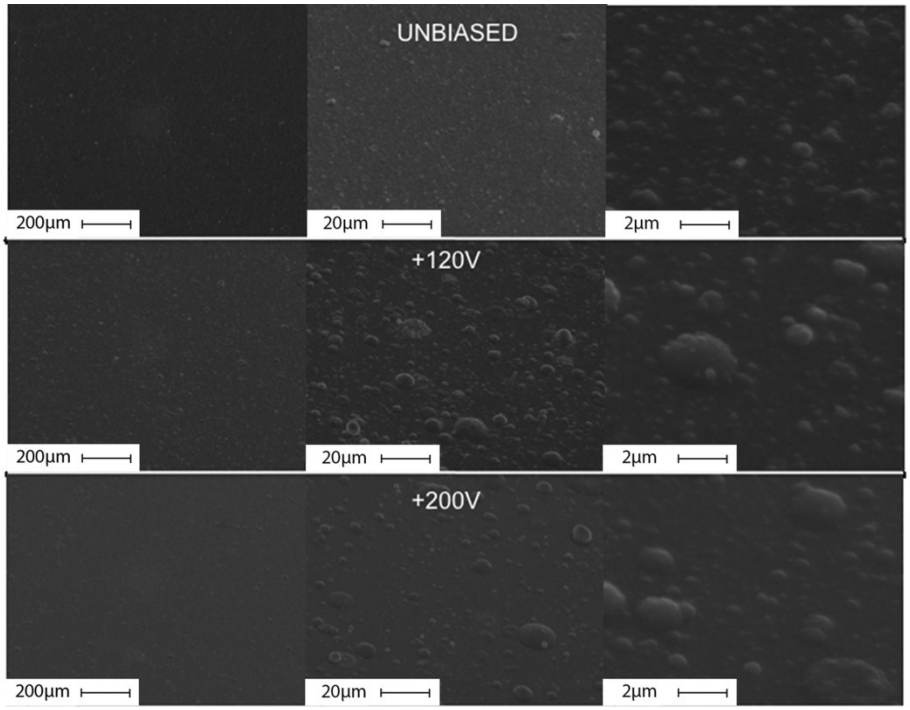

Figure 4.23: SEM images of the surface of CIGS films grown at different positive substrate biases. The pictures were taken at three different magnifications, 100x, 1000x and 10,000x, respectively.

On the other hand, when a positive V_{ext} is applied to the substrate, a significant increase in the quantity of the particulates on the CIGS film can be observed. In Figure 4.23 the surfaces of two CIGS samples grown at different positive V_{ext} (+120 V and +200 V) are compared to the unbiased sample: the droplet density is strongly increased in biased films and their presence becomes detectable even at low magnifications. An enhancement in the droplet density up to $\approx 3\times10^{8}$ cm^{-2} and $\approx 1\times10^{8}$ cm^{-2} is respectively measured in the +120 V and in the +200 V biased film. This is almost three orders of magnitude larger than the average measured in the unbiased case. The maximum radius of the spherical droplets reaches in both cases very high values (5 µm at +120 V and 7.5 µm at +200 V).

Moreover, even the grain morphology seems to be influenced by the bias. Planar SEM images taken at 10,000x (Figure 4.22) reveal an improvement in the grain density and size when the negative voltage is increased. While in the unbiased case

isolated and dispersed grains are clearly visible on the surface, at V_{ext}=−300 V densely packed grains, with an average size up to 1 μm, cover the surface completely. On the other hand, only small grain islands, with a size smaller than 100 nm, are visible on the surface of positively-biased substrates. AFM (Atomic Force Microscopy) analysis confirms the variation in the grain density as a function of the external bias, as shown in Figure 4.24.

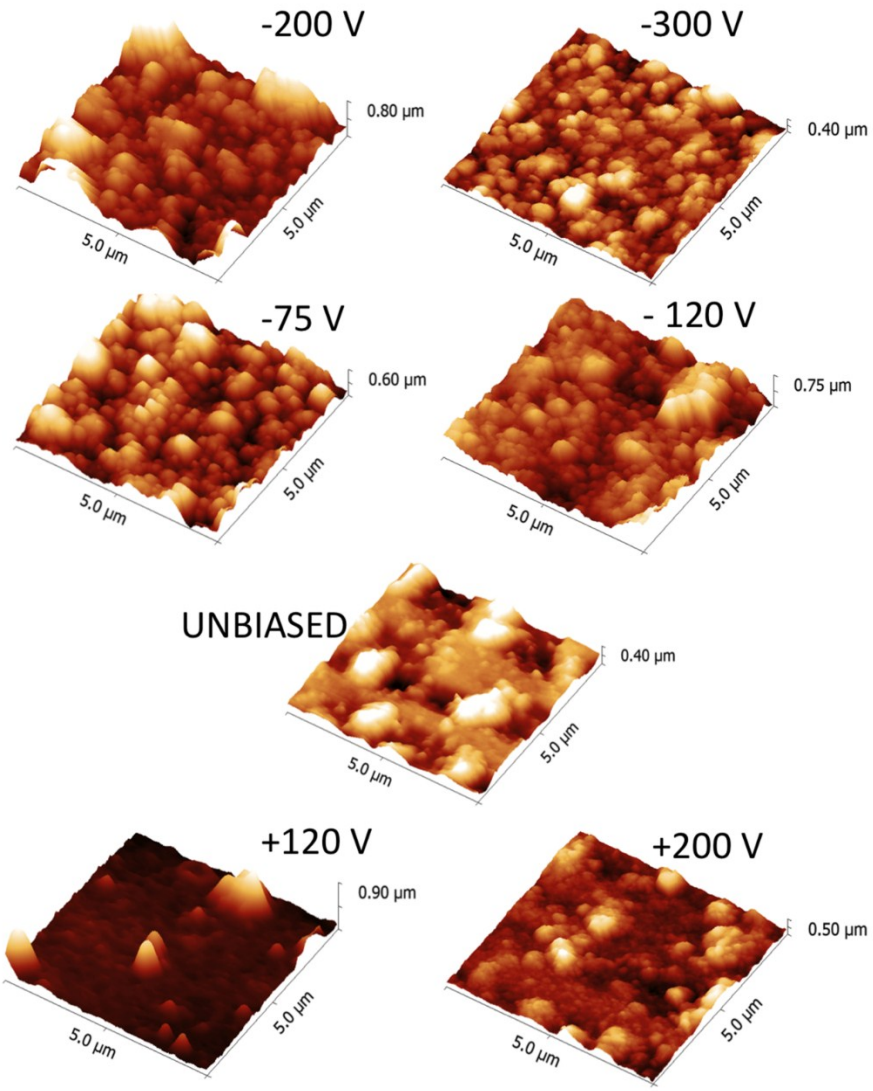

Figure 4.24: Atomic force microscopy images of the surface of CIGS films grown at different V_{ext}. The scanned area is 5 × 5 μm^2.

Figure 4.24 illustrates AFM maps of 5x5 μm^2 surface areas of the CIGS films grown at different V_{ext}. The evaluated root mean square (RMS) CIGS surface roughness is reported in Table 4.9. When compared to the unbiased sample (RMS = 97 nm), the negatively-biased layers exhibit a smoother surface as the voltage increases, with a RMS roughness reaching a value of 42 nm at −300 V. This is probably due to the denser grain distribution also observed in the SEM images. The surface looks very different in the case of positive biases: the samples grown at $V_{ext} \geq +120$ V exhibit a roughness drop to ≈20 nm. This very a low RMS value can be explained by the large presence of embedded spherical droplets. Since these particles exhibit a negligible roughness (due to their native liquid nature), the film morphology is greatly influenced by their presence when positive biases enhance their density (>10^8 cm^{-2}) and size (>5 μm).

The results obtained, show that the application of a negative bias between the target and the substrate is an efficient and elegant method to minimize the droplets density and size. This is an innovative and important development for the CIGS growth by PED for photovoltaic applications and noticeable, an easily scalable process for industrial solar cell production.

4.7 PED dynamics of evaporation

The industrial development of a deposition technique requires a perfect knowledge of the phenomenon on a laboratory. It's therefore essential to understand in detail the evaporation dynamics of the PED technique in order to design a system able to reproduce high quality deposition on larger scale.

Specifically, all the PED parameters affecting the CIGS layer thickness and compositional uniformity were tested, aiming to find the maximum deposition area obtainable with a single PED source.

The PED evaporation dynamics of the material was studied to better understand the origin of compositional variations along the CIGS layer and how to mitigate this phenomenon by adjusting the setup of the electronic source [49].

For this study a target of CGS ($CuGaSe_2$) was used, because its high band gap which enabled to measure the film thickness by optical interference. The thickness was calculated by measuring maxima and minima positions of the interference fringes in the reflectivity spectra acquired by an IR-VIS spectrophotometer (JASCO V-530) in the range between 750 and 1100 nm, where CGS is optically transparent.

The electrons acceleration voltage was varied in the range 10-18 kV to understand how the dynamics of evaporation is affected by the electron beam energy. The substrates used were soda-lime glass of 75 x 25 mm^2, area. After the deposition, the samples were divided in a grid of 15 × 5 squares with an area of 0.25 cm^2 each (75 squares every CGS samples!) as shown in Figure 4.25, to locally probe the chemical composition and the thickness in each square, reported in Table 4.10 as a function of the acceleration voltage (V_{PED}).

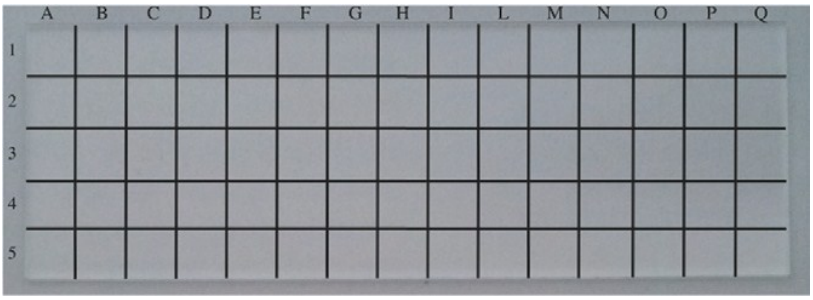

Figure 4.25: A 75×25mm^2 SLG sample divided in to a grid of 15×5 squares of 0.25 cm2 area: the chemical composition and the thickness were measured for each square.

V_{PED} (kV)	at% [Cu]	at% [Ga]	at% [Se]	[Cu]/[Se] ratio
10	13.7	31.8	54.5	0.43
12	20.0	27.3	52.7	0.73
14	21.7	25.9	52.4	0.84
16	23.2	25.5	51.3	0.91
18	23.6	25.4	51.0	0.93

Table 4.10: Compositional data of CGS films obtained by EDS analysis

The Cu content in the film increases from 13.7% at 10 kV to 23.6% at 18 kV, with an abrupt increment between 10 and 12 kV (20.0%). The Cu/Ga ratio is asymptotically drifted to 1 by raising V_{PED}, from 0.43 at 10 kV to 0.93 at 18 kV.

In Figure 4.26 the XRD patterns collected in the central square of every CGS film deposited at different V_{PED} are compared.

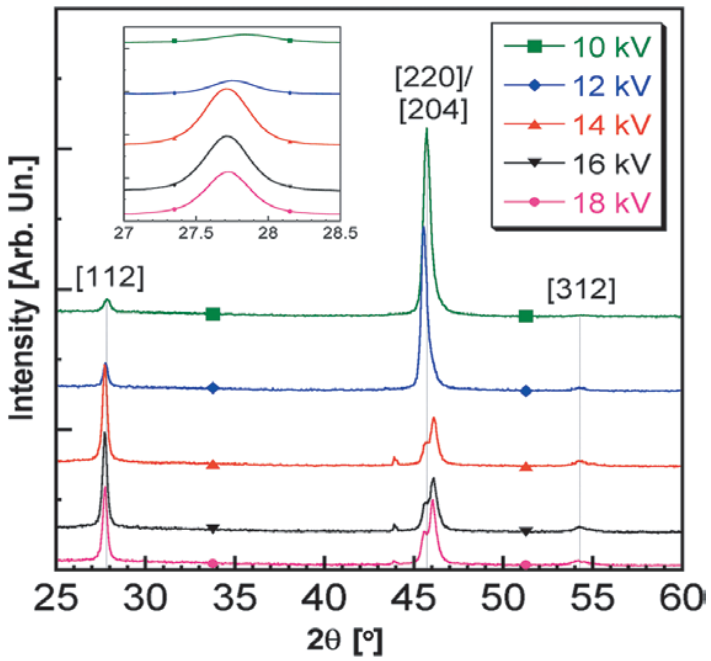

Figure 4.26: *θ/2θ* XRD patterns of CIGS/SLG films grown at different acceleration voltages (V_{PED}). The inset shows the (1 1 2) peak position at various V_{PED}.

The single tetragonal chalcopyrite phase is present on all the samples, with a preferred crystal orientation switching from the (204)/(220) to the (112) direction by increasing the discharge voltage. The chalcopyrite structure is preserved also at low V_{PED}, despite the strong Cu-deficiency: this Cu-poor CGS phase, called *ordered vacancy compound* (OVC) with chemical formula $CuGa_3Se_5$, shows the same tetragonal structure as the stoichiometric CGS. In the OVC phase (that is obviously an unwanted composition, being a n-type semiconductor) the vacant Cu site are compensated by an ordered array of point defects (Cu vacancies and substitutional Ga) [50].

The most significant change in the XRD spectra regards the position of the reflection peaks. As seen in the inset of Figure 4.26, the CGS peaks shift to higher 2θ values by lowering the acceleration voltage. The lattice parameter, *c*, calculated for a tetragonal chalcopyrite structure, exhibits a monotonic increase with V_{PED} (from 10.90Å at 10 kV to 11.09Å at 18 kV). As can be observed from figure 4.27, the experimental values of *c* axis are comprised between those of stoichiometric $CuGaSe_2$ phase (11.09Å [51]) and $CuGa_3Se_5$ (10.89Å [52]), which is the most stable ordered Cu-vacancy compound; a good agreement between the trend of lattice parameters and that of Cu/Ga content ratio as a function of V_{PED} is also shown.

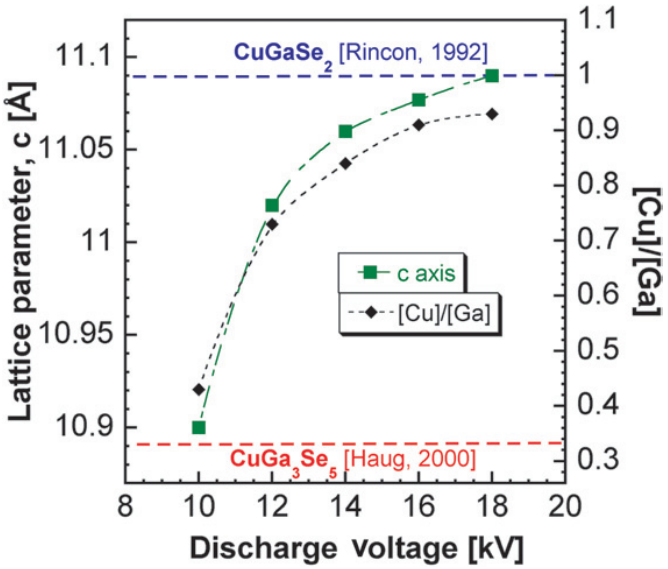

Figure 4.27: Lattice parameter, *c*, and Cu/Ga ratio of CGS films as a function of V_{PED}.

By hypothesizing that the sticking coefficient of the high energy ablated species reaching the substrate assumes the value of the unity and that no re-evaporation from the film surface is expected at 300 °C, it is possible to affirm that CGS films inherit the same chemical composition as the evaporating plume, hence the elemental content of the plume can be deduced by directly analyzing the EDS data on the films. From these measurements it is possible to conclude that a perfect stoichiometric transfer from the starting target to the deposited film never occurs for any V_{PED} values comprised between 10 and 18 kV, that implies an imperfect

compositional transfer mechanism during the solid-to-vapour transition from the target to the plume. By analyzing the compositional data of CGS reported in Table 4.10, the relative content of the different species present on the film (and, thus inside the plume), can be expressed by a simplified chemical formula given by the linear combination of two phases, as follows:

$$CuGa_3Se_5 + M(CuGaSe_2)$$

with the number of moles of the stoichiometric phase, *M*, dependent on the acceleration voltage. The variation of the plume composition as a function of V_{PED} is reported in Table 4.11.

V_{PED} (kV)	Chemical Formula	$CuGaSe_2$ moles, M	$CuGa_3Se_5$ mole fraction (X_{ovc})
10	$CuGa_3Se_5$ + ½ $CuGaSe_2$	½	0.67
12	$CuGa_3Se_5$ + 4 $CuGaSe_2$	4	0.20
14	$CuGa_3Se_5$ + 8 $CuGaSe_2$	8	0.11
16	$CuGa_3Se_5$ + 14 $CuGaSe_2$	14	0.07
18	$CuGa_3Se_5$ + 21 $CuGaSe_2$	21	0.05

Table 4.11: Chemical formula and mole fractions of PED plume at different V_{PED} values, derived from EDS analysis.

At V_{PED} = 10 kV the amount of the OVC phase in the plume dominates, resulting in the crystallization of a compound very similar to $CuGa_3Se_5$, as it appears from the *c*-axis value extrapolated by XRD patterns. Above 12 kV the $CuGaSe_2$ contribution to the plume composition starts to prevail (*M* = 4), and the OVC mole fraction, X_{OVC}, (calculated from the number of moles of $CuGa_3Se_5$ divided by the total moles in the plume) becomes negligible when V_{PED} exceeds 16 kV (*M* = 14). It is then possible to conclude that a good stoichiometric transfer from the target to the plume can be achieved by increasing the energy of the impinging electrons, proportional to the acceleration voltage.

As far as the thickness uniformity, by collecting the measurements of every 0.25 cm^2-large CGS square samples illustrated in Figure 4.25, the whole thickness map on the substrate was rebuilt. A 2D map of the normalized thickness of CGS films grown at 10 kV on a 75×25mm^2-large substrate is given in Figure 4.28.

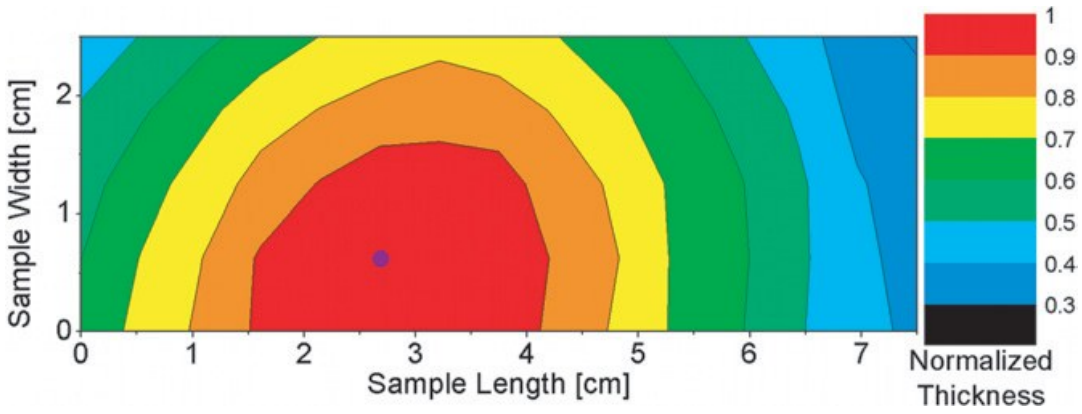

Figure 4.28: 2D map of the thickness of CGS films grown at V_{PED} = 10 kV. The thickness values are normalized with respect to the maximum value indicated by the purple circle.

The thickness experimental data can be plotted as a function of the angle θ formed by the target normal and the line joining the target to the analyzed substrate point. Since $\theta = \arctan(x/d)$, where d is the target–substrate distance and x is the distance between the measured point and the target normal, it is possible to calculate the angular thin-film thickness profile, $t(\theta)$ with respect to the maximum thickness, $t(0)$ = 1500 nm. A comparison between the thickness profiles of CGS, obtained at V_{PED} = 10 kV and 18 kV, respectively, is shown in Figure 4.29.

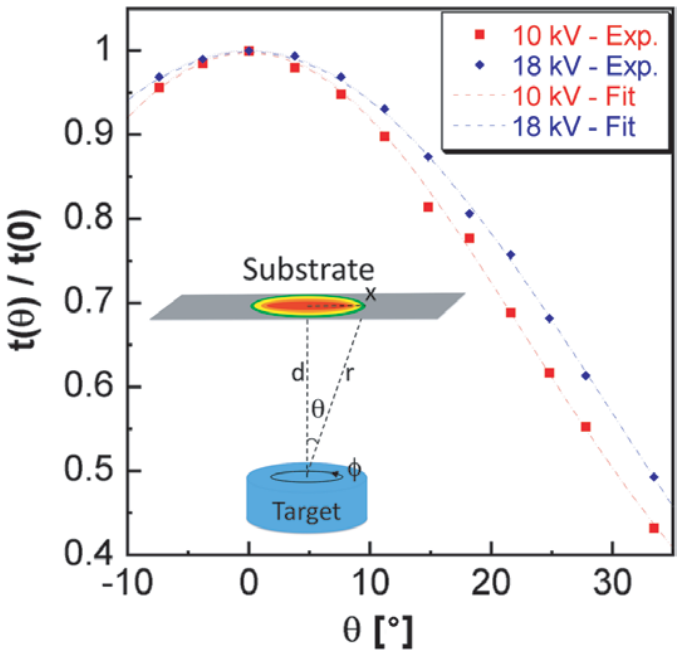

Figure 4.29: Thicknesses profiles (normalized to each maximum) for the CGS films grown with V_{PED} = 10 kV and 18 kV, respectively. The dashed lines are the calculated fitting curves using the bicosine model described below.

The experimental data were fitted with the angular distribution model, introduced by Comsa and David [53], which well applies to several experimental works about PLD [54 55 56]. In this model the angular distribution over the hemispherical space described by θ and φ, which is the rotation angle around the normal to the target surface (inset in Figure 4.29), is described by a function $F(\theta,\varphi)$, actually independent from φ, due to the circular symmetric nature of the evaporation. This function is composed by a linear combination of two cosine terms:

$$F(\theta,\varphi) = F(\theta) = a\ \cos\theta + (1-a)\ cos^{p}\ \theta$$

The first component of the function, weighted by the coefficient *a*, gives a broader distribution, with respect to the forward-peaked second component exhibiting an exponent $p > 1$. Integrating the above bicosine equation over hemispherical space, the contribution fraction of the first cosine term, *f*, to the evaporation dynamics can be found as in [56]:

$$f = \frac{(pa + a)}{(pa - a + 2)}$$

a and *p* are adjustable parameters to yield the best agreement with the experimental data, taking into account the $\cos^3 \theta$ correction term for the planar geometry of the substrate [54]. The angular distribution functions that give the most satisfactory fitting at each value of V_{PED} are listed in Table 4.12.

V_{PED} (kV)	a value	p value	R^2 (bicosine model)	Contribution fraction of cos θ term, f
10	0.31	0.69	0.9963	0.656
12	0.07	0.93	0.9932	0.201
14	0.05	0.95	0.9974	0.120
16	0.03	0.97	0.9953	0.069
18	0.02	0.98	0.9936	0.049

Table 4.12: Thickness distribution model of CGS as a function of PED voltages, according to bicosine models

The goodness of the fit, measured by the coefficient of determination, R^2, together with the *f* value calculated at each V_{PED} are also reported. As it appears from the *f* coefficients, the contribution of the cos *θ* term to the distribution profile is very significant at 10 kV (0.656), while it becomes smaller at higher V_{PED} and almost negligible above 16 kV. At $V_{PED} \geq 14$ kV the angular distribution can be assumed to be driven only by the second term, with the exponent p asymptotically tending to a constant value ≈4:

$$F(\theta) \approx cos^4\theta$$

Therefore, in this V_{PED} range the plume distribution can be regarded as independent of the acceleration voltage.

By comparing the $CuGa_3Se_5$ mole fraction values, X_{OVC}, in Table 4.11 and those of *f* factors in Table 4.12, a perfect agreement can be found. The former represents the mass contribution of the OVC phase to the whole plume composition, whereas

the latter is the ratio of the plume mass evaporating according to the cos θ distribution over the total evaporated mass. Since they reproduce, the fraction of plasma plume having a $CuGa_3Se_5$-related composition and the one expanding from the target with a broad angular distribution, respectively, is possible to assert that the part of the plume exhibiting the OVC phase spreads from the target according to a cos θ distribution, which is the typical distribution due to the evaporation occurring at the thermodynamic equilibrium. In contrast, the expansion of the stoichiometric $CuGaSe_2$ fraction of the plume follows a forward-peaked $\cos^p \theta$ trend, typical of an ablative mechanism. The thermodynamic evaporation of $CuGa_3Se_5$ is in agreement with the $Cu_2Se–Ga_2Se_3$ pseudo-binary phase diagram, which evidences that an incongruent transition is developed during the $CuGaSe_2$ melting, leading to the formation of a Cu-poor liquid phase with respect to the solid.

The study of the evaporation dynamics has allowed the depth understanding of the ablation phenomenon and how it has an impact on the composition and uniformity of grown film. The data obtained are the basis for the development of a technology that can increase the area of deposition. This technology is crucial to expand the PED technique to industrial applications. In the next section will be describe, through the study of the ablated material distribution, how a simulation model that combines the effects of different PED sources have been created with the aim of increasing the deposition area.

4.8 Industrial Scale up

The activities to design and to build a new apparatus equipped with a multi-source array of PED guns in order to produce wide photovoltaic cells (16x16 cm^2) is reported in this paragraph. As already mentioned in the previous paragraph, the deposition area of a single PED source is not suitable for large area solar cells realization, for its limited “deposition cone”. As presented in Figure 4.13 and Table 4.8, “large-area” CIGS-based solar cell grown by PED with high quality and high uniformity of performance (η=16%) over a total area as large as 6 cm^2 have been

reproducibly obtained; this is the limit achievable with a single PED source and with the static deposition.

In order to further enlarge the deposited are, 3 solutions can be adopted: i) increasing the target-substrate or ii) moving the substrate or iii) developing a multi-PED system; we followed the latter, for the possibility to keep a high deposition rate. Indeed, increasing the target-substrate distance causes a deposition rate decreasing proportional to the square of the distance; the same effect results by moving the substrate, making these kinds of approach unacceptable in the industrial perspective.

The increase the deposition area keeping a high degree of thickness uniformity by using different PED sources is a challenging task. Exploiting the results obtained on the ablation/evaporation study, a software simulating the dynamics of PED plume has been developed. The simulation program [57] was written in the Matlab code, using the bicosine equation to include both contributions (evaporative and ablative) and to calculate the film thickness distribution pattern on the substrate [49].

$$F(\theta,\varphi) = F(\theta) = a\ \cos\theta + (1-a)\ cos^p\ \theta$$

The starting point has been the simulation of the CIGS layer uniformity from a single PED source. As expected and experimentally verified, the CIGS film grown by a single PED source (accelerating voltage = 16 kV) The simulated data are in excellent agreement with the experimental results obtained on 6 cm^2 wide area cells, showing a significant thickness drop at the rim of the substrate holder (Figure 4.30).

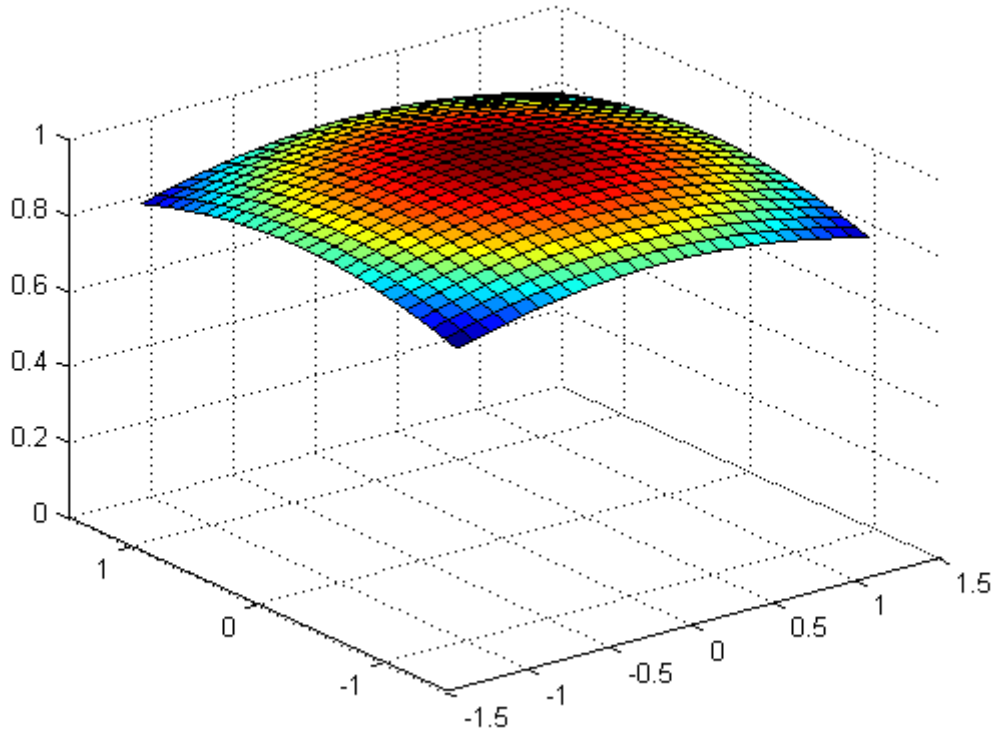

Figure 4.30: CIGS thickness profile on 6 cm^2 wide area obtained by simulating a single source PED deposition.

The simulation is essential to find out the optimal number of sources necessary to uniformly coat a 16x16 cm^2 (256 cm^2) commercial substrate in a multi-PED system. In Figure 4.31 the result of the expected CIGS film uniformly on a 16x16 cm^2 substrate with an area of 256 cm^2 (left side) using 4 different sources in a square, static configuration (right), which is the minimum number to realize CIGS-based solar cells with the desired area and within reasonable time.

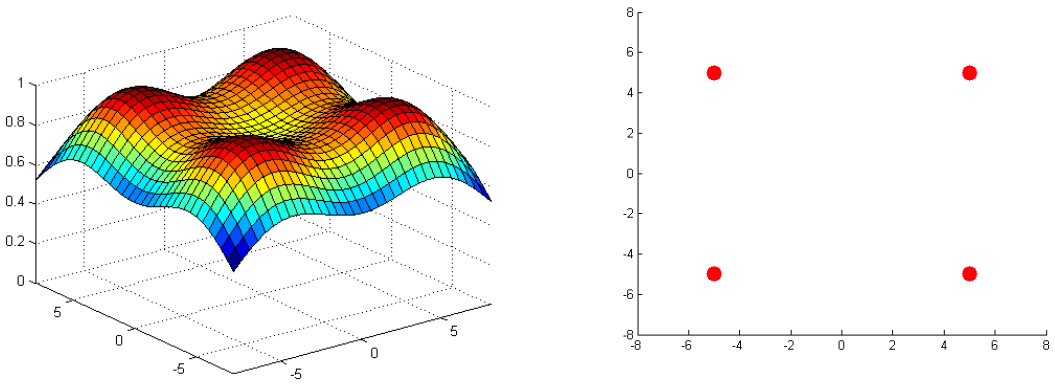

Figure 4.31: CIGS thickness profile on 256 cm^2 wide area obtained by simulated 4-source PED deposition (left). Target configuration under the substrate used to generate the CIGS profile (right).

In the simulations, different parameters aspects of industrial interest have been taken into account:

1. Standard deviation: it allows to evaluate the thickness variations occurring during the deposition
2. Minimum thickness: it allows to evaluate position of the thinnest areas of the layer. A thickness too small is not sufficient for an optimal device operation.
3. Coating yield: it allows to evaluate the relationship between the evaporated material deposited on the cell area, respect to the total amount of the evaporated material. It is a measure of the material waste.
4. Production time: it is the time required to realize a 16x16 cm^2 cell. In the simulation used to calculate this parameter, 4 PED sources operating at 100 Hz were considered. The repetition rate of 100 Hz was chosen as a good compromise between the industrial need of speed production and process reliability. In fact, in order to satisfy the demanding requirements of the industrial partners involved in the PED4PV project, pulsed sources with higher repetition rate compared to the ones currently used in the laboratory, are needed.

To maximize the different parameters two different alternatives were explored:

1. Increasing the number of sources. In this way it is possible to maximize the uniformity and increase the production speed of the devices but this involves a greater investment in electronic sources. A 6 sources deposition (Figure 4.32) was simulated to increase the uniformity compared to the previous case based on 4 sources.

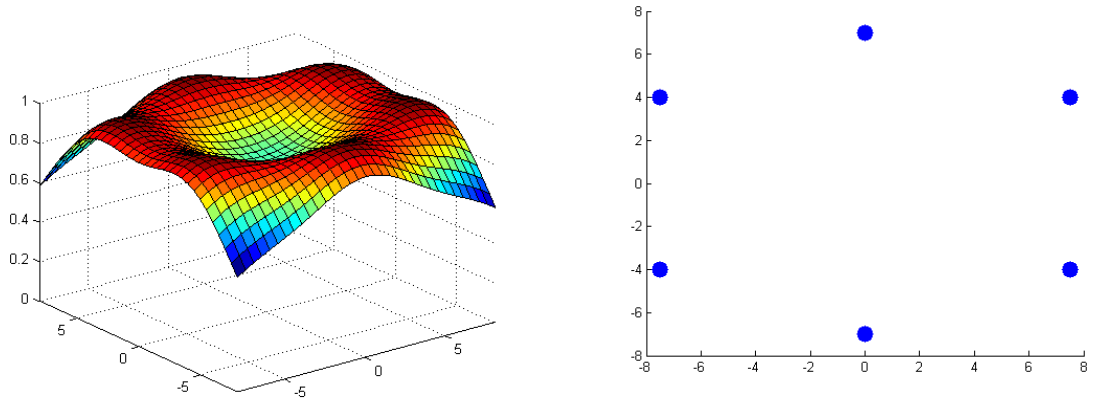

Figure 4.32: CIGS thickness profile on 256 cm^2 wide area obtained by simulating a 6-source PED deposition (left). Target configuration under the substrate used to generate the CIGS profile (right).

2. Substrate motion. The substrate movement can increase the uniformity on larger area. At the same time it allows to increase the production speed and minimize the material waste. In Figure 4.33 is represented a simulation in which a linear motion was introduced.

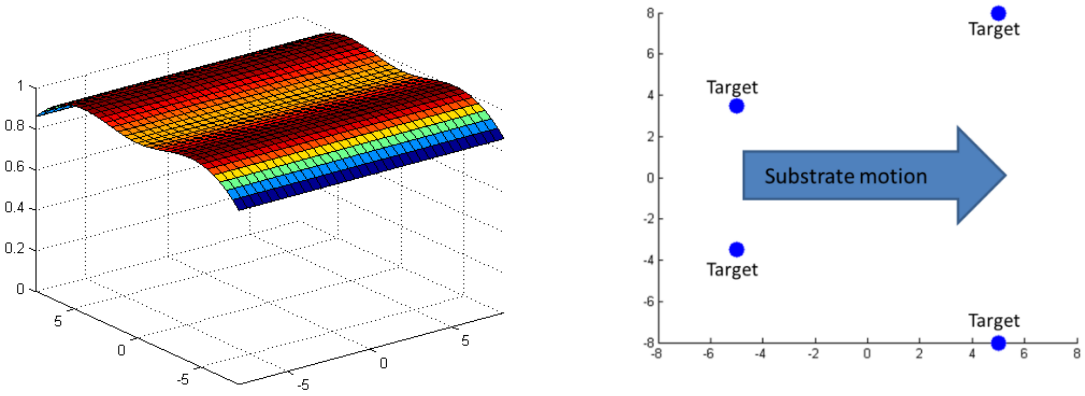

Figure 4.33: CIGS thickness profile on 256 cm^2 wide area obtained by simulating a 4-source PED deposition with the addition of linear motion (left). Target configuration under the substrate used to generate the CIGS profile, the arrow indicates the direction of the substrate motion (right).

The simulations allows to explore more complex substrate movements, to look for higher film quality, as shown in Figures 4.34 (4 PED sources, rotational movement) and 4.35 (4 PED sources, linear + rotational movement). A summary of the most relevant figures are reported in Table 4.13.

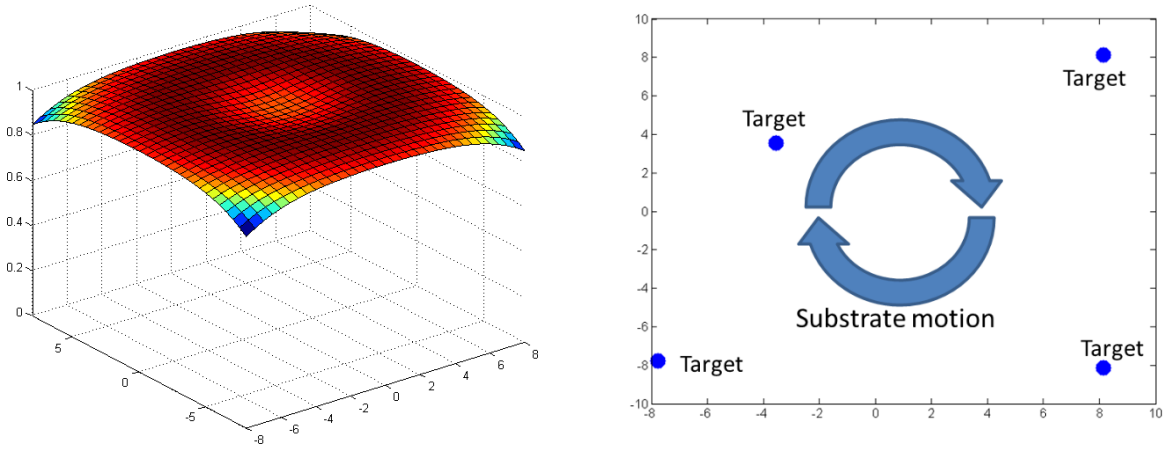

Figure 4.34: CIGS thickness profile on 256 cm^2 wide area obtained by simulating a 4-source PED deposition with the addition of a rotational movement (left). Target configuration under the substrate used to generate the CIGS profile, the arrow indicates the direction of the substrate motion (right).

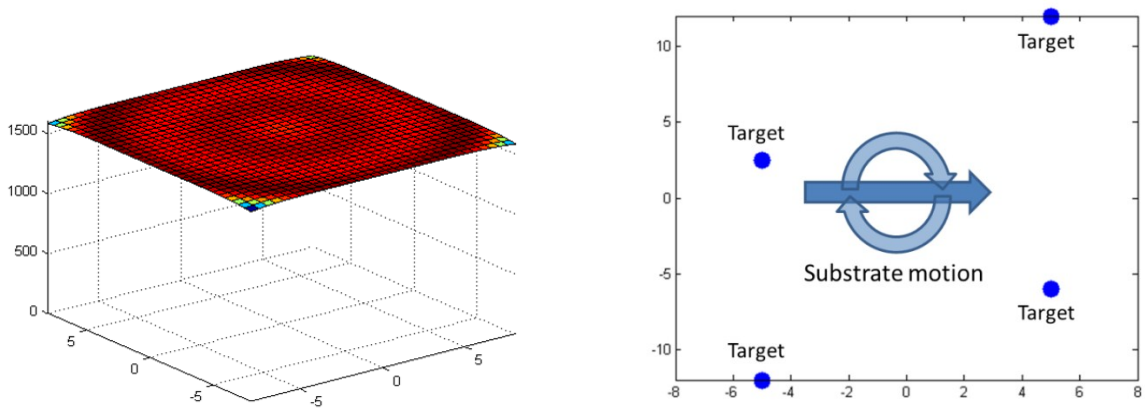

Figure 4.35: CIGS thickness profile on 256 cm^2 wide area obtained by simulating a 4-source PED deposition. Both linear and rotational motion were applied. (left). Target configuration under the substrate used to generate the CIGS profile, the arrow indicates the direction of the substrate motion (right).

Substrate motion	Uniformity (%)	Coating yield (%)	Deposition Time (s)
Static	83	54	81
Linear	96	46	50
Linear-rotational	99.8	30	110

Table 4.13: Comparison between different type of motion used in multi-PED (4 source) system simulation.

Increasing the complexity of the substrate movements it is possible to further increase the film uniformity. However the increase of uniformity causes a dilation of the time required to achieve the layer of CIGS.

The multi-PED has finally been compared to the deposition technique most used in the industrial processes [58]: the thermal co-evaporation. The data shown in Table 4.14, concerning the thermal co-evaporation, refer to a process simulated by using the developed software.

Technique	Uniformity (%)	Std. Dev. (%)	Coating yield (%)	Deposition time (s)
Thermal co-evaporation (STANDARD)	96	3.0	22.0	130
Multi-source PED (high speed)	96	2.8	46	50
Multi-source PED (high quality)	99.8	0.2	30.2	110

Table 4.14: Comparison between thermal co-evaporation (industrial standard technique) and multi-source PED technique (simulation)

The data in Table 4.14 demonstrate the versatility of the PED multi-source in comparison with the co-thermal evaporation. The linear motion (Multi-Source PED - Speed) permits to reduce the waste material and the time taken to perform a CIGS film on a surface of 16x16 cm^2 more than 50%; this is in accordance with the time required by the industrial partners of the project PED4PV. Instead using a linear-rotation (Multi-Source PED - High Quality) it is possible to increase the uniformity compared to co-thermal evaporation, keeping production times like this.

4.8.1 Multi-PED system realization

Using the simulation results, a first multi-PED prototype has been realized, to deposit on a 75x25 mm^2 (≈18 cm^2) glass/Mo substrate using 2 PED sources [57]. The Figure 4.36 shows the simulation of thickness uniformity in this system.

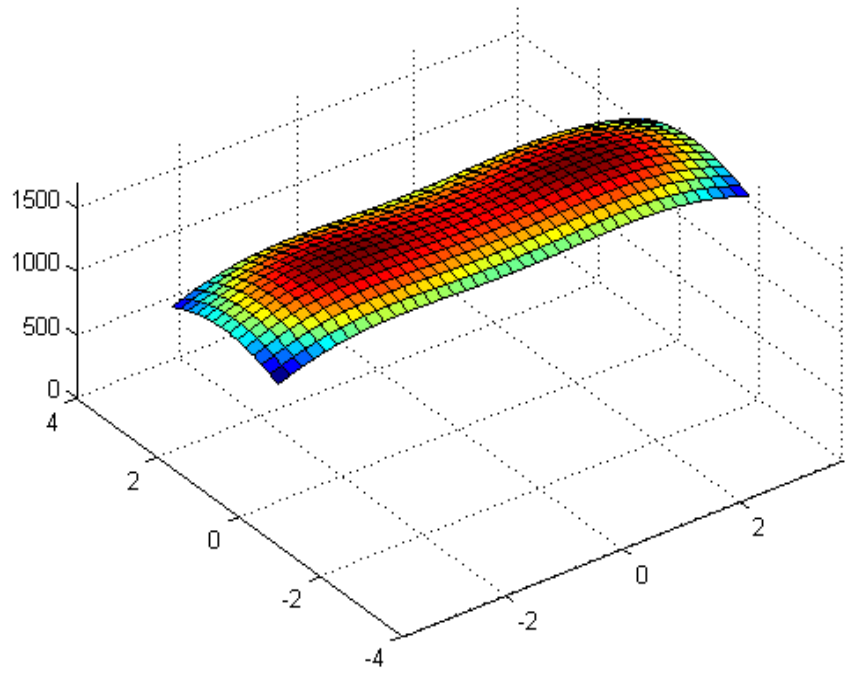

Figure 4.36: CIGS thickness profile on 18 cm^2 wide area (75x25 mm^2) obtained by simulated 2-source PED deposition.

In Figure 4.37 the double-PED system in operation is shown; one may notice that every PED source has its own CIGS target.

Figure 4.37: Double-PED system in operation

The final device has been finally completed, to test the effectiveness of the new deposition process. After the standard CIGS deposition, according to the parameters described in the previous paragraphs, the cell was completed by depositing In_2S_3 buffer layer (an interesting alternative, cadmium free, buffer layer) in collaboration with Helmholtz-Zentrum Berlin (HZB), by ILGAR (Ion Layer Gas Reaction) method [59]. The cell was terminated by a bi-layer TCO (Transparent and Conductive Oxide), formed by UZO (undoped ZnO) and AZO (2% Al doped ZnO) both grown by RF-sputtering; the final architecture was: AZO/UZO/In_2S_3/CIGS/Mo/Glass.

The rectangular substrate was divided into 3 1x1” samples (Figure 4.38); the J-V characteristics data of three different solar cells confirm a good uniformity (Table 4.15). It must be recalled that, rather than the efficiency, this activity was more focused on the search for the performance uniformity on area larger than 1”x1”; the efficiency around 10% on squared inches CIGS-based solar cells with unconventional, Cd-free buffer layer is however an important results.

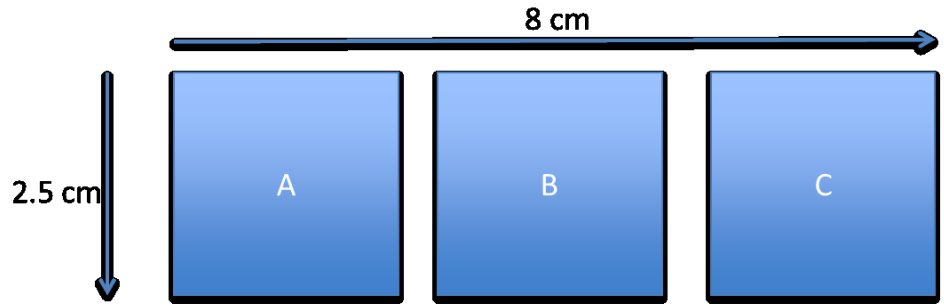

Figure 4.38: Schematic representation of solar cell partition.

	A	B	C
Voc (mV)	608	598	603
Jsc (mA/cm^2)	27	28.1	28
Fill Factor (%)	62	62	57
Efficiency (%)	10.18	10.42	9.62

Table 4.15: Photovoltaic parameters of the cells represented in Figure 4.38

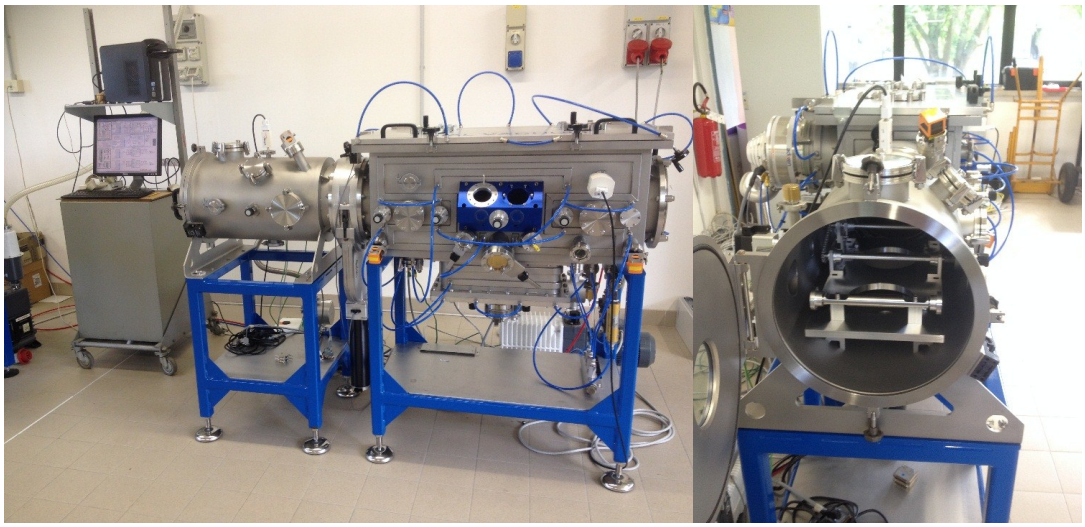

Figure 4.39: Pre-industrial Multi-PED system installed at IMEM-CNR

Thanks to the know-how acquired on the by the PED process and the promising results achieved on larger area, with the support of the industrial partners involved in the “PED4PV” project we have finally been able to design, realize a prototype of a multi-PED deposition chamber (Figure 4.39) with the aim to deposit CIGS-based solar cells on 16x16 cm^2 large substrates (same as Silicon-based cells). The multi-PED system, recently installed at IMEM-CNR in Parma has been successfully tested and the first large area cells are already available (Figure 4.40) , although not yet fully characterized and optimized.

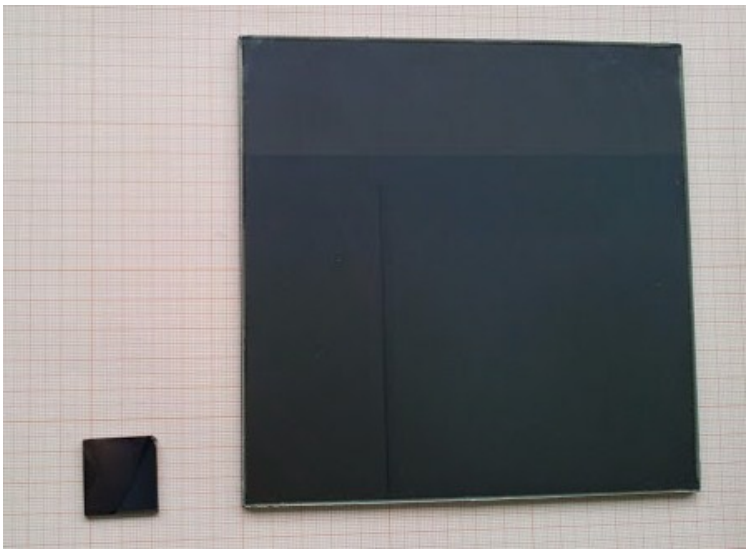

Figure 4.40: Comparison between a CIGS film deposited in the lab-scale PED system on a 2.5x2.5cm^2-wide glass (left), and a sample grown on a substrate area of 16x16cm^2 using the pre-industrial multi-PED system (right).

The prototype multi-PED system present several innovations:

1. 4 optimized PED source, specifically realized to increase the pulse frequency (and thus the deposition rate)
2. The chamber is equipped with a linear motion system to maximize the solar cells uniformity.
3. The low temperature deposition temperature, characteristic of the PED technique, enables the deposition on unconventional substrates, such as ceramic (ideal for Building Integrated PhotoVoltaic, BIPV) and/or thermolabile, flexible materials (i.e. polymers, metal foils, etc)
4. Last, but not least, I would like to emphasize the financial support of private investors and companies, in a difficult economic scenario and in a tough field such as the photovoltaic renewable energy, making possible a (rare) example of fundamental research that moves towards (pre-)industrial applications.

4.9 CIGS growth on Joule heated substrate

In view of a possible PED industrial scale-up of the PED process, one of the most important requirements is the reduction of the deposition time; the solar cell production must be rapid and continuous. PED is a fast process (<15 min to deposit 1.5 um of CIGS at 10 Hz) and suitable for low temperatures deposition, but over time the heaters tend to heat the gun. A continuous heating by a massive sample-heater, such as the conventional IR lamp-based device, can therefore cause two different drawbacks:

1. the target overheating leads to an increase of the melted surface of the material causing formation of droplets of the film surface [44].
2. the electronic source losses of efficiency due to the overheating with. Indeed, when the PED source overheats the discharge time is extended, decreasing the power of the single pulse and the ablation efficiency. [60] As a secondary consequence of this phenomenon there is a further heating of the target due to the less energetic electrons, the ones unable to ablate CIGS, aggravating the situation described in point 1.

In order to minimize the PED sources overheating, during this work, an unconventional heater was studied, realized and tested, instead of the normally used method implying IR lamps and graphite susceptors. It is based on the Joule effect, forcing the current to pass through the metal back contact (Molybdenum) of the metalized substrate [61]. Due to the resistance of the thin metal layer (typically, the Mo thickness is about 0.5 μm) deposited on the substrate, the flowing electrical power is efficiently transformed into heat: the heating is localized and only few Watt are required to increase the temperature of a 25x25mm^2 wide substrate surface up to ≈300°C; the very low emissivity of the metal layer leads to a negligible heat irradiation towards the e-beam source, the target and the walls of the vacuum chamber, thus minimizing heat-induced instabilities effects during the target ablation process. In addition, this type of heating through a constant current flow allows a good temperature uniformity of the substrate as well as the larger conventional heater [57].

The effectiveness of joule heating system has been studied by comparing a standard solar cell (conventional IR-graphite heater, used to fabricate the 15% cell efficient described in Chapter 3) with a Joule heated solar cell. Since the goal is the comparison of the hearing systems rather than the cell performance, the cells architecture used were as simple as possible (Glass/Mo/NaF/CIGS/CdS/ZnO;Al, without i-ZnO layer on top). A 25x25mm^2 wide Mo coated-glass substrate was mounted on a customized holder made by two parallel Cu rods, shown in Figure 4.41. These rods were connected to a 0-10V DC voltage generator. By using this configuration, the generated DC current was forced to flow across the Mo film, heating only the area where the CIGS will be grow. The Mo thickness was 500 nm, with a resistivity value of 1x10^{-6} Ωcm.

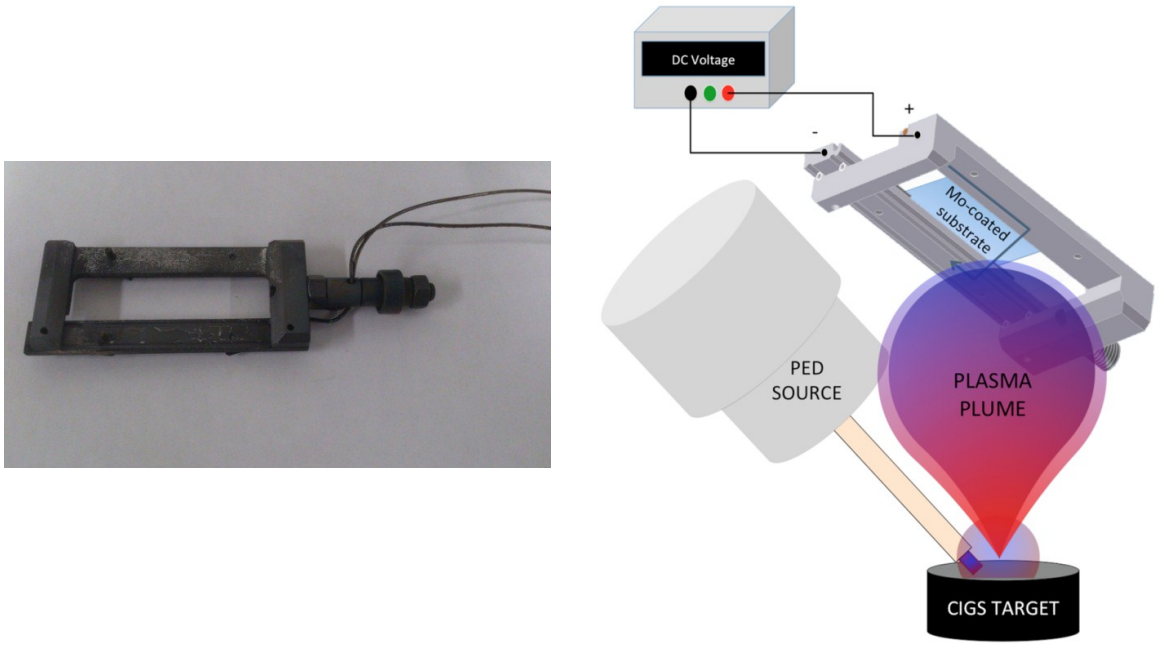

Figure 4.41: Picture of the Joule heating sample holder (left) and Representative scheme of the Joule heating experimental setup (right).

The surface temperatures of Mo and glass were monitored at the same time by a thermo-imaging camera (FLIR T420), setting the emissivity of Mo and soda-lime glass to 0.12 [62] and 0.95 [63], respectively.

The Mo-coated substrate was heated very slowly in order to prevent any stress on the glass by gradually increasing the applied voltage and waiting for the stabilization of the glass temperature, as represented in Figure 4.42.

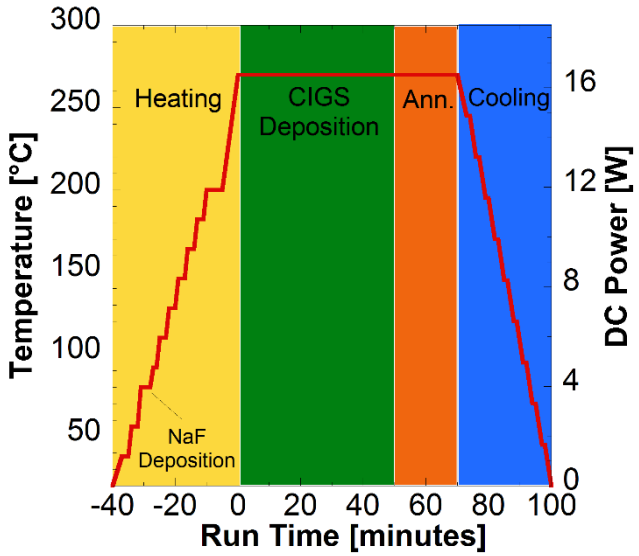

Figure 4.42: Substrate temperature (left) and applied DC power (right) of the Mo Joule heating method as a function of process time.

Once the temperature of 80 °C has been reached, the 30 nm-thick layer of NaF was grown before increasing the temperature to 270 °C for the CIGS deposition. After that, the DC power was kept constant for 20 minutes to promote the Na diffusion through the CIGS layer and finally the sample was slowly cooled down to room temperature.

Different types of substrates are tested with this heating method; the 2 main results for industrial perspectives are: i) possibility to use thermolabile substrates, due to a combination of low temperature PED deposition and localized Joule heating and ii) rapid heating/cooling times. In figure 4.43a e 4.43b a plot of rapid thermal heating and rapid thermal cooling process applied on a molybdenum film deposited on a polyimide substrate is shown.

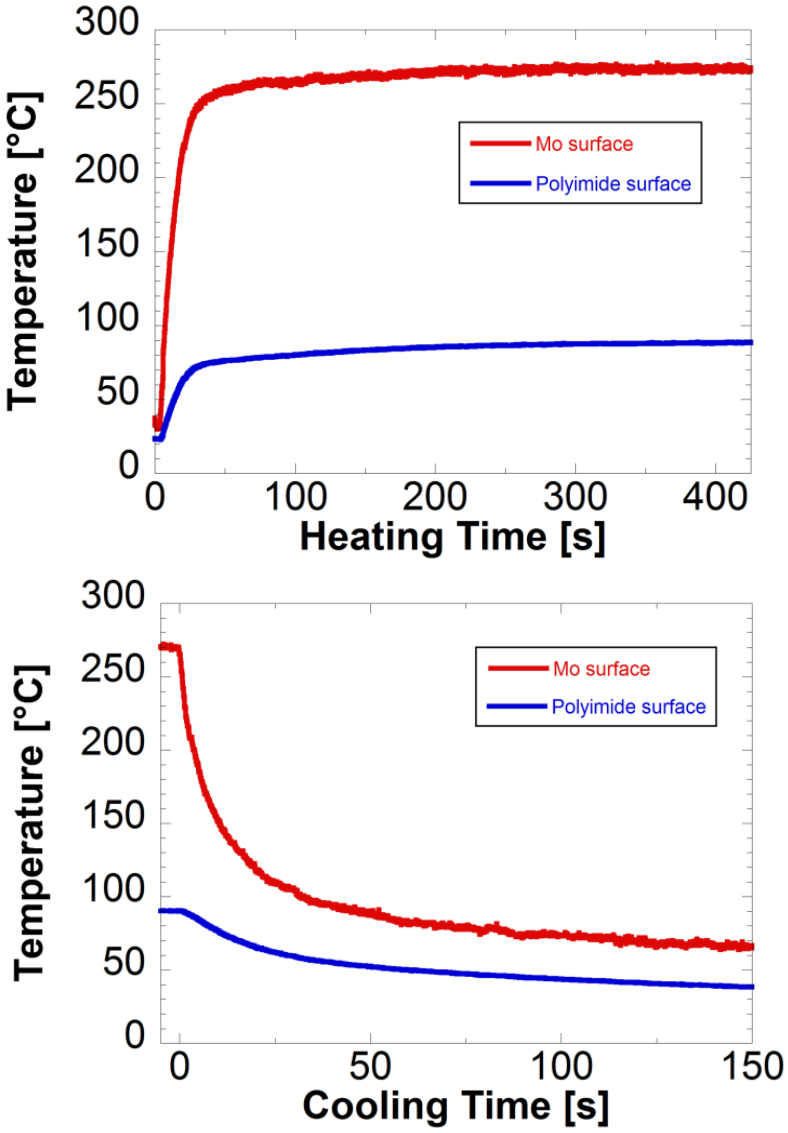

Figure 4.43: Fast joule effect heating process (a) and fast joule effect cooling process (b)

In Figure 4.44 two different thermal images at room temperature (top) and after a rapid thermal heating (down), demonstrate the excellent thermal uniformity.

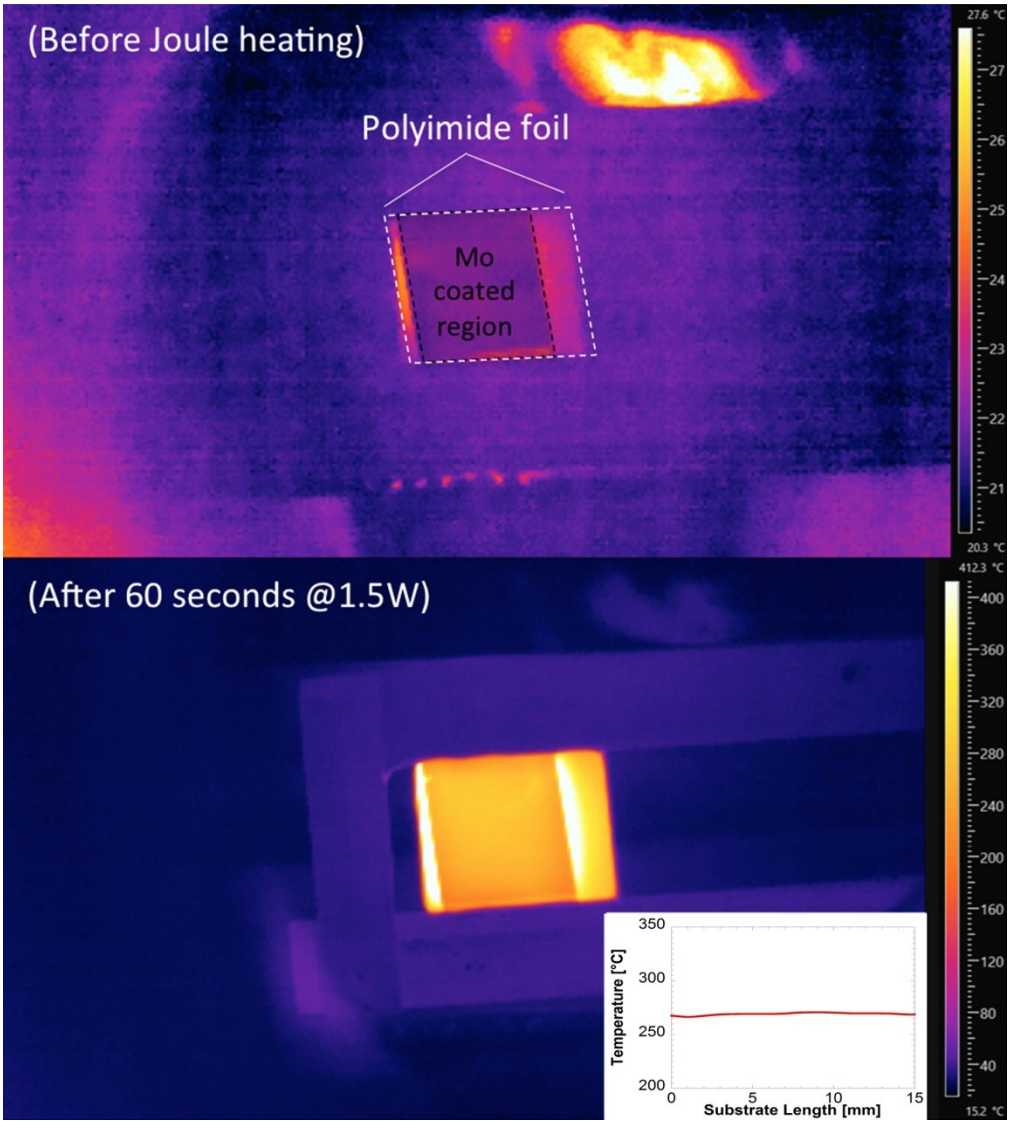

Figure 4.44: Sample thermal images before and after joule heating. The inset shows the temperature profile of the Mo surface.

The localized and low energy Joule methods is very efficient to limit the environmental heating, the wall chamber and the PED sources. Figure 4.45 shows the thermal map of the Mo/glass substrate before the CIGS growth. In the inset, the thermal profile along Mo surface is shown and it can be observed that, at 270 °C, the molybdenum temperature gradient is less than 10 °C and the glass temperature remains below 150 °C

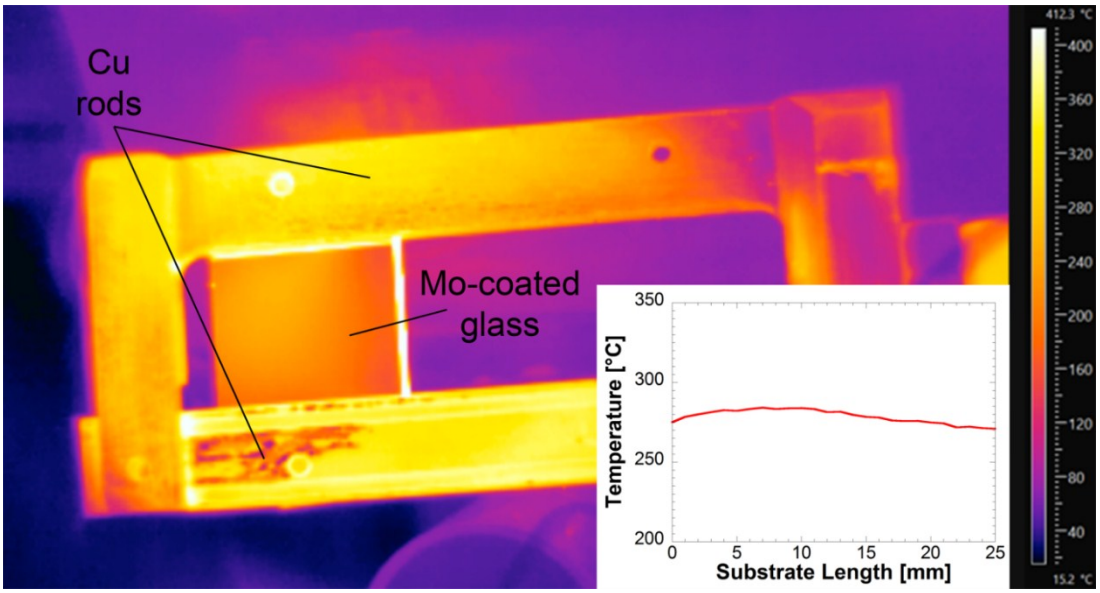

Figure 4.45: Infrared image of a Mo-coated glass substrate when a DC power of 16 W is applied between the two Cu rods. The inset shows the temperature profile of the Mo surface.

Once optimized the CIGS deposition, the complete solar cells were realized and compared. Figure 4.46 shows a comparative cross-sectional image of a CIGS thin film grown on a substrate heated by the Joule method (JH-CIGS) (Figure 4.46a) and a CIGS thin film grown with the conventional heating method (CH-CIGS) (Figure 4.46b).

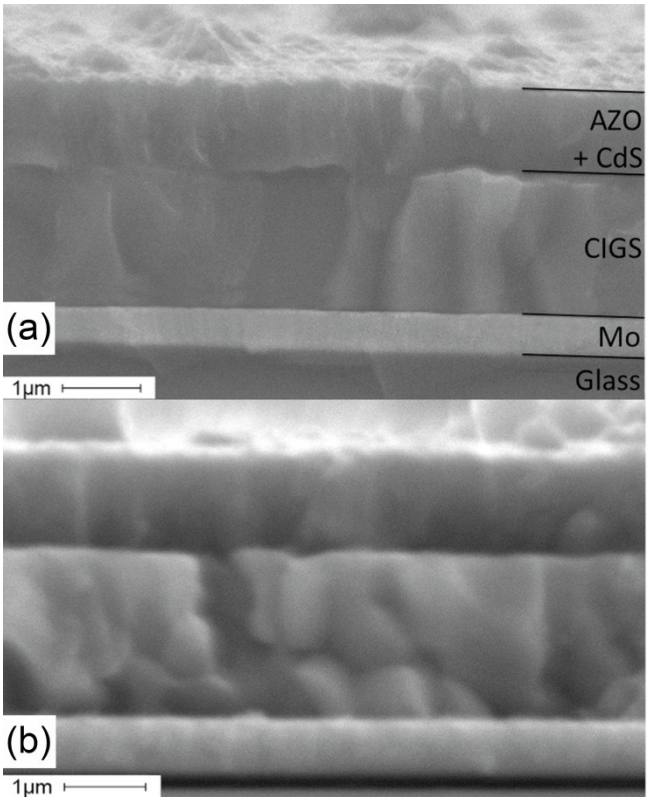

Figure 4.46 - Cross-sectional images of AZO/CdS/CIGS/Mo/Glass cells with a JH-CIGS (a) and with a CH-CIGS layer (b).

The former exhibits a very compact structure, characterized by the presence of larger grains with average dimension of about 2 μm. The growth mechanism leading to larger in JH-CIGS sample is currently under investigation, being only partially justified by the longer deposition time (50 minutes for depositing 2 μm-thick JH-CIGS and 15 minutes for a CH-CIGS layer with the same thickness).

Typical J-V characteristics of JH- and CH-CIGS (0.1 cm^2 wide) under standard illumination conditions (AM1.5G at 25°C) are shown in Figure 4.47. The corresponding cell parameters are reported in Table 4.16, from where it can be observed that the lower FF of the JH-CIGS cells is compensated by an increase in J_{SC} and V_{OC} values with respect to CH-CIGS-based devices, leading to similar efficiency values.

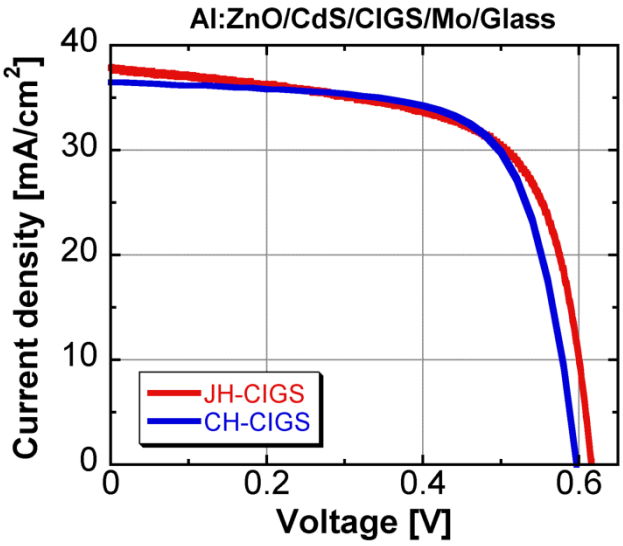

Figure 4.47 - Current-voltage characteristics of CIGS solar cells fabricated by Joule effect heating (red line) and by a conventional IR-lamp based heater (blue line), measured at 25 °C under AM1.5G (100 mW/cm^2) illumination.

Heating mode	V_{OC} (mV)	J_{SC} (mA/cm^2)	FF (%)	Efficiency (%)
JH-CIGS	616	37.97	65.2	15.25
CH-CIGS	597	36.50	69.0	15.03

Table 4.16: Photovoltaic parameters of solar cells presenting a CIGS layer fabricated at T ≈ 270°C by two different heating modes: by Joule heating (JH-CIGS) and by the external lamp heater (CH-CIGS). The top Al contacts are excluded from the estimation of the illuminated area.

As for the doping value, the net acceptor density, N_A, measured on a JH-CIGS solar cell, estimated at the minimum of the C-V profile [17], is about 6.9x10^{15} cm^{-3} (Figure 4.48), comparable to the value obtained on the traditionally heated CH-CIGS (6.2x10^{15} cm^{-3}).

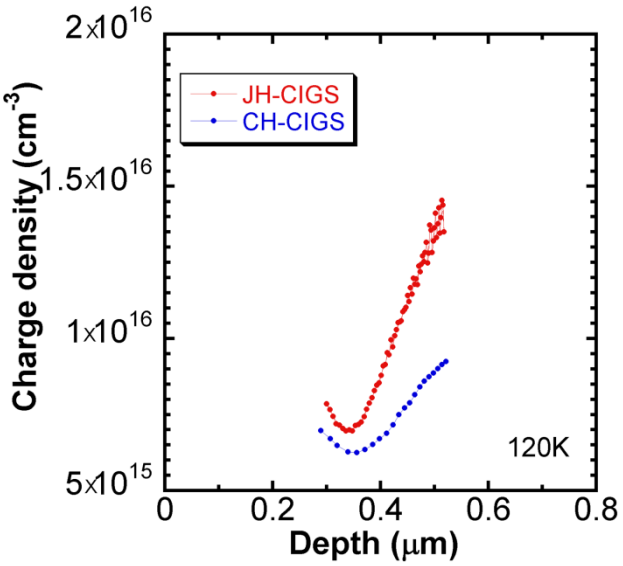

Figure 4.48: Comparison of CV profiles taken at 120K of conventionally heated (blue circles) and Joule-heated CIGS solar cells.

The results obtained by using the Joule heating, demonstrates that this method is particularly suitable for industrial applications, especially on non-conventional substrates such as polyimide and materials presenting a low melting point.

The Table 4.17 shows the power consumption of the two heating methods, JH and CH, as a function of the solar cell area.

Heating mode	6 cm^2 cell area	256 cm^2 cell area
Joule Heating-CIGS	15 W	630 W
Conventional heating-CIGS	1400 W	2200 W

Table 4.17: Power consumption comparison between Joule heating-CIGS and Conventional Heating-CIGS

The energy needed to heat the substrate is considerably reduced compared to a traditional heating making the Joule heating advantageous also from an economic point of view [57]. The power consumption necessary to heat through the Joule Heating a substrate of 256 cm^2 (16x16 cm^2) derives from a theoretical calculation because the prototype chamber shown in Figure 4.39, is not yet equipped with this type of heater.

The innovative idea, recently patented [57], of Joule Heating and the related technology is very interesting for the fabrication of CIGS, but can be employed to heat any material, being the only requirement the presence of a metal substrate where the current can flow.

References

[1] S. Rampino, F. Bissoli, E. Gilioli and F. Pattini, Prog. Photovolt: Res. Appl. 21 (2013) 588

[2]M. Bronzoni, M. Stefancich, S. Rampino, Thin Solid Films 520 (2012) 7054.

[3]S. Tricot, N. Semmar, L. Lebbah, C. Boulmer-Leborgne, J. Phys. D: Appl. Phys. 43 (2010) 65301.

[4] G. Hanna, J. Mattheis, V. Laptev, Y. Yamamoto, U. Rau, H.W. Schock, Thin Solid Films 31 (2003) 431–432.

[5] D.B. Chrisey, G.K. Hubler, Pulsed Laser Deposition of Thin Films, John Wiley & Sons, Inc., New York, 1994.

[6] H. Hahn, G. Frank, W. Klinger, A. Meyer, A.D. Stöiger, Z. Anorg. Allg. Chem. 271 (1953) 153.

[7]T. Negami, T. Satoh, Y. Hashimoto, S. Nishiwaki, S.-I. Shimakawa, S. Hayashi, Sol. Energy Mater. Sol. Cells 67 (2001) 1.

[8] Rudmann D. Effects of sodium on growth and properties of Cu(In,Ga)Se2 thin films and solar cells. s.l. : Dissertation for the degree of Doctor of Sciences, Swiss federal institute of technology - Zurich, 2004.

[9] J. H. Scofield, A. Duda, D. Albin, B. L. Ballard, and P. K. Predecki, Thin

Solid Films 26 (1995) 260.

[10] P. M. P. Salomè, A. Hultqvist, V. Fjallstrom, M. Edoff, B. Aitken, K. Vaidyanathan, K. Zhang, K. Fuller, and C. Kosik Williams, IEEE J. Photovolt. 3 (2013) 852-858

[11] E. Cadel, N. Barreau, J. Kessler, P. Pareige, Acta Materialia 58 (2010) 2634-2637

[12] S. Rampino, N. Armani, F .Bissoli, M. Bronzoni, D. Calestani, M. Calicchio, N. Delmonte, E. Gilioli, E. Gombia, R. Mosca, L. Nasi, F. Pattini, A. Zappettini, M. Mazzer, Appl.Phys.Lett. 101 (2012) 132107.

[13] M. Cwil, M. Igalson, P. Zabierowski, and S. Siebentritt, J. Appl. Phys. 103 (2008) 63701.

[14] T. Eisenbarth, T. Unold, R. Caballero, C. A. Kaufmann, and H. W. Schock, J. Appl. Phys. 107 (2010) 34509.

[15] M. Cwil, M. Igalson, P. Zabierowski, C. A. Kaufmann, and A. Neisser, Thin Solid Films 515 (2007) 6229.

[16] D. Drouin, A. R. Couture, D. Joly, X. Tastet, V. Aimez, and R. Gauvin, Scanning 29 (2007) 92.

[17] M. Lammer, U. Klemm, and M. Powalla, Thin Solid Films 387 (2001) 33.

[18] A. L. Fahrenbruch and R. H. Bube, Fundamentals of solar cells. New York: Academic Press,1983.

[19] Mette A, et al. Progress in Photovoltaics: Research and Applications. 15 (2007) 493-505.

[20] P. Jackson, D. Hariskos, R. Wuerz, O. Kiowski, A. Bauer, T. M. Friedlmeier and M. Powalla, Phys. Status Solidi RRL, 9 (2015) 28–31. doi: 10.1002/pssr.201409520

[21] W. Shockley, H.J. Queisser, J.Appl.Phys. 32 (1962) 510–519.

[22] S. Siebentritt, Sol.Energy Mater.Sol.Cells 95 (2011) 1471–1476.

[23] J.H. Werner, J. Mattheis, U. Rau, ThinSolidFilms 480–481 (2005) 399–409.

[24] C. Maragliano, L. Colace, M. Chiesa, S. Rampino, M. Stefancich, IEEEJ.Photovoltaics 3 (2013) 1106–1112.

[25] S. Rampino, M. Bronzoni, L. Colace, P. Frigeri, E. Gombia, C. Maragliano, F. Mezzadri, L. Nasi, L. Seravalli, F. Pattini, G. Trevisi, M. Motapothula, T. Venkatesan, E. Gilioli , SOL ENERG MAT SOL C, 133 (2015) 82-86

[26] D. Liao, A. Rockett, J.Appl. Phys. 91 (2002) 1978–1983.

[27] L. Roussak, G. Wagner, L. Makhova, I. Konovalov, Phys. Status Solidi C 6 (2009) 1287–1290.

[28] C.H. Lei, A. A. Rockett, I. M. Robertson, N. Papathanasiou, S.Siebentritt, J.Appl.Phys.100 (2006) 114915.

[29] B. Schumann, A. Tempel, G. Kühn, Sol.Cell 16 (1986) 43–63.

[30] B. J. Stanbery, S. Kincal, S. Kim, C. H. Chang, S. P. Ahrenkiel , G. Lippold, H. Neumann,T. J. Anderson, O. D. Crisalle, J.Appl.Phys.91 (2002) 3598–3604.

[31] L. C. Yang, J.Cryst. Growth 294 (2006) 202–208.

[32] J. Cieslak, T. Hahn, J. Kräußlich, H. Metzner, J. Eberhardt, W. Witthuhn, Phys.StatusSolidiC 6 (2009) 1023–1026.

[33] R. Chakrabarti, B. Maiti, S. Chaudhuri, A. K. Pal, Sol.EnergyMater.Sol.Cells 43 (1996) 237–247.

[34] S. Zott, K.Leo, M.Ruck, H.W.Schock, J.Appl.Phys. 82 (1997) 356–367.

[35] D. N. Hebert, J. A. N .T. Soares, A. A. Rockett, Mater.Res.Soc. Symp. Proc1165 (2010) 93–100.

[36] A. Rockett, Thin Solid Films 480–481 (2005)

[37] G. Monaco, M. Gastaldi, P. Nicolosi, M.G. Pelizzo, E. Gilioli, S. Rampino, F. Bissoli, F.Pattini, S. Agnoli, G. Granozzi, N. Manuzzato, Eur. Phys. J. Spec. Top. 169 (2009) 159.

[38] R. Henda, G. Wilson, J. Gray-Munro, O. Alshekhli, A.M. McDonald, Thin Solid Films 520 (2012) 1885.

[39] L. Zhang, Q. He, W .L. Jiang, F. F. Liu, C. J. Li, Y. Sun, Sol. Energy Mater. Sol. Cells 93 (2009) 114.

[40] T. Yoshitake, G. Shiraishi, K. Nagayama, Appl. Surf. Sci. 197–198 (2002) 379.

[41] K.L. Chen, J.H. Chen, H.C. Yang, H.E. Horng, Physica C 372–376 (2002) 1078.

[42] G. Koren, R.J. Baseman, A. Gupta, M.I. Lutwyche, R.B. Laibowitz, Appl. Phys. Lett. 56, 2144 (1990)

[43] D. Lubben, S. A. Barnett, K. Suzuki, S. Gorbatkin, J.E. Greene, J. Vac. Sci. Technol. B 3 (1985) 968.

[44] S. Rampino, F. Pattini, C. Malagù, L. Pozzetti, M. Stefancich, M. Bronzoni, Thin Solid Films 562 (2014) 307-313

[45] F. Fabbri, G. Padeletti, T. Petrisor, G. Celentano, V. Boffa, Supercond. Sci. Technol. 13 (2000) 1492.

[46] Y. Li, K. Tanabe, IEEE Trans.Appl. Supercond. 9 (1999) 1586.

[47] G. Muller, M. Konijnenberg and G. Rafft, Deposition by means of pulsed electron beam ablation. in F.C. Matacotta and G. Ottaviani. Science and Technology of Thin Films. s.l. : World Scientific, 1995, pp. 89-119.

[48] B. Schumann, A.Tempel, G.Kühn, Sol.Cell16 (1986) 43–63.

[49] F. Pattini, M. Bronzoni, F. Mezzadri, F. Bissoli, E. Gilioli and S Rampino, Journal of Physics D: Applied Physics, 46 (2013) 24

[50] S. B. Zhang, S-H Wei, A. Zunger and H. Katayama-Yoshida, Phys. Rev. B 57 (1998) 9642

[51] C. Rincon and F. J. Ramirez J. Appl. Phys. 72 (1992) 4321

[52] F. J. Haug, M. Krejci, H. Zogg, A. N. Tiwari, M. Kirsch and S. Siebentritt, Thin Solid Films 239 (2000) 361–362

[53] G. Comsa and R. David, Chem. Phys. Lett. 49 (1977) 512

[54] T. Venkatesan, X. D. Wu, A. Inam and J. B. Wachtman Appl. Phys. Lett. 52 (1988) 1193

[55] J. Segner, C. T. Campbell, G. Doyen and G. Ertl Surf. Sci. 138 (1984) 505

[56] H. Dang and Q. Qin, Phys. Rev. B 60 (1999) 11187

[57] M. Bronzoni, D. Delmonte, E. Gilioli, M. Mazzer, F. Pattini, S. Rampino. (2014). Italian Patent No. MI2014A000960, “Metodo di fabbricazione di celle solari a film sottile”. Milano: Ufficio italiano Brevetti e Marchi.

[58] S. R. Kodigala, CIGS BASED THIN FILM SOLAR CELLS. s.l. : Elsevier, 2010. pp. 28-35

[59] N. A. Allsop, A. Schonmann, H. J. Muffler, M. Bar, M. C. Lux-Steiner, C. H. Fischer, Progress on Photovoltaics: Research and Applications; 13 (2005) 607–616.

[60] G. Muller, M. Konijnenberg and G. Rafft, Deposition by means of pulsed electron beam ablation. in F.C. Matacotta and G. Ottaviani. Science and Technology of Thin Films. s.l. : World Scientific, 1995, pp. 89-119.

[61] S. Rampino, F. Annoni, M. Bronzoni, M. Calicchio, E. Gombia, M. Mazzer, F. Pattini, E. Gilioli, Renew. Sust. Energ. 7 (2015) doi: 10.1063/1.4906979

[62] D. Xinkang, W. Cong, W. Tianmin, Z. Long, C. Buliang, and R. Ning, Thin Solid Films 516 (2008) 3971-3977.

[63] M. Rubin, Sol. Energ. Mater. 12(4) (1985) 275-288.

Conclusions and Outlook

This Thesis concerns the study and development of a new method to grow thin film solar cells based on CIGS, by using the Pulsed Electron Deposition (PED) technique. The activity, carried on at IMEM-CNR in Parma, deals with both fundamental and applied research to address the following issues:

1. To optimize a novel low temperature and single stage fabrication process for CIGS solar cells with efficiency >15%, by exploiting the peculiar features of PED technique (stoichiometric transfer and high kinetic energy of the adatoms).
2. To scale up the CIGS deposition process from the laboratory scale to the pre-industrial fabrication of solar mini-modules, limiting some drawbacks typical of the PED technique (i.e. narrow-peaked distribution of adatoms, generation of particulates, long-term stability of the e-beam source).

1. CIGS is a complex material. In order to guarantee a good stoichiometric transfer from the target in a single stage, the pulsed e-beam acceleration voltage has been set to16 kV; it's a remarkable result, allowing to avoid further steps for compositional adjustments (post-growth thermal annealing or selenization treatment). The growth of CIGS films was performed by varying the temperature of the glass substrate from RT to 500°C. The CIGS films deposited at very low temperature exhibited poor crystal quality and great stoichiometric preservation, while when the temperature exceeds 300°C, Se re-evaporation started to occur from the film surface, losing the required stoichiometry. A Se depleted film shown a high degree of electrical compensation, which lowers the free acceptors concentration in CIGS layer. A

compromise temperature of 270°C was found to maximize both crystallization and p-type doping in CIGS films. This surprisingly low temperature for growing high-crystal quality films can be possible by exploiting the energetic distribution of PED adatoms, arriving at the substrate with kinetic energies >>1eV, providing high diffusion mobility on the film surface. This temperature is at least 150°C lower with respect to that used in the state-of-the-art CIGS deposition process as thermal co-evaporation and RF-sputtering, enabling the CIGS deposition on thermolabile and flexible substrates, suggesting interesting development in the emerging field of the "BIPV" (Building Integrated PhotoVoltaic).

On the other side, the Na diffusion from the glass substrate to the CIGS is hindered at such a low temperature, limiting the p-type doping concentration in the absorber layer (< $5x10^{14}$ cm^{-3}) and hence the cell efficiency (up to 7.5%). This challenge was solved by growing a precursor layer (NaF) before the CIGS. The p-type doping of CIGS was found to monotonically increase (from $1x10^{14}$ to $1x10^{17}$ cm^{-3}) with the NaF increasing thickness layer from 0 to 40 nm. 30 nm NaF thickness was used to prevent the drop in the CIGS mechanical adhesion with the substrate occurring for thicker NaF layers and to finally get a free acceptor concentration value of $6x10^{15}$ cm^{-3} in the CIGS, as measured by Capacitance-Voltage measurements, ending to photovoltaic efficiencies > 15% on a 0.15 cm^2-wide solar cells with the following architecture: Al:ZnO/CdS/CIGS/Mo/Glass. A further study on the post-growth CIGS annealing process allowed to improve both efficiency and uniformity on a wider cell area. A thermal annealing treatment of 80 minutes was found to enhance the Na diffusion from the NaF layer and thus the free acceptor density (up to $1x10^{16}$ cm^{-3}) without affecting the film mechanical stability. Conversion efficiency values > 17% over 0.1 cm^2 area and > 16% over a 6 cm^2-wide cell were measured on annealed samples. Finally, by inserting an undoped ZnO layer between CdS and Al:ZnO, the resistive effects in the cells were reduced, thus achieving a remarkable efficiency of 18.75% on 0.15 cm^2 –wide active area.

Since a significant efficiency improvement (up to 28%) has been suggested by theoretical calculations if the grain size of the absorber layer is enhanced, the low-temperature CIGS growth process was tested using crystalline substrates (GaAs

and Ge). Single-crystal CIGS layers with thickness > 1.5 μm have been epitaxially grown at 300°C; only twin boundaries along the (112) directions were detected as extended crystal defects, with no threading dislocations. These epitaxial films exhibit a reduced electrical compensation with respect to polycrystalline CIGS, and current-voltage and capacitance-voltage measurements confirm an intrinsic p-type conductivity, with a free carrier concentration of $3.5x10^{16}$ cm^{-3}.

The realization of epitaxial CIGS grown on Ge as absorber layer in a solar cell completed with the standard multi-layer architecture (Al:ZnO/ZnO/CdS) and the comparison with a standard poly-crystalline CIGS layer is in progress, to be used both in single-junction and in tandem solar cells.

2. To scale up the CIGS deposition route for fabricating solar mini-modules, three main challenges, intrinsically present in PED technique, have been faced in the second part of the Thesis

a. The generation of micrometer particulate produced during the ablation process, responsible to reduce the cell efficiency and the performance uniformity on large area. To control both particulate density and dimensions, a negative electric fields has been applied between substrate and target to repulse particles away from the growing film surface. A negative DC bias > -200 V is effective to reduce the droplet density on the film surface by one order of magnitude, halving their average size.
b. A narrow-peaked angular distribution of the adatoms generated by PED as compared to thermal evaporation techniques, which limits a coating uniformity > 90% over a maximum area of only 10 cm^2. A mathematical simulation model, based on the superimposition of the plumes generated by an array of PED sources was compiled in order to optimize the deposition uniformity over larger substrates (16x16 cm^2, the typical size of a conventional silicon-based solar cell). The model allowed to change three parameters: i) the number of required guns, ii) their relative position in the vacuum chamber and iii) the most substrate motion type. A CIGS deposition uniformity of 98% can be achieved using a vacuum chamber composed of an array of 4 PED sources arranged in a squared geometry, and equipped

with a back-and-forth linear substrate translation system. Such a configuration allows a considerable reduction of deposition time (-50%),material (-50%) and costs in comparison to thermal co-evaporation technique.

c. The long-term instability of the PED e-beam due to the overheating effects of both the cathode and the dielectric tube is a relevant drawback for prolonged deposition processes. With the aim of limiting the heat transferred to the PED source from the conventional graphite heater, a novel type of non-radiative heater was designed and tested. By flowing a DC electrical current across the Mo layer (the back contact on the glass), a local and selective heating of the substrate by Joule effect is achieved. Solar cells based on CIGS heated by Joule effect exhibit efficiencies >15%, equivalent to those fabricated by the standard radiative route, using a much lower power (only 1/100 on 6 cm^2 area). Moreover, the rapid heat transfer led by Joule effect leads to faster heating and cooling stages (few tenths of seconds instead of some minutes), thus strongly reducing the total cell fabrication time.

All the fundamental achievements, as well as the instrumental and technological improvements developed in this Thesis, have been utilized to design and build a pre-industrial multi-PED prototype system. It has been recently installed at IMEM-CNR: the first CIGS deposition tests conducted at room temperature on 16x16cm^2-wide glass (Figure 1) confirm a satisfactory agreement between the theoretical distribution of CIGS thickness over the substrate and the measured profiles; the installation of the substrate heater in the chamber has been completed, and the system is now ready to fabricate the first CIGS mini-modules.

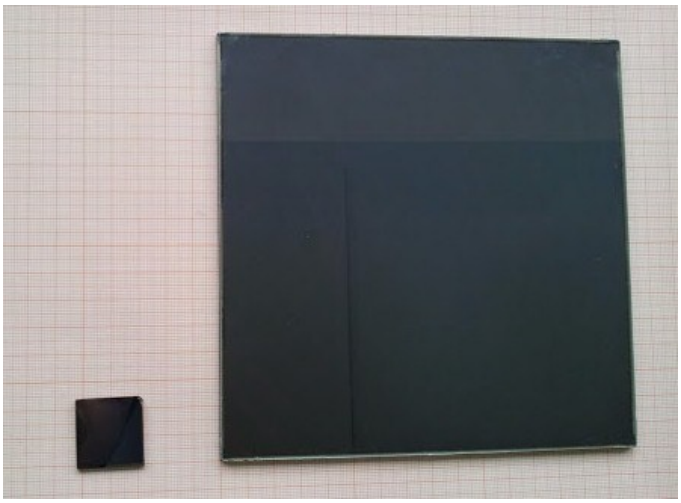

Figure 1 - Comparison between a CIGS film deposited in the lab-scale PED system on a 2.5x2.5cm^2-wide glass (left), and a sample grown on a substrate area of 16x16cm^2 using the pre-industrial multi-PED system (right).

This Thesis work clearly confirms that by optimizing some technological issues, the PED technique can be a suitable and robust technique for industrial applications. Besides the thin film solar cells (in only very few years we can compete with the best laboratory in the word working on CIGS), the results achieved in this Thesis could open new possibilities of research in various fields of thin film technology, in particular when complex materials have to be deposited in a simple process (stoichiometric transfer from the target to the growing film and low temperature deposition), with good surface morphology (substrate bias to limit the particulates), with an efficient, rapid and uniform heating (by Joule effect).

Acknowledgments

At the end of these three years of work I would thank all the people who, for various reasons, have been with me on this journey, without their help this thesis would have never been accomplished.

First, I would like to thank my supervisor, Dr. Stefano Rampino, which allowed me to perform Ph. D. at the IMEM-CNR, guided and supported me during the last three years and whose theoretical and methodological contributions are at the base of my training and activity. Many thanks to Dr. Edmondo Gilioli his enthusiasm and passion for research has been inspiring for me.

I thank all members of the TEAM PED for the advices received and the fruitful discussions: Dr. Francesco Pattini (especially for his knowledge and experiences), Dr. Francesco Bissoli, Dr. Massimo Mazzer and Nicoletta Marigo. Special thanks to Filippo Annoni, it has been a pleasure to work and share this experience with you.

I also thank all the people at IMEM-CNR involved in this thesis project. Thanks to Dr. Davide Calestani and Dr. Andrea Zappettini for the development and realization of the targets used during this work. Thanks to Francesco Mezzadri, Tullo Besagni e Patrizia Ferro for X-ray diffraction measurements and Lucia Nasi for TEM measurements. Thanks also to Marco Calicchio, Enos Gombia and Aldo Kingma for the characterizations of the devices.

I would also like to thank my foreign colleagues who worked on the project during the time they spent at IMEM-CNR. Vimalkumar Thottapurath Vijayan for

developments on the buffer layer, J.P. Garcia for those on the TCO. I also thank Valerio Tega and Prof. Lorenzo Colace (University of Roma 3) for the study and implementation of Ge substrates, Marco Stefancich and Carlo Maragliano (Masdar Institute – Abu Dhabi) for the measures carried out and the stimulating discussions.

This work has been partially supported by the Italian Ministry of University and Research (FIRB-2008 Project, “Nanostructured and Thin-Films Photovoltaic Devices for spectral splitting concentration systems“) and by CNR (Programme “Progetto Bandiera – La Fabbrica del Futuro”, project “MaCISte, “Mature CIS-based solar cells technology”) and (programme "Industria 2015 - PED4PV” of the Italian Ministry of Economic Development).

Thanks to friends David Delmonte and Giulia Spaggiari with which I happily shared the office in recent years. Beside them, a big thank to all my colleagues and friends with whom I shared lessons, commitments, worries and frustrations, as well as ideas and satisfactions.

Finally, a special thanks to my family that has always been supportive and helped me in all this time.

Abbreviations and symbols

AFM	Atomic Force Microscopy
AM1.5	Air mass 1.5
AZO	Aluminum doped Zinc Oxide
BIPV	Building Integrated Photovoltaic
CBD	Chemical Bath Deposition
CGS	Compound formed from Cu, Ga, Se; usually CuGaSe2
CH	Conventional Heating
CIGS	Compound formed from Cu, In, Ga, Se; Cu(In,Ga)Se2
CIS	Compound formed from Cu, In, Se; CuInSe2
CGI	Cu/(In+Ga) ratio
CS	Channel-Spark
C–V	Capacitance – Voltage
EDX	Energy-Dispersive X-ray analysis
EBIC	Electron Beam Induced Current
E_g	Energy Gap
FF	Fill Factor
FFT	Fast Fourier Transform
GGI	Ga/(In+Ga) ratio
I–V	Current – Voltage
HAADF	The High-Angle Annular Dark-Field
HIP	Hot Isostatic Press
HRTEM	High Resolution Transmission Electron Microscopy

ILGAR	Ion Layer Gas Reaction
JH	Joule Heating
J_{sc}	Short-circuit current
J–V	Current density – voltage
MBE	Molecular Beam Epitaxy
ODC	Ordered defect compound
OVC	Ordered vacancy compound
PDT	Post-deposition treatment
PED	Pulsed Electron Deposition
PLD	Pulsed Laser Deposition
PV	Photovoltaic
PVD	Physical Vapour Deposition
SEM	Scanning Electron Microscopy
SLG	Soda-Lime Glass
TCAD	Technology Computer-Aided Design
TCO	Transparent Conductive Oxide
THC	Transient Hollow Cathode
V_{oc}	Open Circuit Voltage
XRD	X-ray diffraction
YBCO	Yttrium Barium Copper Oxide